UNIVERSITY OF SOUTHAMPTON

Integrated Optical Fluorescence Multi-Sensor System

by

Ping Hua

A thesis submitted for the
degree of Doctor of Philosophy

in the
Faculty of Engineering, Science and Mathematics
Optoelectronics Research Centre

July 2009

UNIVERSITY OF SOUTHAMPTON

ABSTRACT

FACULTY OF ENGINEERING, SCIENCE AND MATHEMATICS
OPTOELECTRONICS RESEARCH CENTRE

Doctor of Philosophy

Integrated Optical Fluorescence Multi-Sensor System

by Ping Hua

Research on fluorescence-based integrated optical immunoassay multisensing systems has gained growing interest in the last ten years. This is because the systems have the potential to simultaneously detect multiple analytes in a single measurement, and the techniques involved are fast, robust and cost-effective. Therefore they have the potential to replace conventional chromatographic techniques, as the monitoring systems for the rapid assessment of water or food samples. Other areas, such as clinical diagnostics or forensic science also have a demand for highly multiplexed analytical systems.

This thesis presents a novel 32-analyte integrated optical fluorescence-based multisensor, and its integration to an automated multi-bio-sensing system. This system is primarily used for detecting organic pollutants in river water.

A fibre-pigtailed sensor chip consists of a channel waveguide circuit which distributes evanescent excitation light to 32 separate sensing patches on the chip surface is realised. Bio/immunochemistry may be used to sensitise each of the 32 patches to a specific analyte and a microfluidic system is used to automatically handle the sample injection over the sensor surface, enabling rapid, simultaneous and high-sensitivity fluorescence detection of up to 32 pollutants. A fibre coupled photodiode detection array monitors the 32 separate fluorescence signals, and software controls the laser, fluidics, data acquisition and processing of the fluorescence signals and records the laser power and ambient and chip temperature.

Extensive study was undertaken theoretically and experimentally in order to optimise the sensor chip design, fabrication and sensing system. The surface intensity of the sensor region was also studied in depth, based upon beam propagation method simulation of waveguides which gave the optimum fibre to waveguide coupling efficiency. Low loss, high signal strength and robust optical transducers were realised.

The surface immunochemistry used in this research was based on binding inhibition tests that require antibodies directed against specific analytes and analyte derivatives that can be covalently bound to a transducer surface. The sensing system was characterised for a single analyte, estrone, and a limit of detection (LOD) below 1 ng.L^{-1} was achieved. The sensing system was then applied against up to six organic pollutants and the LODs below 20 ng.L^{-1} were achieved for all six analytes.

A detailed study was also carried out with a CCD detector system, used to replace the fibre collection and photodiode array system and allow straight forward extension to more than 32 analytes. A direct comparison between these two systems is also presented.

Declaration of Authorship

I, Ping Hua, declare that this thesis entitled "Integrated optical fluorescence multi-sensor system" and the work presented in it are my own. I confirm that:

- This work was done wholly or mainly while in candidature for a research degree at the University of Southampton;
- Where any part of this thesis has previously been submitted for a degree or any other qualification at this University or any other institution, this has been clearly stated;
- Where I have consulted the published work of others, this is always clearly attributed;
- Where I have quoted from the work of others, the source is always given. With the exception of such quotations, this thesis is entirely my own work;
- I have acknowledged all main sources of help;
- Where the thesis is based on work done by myself jointly with others, I have made clear exactly what was done by others and what I have contributed myself;
- Parts of this work have been published as shown in the list of publications.

Signed: _____

Date: _____

Acknowledgements

The author is most grateful to her supervisor Professor James Wilkinson for his guidance, encouragement and support throughout this work.

The author wishes to extend her special thanks to Patrick Hole for his assistance in testing optical components for the AWACSS project, to Peter Horak, Paul Hoy and Daniel Friedrich for their constructive discussions, to Eleanor Tarbox for her proofreading of this thesis, and to Dave Sager and Neil Sessions for their help in the cleanroom, as well as to all members in the group for their support and encouragement.

The author also wishes to acknowledge all partners of AWACSS project, particularly the group in Tübingen University for their contribution to the sensor surface chemistry, to King's College, University of London for providing analytes and antibodies, and to the former Central Research Laboratory in London for constructing the detection system.

Finally, the author would like to thank her family for their patience, understanding, encouragement and support.

Contents

List of Figures

List of Tables

List of Symbols and Abbreviations

μ	permeability
μ_0	freespace permeability
c	speed of light
C_{ab}	antibody concentration
D	molecule surface density
D_{ab}	antibody diffusion coefficient
D_e	diffusion coefficient
D_{eff}	effective aperture of lens
D_k	distance away from the emitting surface
d_p	penetration depth of evanescent field
E_f	electric field in fibre
E_g	electric field in waveguide
f	focal length
F	Fourier transform
F^{-1}	inverse Fourier transform
H	magnetic field strength
h	Planck's constant
$\mathrm{H}(\omega)$	transfer function
I(t)	electric current
I_s	surface intensity
k_b	f-number
n_d	dark noise or dark current
n_{eff}	effective refractive index of a waveguide mode

n_m	Mode index
n_{photon}	photon noise or shot noise
n_r	readout noise
n_s	substrate index
Γ_{max}	maximum binding rate
η, η_{qe}	quantum efficiency
η_c	coupling efficiency
η_{ccd}	CCD system collection efficiency
λ_e	emission wavelength
λ_p	pump wavelength
ρ	surface density
σ_a	absorption cross-section
$\sigma_{background}$	standard deviation of background signal
σ_{signal}	standard deviation of signal
Φ	incident photon flux
ω	angular frequency
Ω	solid conical angle
ω_c	cut-off frequency for a filter
Ω_k	solid angle of emitted light
ϵ_0	freespace permittivity
AWACSS	automated water analyser computer supported system
BSA	bovine serum albumin
BPM	beam propagation method
CCD	charge-coupled device
CMOS	complementary metal oxide semiconductor
CRL	Central Research Laboratory
DC	direct current
DCC	dicyclohexylcarbodiimide
DMF	dimethylformamide
ELISA	enzyme-linked immunosorbent assay
EU	European Union
FD	finite difference
FFTCCD	full frame transfer charge-coupled device

FIA	flow injection analyser
FT	Fourier transform
FTCCD	frame transfer charge-coupled device
HCCD	horizontal serial register charge-coupled device
HPLC	high pressure liquid chromatography
IE	ion exchange
ILCCD	interline transfer charge-coupled device
LOD	limit of detection
MZI	Mach-Zehnder interferometer
NA	numerical aperture
ND	neutral density
NEP	noise equivalent power
ORC	Optoelectronics Research Centre
PBS	phosphate buffered saline
PD	photodiode
PECVD	plasma enhanced chemical vapour deposition
PIN	positive-intrinsic-negative
PM	polarisation maintaining
QE	quantum efficiency
RF	radio frequency
RIANA	RIver ANAlyser
RIfS	reflectometric interference spectroscopy
RIU	refractive index unit
ROI	region of interest
RT	room temperature
SNR	signal to noise ratio
SPR	Surface Plasmon Resonance
TE	transverse electric
TM	transverse magnetic
UV	ultra-violet
VCCD	vertical serial register charge-coupled device
VCSEL	vertical cavity surface emitting laser
WG	waveguide

Chapter 1

Introduction

1.1 The objectives of the work

Monitoring water quality and identifying pollution sources are important tasks in the management of rivers, which are major sources of water for human consumption. The main objectives of the overall research project are to construct and demonstrate a cost-effective, on-line, water-monitoring biosensor to rapidly and simultaneously measure a plurality of low molecular weight organic pollutants; for example, pesticides, antibiotics and endocrine distruptors, with the potential for remote control and surveillance. This work was undertaken in the framework of the Automated Water Analyser Computer Supported System, funded by the European Commission, under the Fifth Framework Programme and contributing to the implementation of the Key Action "Sustainable Management and Quality of Water" within the Energy, Environment and Sustainable Development.

An initial market survey, covering twelve European countries and the USA, was undertaken by Siemens, one of the project partners. The outcome of this survey represents the present situation in analytical practice in the different countries based on the present EU legislative needs (2; 3) and available laboratory equipment and assays. The collected data covered lists of substances, data on the number of sampling sites, sampling frequencies, number of samples, detection limits and methods applied, numbers of positive findings, detection limit below 0.1 μg.L^{-1} as well as analytical costs. The research finding shows that the annual European expenditure for analysis of organic compounds

in water-monitoring is excess of 29 million Euro (4). The top 32 compounds account for more than 48% of the total expenditure. The total number of analyses performed to detect all compounds in one year is 2.9 million. The top 32 compounds account for more than 26% of the total measurements conducted. Trace chemical analysis using state-of-the-art analytical instrumentation presently carries a high cost per measurement, so that a low-cost instrument capable of simultaneously measuring many of these priority pollutants is expected to meet an important market need and gain widespread acceptance, particularly if it is readily adaptable to new compounds as the need arises and if it can operate unattended with centrally controlled monitoring and surveillance of water systems (4).

The integrated optical fluorescence multi-sensor instrument described in this thesis is based on evanescent field technology. Laser light is coupled into an optical transducer and guided down to the multi-sensing area, which contains 32 patches in this case. The transducer surface is chemically modified in spatially distinct loci with analyte derivatives. Analyte-specific antibodies are labelled with a fluorescent marker which, upon binding to the transducer surface, are excited in the evanescent field. The emitted light is then collected for detection with 32 polymer fibres. The design allows for the simultaneous measurement of multi-analyte spots.

The immunochemistry utilised in the project takes advantage of a binding inhibition test that requires antibodies directed against specific analytes and analyte derivatives that can be covalently bound to a transducer surface. A huge number of polyclonal antibodies and their corresponding analyte derivatives have been produced for a variety of organic micro-pollutants. After being purified and labelled with a fluorescent marker, they were developed into immunoassays and used in this research project.

As part of the overall research project, the work described in this thesis and conducted by the author has focused on the following main tasks:

- Design and fabrication of IO sensor arrays. Selection of waveguide materials technology and optimisation of fibre coupling, surface irradiance, packing density, optical isolation and chemical compatibility; design of sensor array geometry for small total sample volume, low crosstalk and high signal strength; waveguide circuit layout and mask fabrication, with incorporation of tapered waveguides for reduced

photobleaching and high-index over-layers for improved pump efficiency. IO sensor arrays with a deposited isolation layer and with the fibre coupling loss and surface irradiance experimentally traded-off.

- Optimisation of the fabrication parameters and realization of the final IO sensor array chips.

- Packaging. Optimisation of inputs to sensor arrays for optical coupling, establishing the apparatus for improving optical alignment, adopting of final chip fabrication and interconnection procedures.

- Signal collection from arrays. The establishment of laboratory-based signal collection from photodiode arrays via hardware tests for PD array readout, AD conversion and hardware control. The determination of collection efficiency and signal noise performance.

- Detection and signal/noise optimisation. The development of strategies for background fluorescence subtraction, ambient light suppression and noise reduction depending upon the test protocols, raw S/N ratio, extent of photobleaching, and the implementation of the photodetection system.

- Production of optimised sensor array chips assemblies with robust and stable optical coupling for field tests.

- Determination of ultimate system detection limits, in collaboration with staff at King's College, University of London and the University of Tübingen, Germany.

1.2 State of the art of optical biosensors

Research activities on chemical and biochemical sensors have progressed dramatically over the past three decades. At present, much research work is focused on the development of systems capable of multi-analyte detection in a single sample, for environmental, clinical or security applications. Optical sensors have great potential in this field because of their ability to probe surfaces and films, using a range of optical phenomena while achieving low noise and high sensitivity. In addition, they have advantages in speed and immunity from electromagnetic interference, and permit in-situ sensing and real-time

measurements. Optical sensors are also suitable for miniaturization and for remote and multi-analyte sensing.

In general, the operation of an immunoassay biosensor can be divided into two components. The first is the immunoassay process, which is based on antigen (analyte of interest) and antibody binding reactions providing a concentration-dependent response to the analyte, and the second part is the physical transduction process, which is based on converting the biological binding process into a measurable signal. The techniques explored for the physical transduction process vary from electrochemical, mass, thermal to optical systems.

Optical biosensors offer more advantages over laboratory based systems compared to other sensing systems. In addition to the advantages of optical sensors mentioned above, another important feature of an optical sensor system is that it is substantially free from electromagnetic interference and has a reduced possibility of causing an explosion in a dangerous environment, compared to electrical transduction systems.

There have been many applications in both the sensing industry and in research where optical phenomena are utilised. The surface plasmon resonance (SPR) biosensor is one example, it is one of the most sensitive devices currently on the market and is also the most popular tool for characterizing and quantifying biomolecular interactions and for environmental monitoring. The SPR affinity sensor detects chemical or biological substances by measuring their binding to the sensor surface. This binding is measured by monitoring changes in the refractive index close to the sensor surface. Any binding or adsorption process which results in a change in surface refractive index will be measured (5). A rigorous model, based on this principle, was established for environmental monitoring (6). This model detects the change in transmitted power when a thin layer is adsorbed to the metal-clad region of the sensor, as a function of the waveguide and metal film parameters. The excitation and propagation of modes in the metal-clad region were analysed and, based on this, the device transmission was determined in the presence of sensing films (6). Based on the same principle, a SPR sensor probe with an integrated reference surface was investigated (7). In order to fabricate the integrated reference surface, two dielectric layers with different thicknesses were deposited on the single gold SPR sensor surface. The working sensor surface was a dielectric layer with immobilized bovine serum albumin (BSA) antigen and an adjacent thin dielectric layer, without BSA,

that provided the reference surface. A specific immunoreaction of anti-BSA antibody was detected after immersion of the SPR probe into a sample solution. Simultaneous observation of reference and working surface response enabled the determination of the immunoreaction, without the need for the baseline measurements (7). The integrated SPR sensor device, Spreeta 2000, was reported (8) to have a size of a thumbnail and it incorporates all of the optical and optoelectronic components necessary for implementing SPR biosensing into an inexpensive and moulded plastic package. It is claimed that the performance of Spreeta 2000 is sufficient for virtually any SPR biosensing applications (8). The low noise of about $1.8\text{x}10^{-7}$ RIU in 0.8s and the response of 0.2% over $\Delta n = 0.04$ of the sensor were achieved. This also gives an example of shifting the SPR applications from high-cost systems designed for laboratories to low-cost, disposable, portable electronic systems designed for the field.

The integrated optical Mach-Zehnder interferometer (MZI), as another example, is an evanescent refractometer whose surface may be chemically modified to render it sensitive to specific chemical species (9). In principle, the MZI is more sensitive than waveguide surface plasmon resonance (SPR) based sensors (10), primarily because it does not employ coupling to a lossy waveguide, although exploitation of this enhanced sensitivity may require the sensitive region to be longer. Furthermore, the MZI may be rendered sensitive over a wider range of superstrate indices, as it does not employ "resonant" coupling between two dissimilar waveguides but, in effect, directly measures modal velocity changes due to changes in refractive index in the evanescent field of an unisolated waveguide compared with a waveguide isolated from the analyte. Highly sensitive MZI immunosensors have already been demonstrated, for example by Heideman and Lambeck (11), and this work has concentrated upon achieving sensitive operation over a wide range of indices, enhancing the sensitivity of ion-exchanged devices using high-index overlayers (12), and investigating the simple and reliable incorporation of these sensors into instrumentation.

The aim of the research work (13) was to realise an integrated refractometer chip for incorporation in practical instrumentation, for measurements in analytes having a wide range of indices. The MZI has been chosen as it is straightforward to design and fabricate, and is tolerant of manufacturing error. The design adopted incorporates (i) thin tantalum pentoxide (Ta_2O_5) films to enhance sensitivity, (ii) a high-sensitivity MZI and

a low-sensitivity MZI to allow the combination of high sensitivity with wide index range, (iii) 3 x 3 output couplers from each MZI to ensure sensitive operation over the entire index range and to remove ambiguity in the direction of index change, and (iv) reference waveguides with and without analyte windows, to allow compensation for the effects of input power fluctuations and potentially to determine analyte absorption.

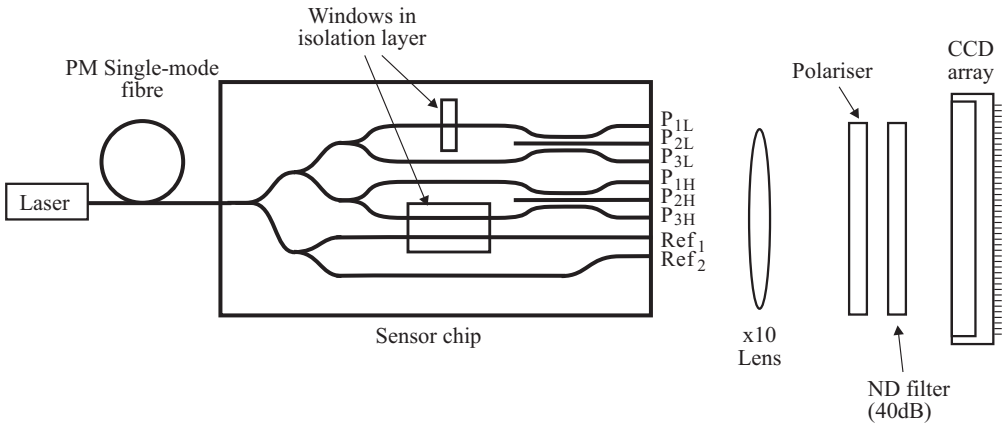

FIGURE 1.1: Integrated optical dual Mach-Zehnder interferometer sensor system.

Figure 1.1 shows the schematic diagram of a typical device and outline measurement system. Light is coupled into the sensor chip using a mono-mode fibre and the power is divided equally into a "left branch" which feeds the two interferometers and a "right branch" for referencing purposes. Power in the "left branch" is split again to feed the two interferometers and then again into the two arms of each interferometer. In each interferometer, the relative phase of the light in the two paths combining at the 3 x 3 directional coupler depends upon the refractive index of the analyte in the window in the isolation layer which otherwise covers the entire device. One MZI has a window 10 times shorter than the other, resulting in a sensitivity 10 times lower, in order to remove ambiguities due to the periodic nature of the response to index for large index changes. In a conventional MZI, the light is recombined in a simple Y-junction, resulting in an output which varies periodically with relative phase, with excess power being scattered into the substrate. Sensitive transducer response to small changes in analyte index requires that the device must always operate in a sensitive region of the response curve. This cannot be satisfied over the entire range of indices for a single-output MZI, which shows maxima and minima in the interference function. The use of a three-waveguide coupler, described in detail in (14), results in three outputs, with the interference functions shifted by nominally 120° with respect to each other. In this way at least one output yields

a sensitive response to small index changes whatever the baseline index is. While use of 3 x 3 directional couplers tightens the constraints on manufacture somewhat, it also allows referencing the individual signals to the sum of the signals emerging from the three outputs, assuming negligible variation in total loss as power is distributed among them, thus removing the effects of source intensity fluctuations.

Two reference outputs are provided; the first is isolated from the analyte for its entire length, allowing simple removal of the effects of input power fluctuations and to eliminate the effects of analyte absorption. The second reference waveguide is exposed to the analyte through an identical window to that of the high-sensitivity MZI, yielding a direct measurement of the loss due to the window and analyte. In the presence of optically absorbing analyte media, this reference output may be used to estimate the optical absorption of the analyte by comparison with the first reference channel. The whole chip may be coated with a thin film of a robust high-index material, such as Ta_2O_5 in order to increase the sensitivity of both MZIs and the exposed reference waveguide. A phase resolution of 0.3° was obtained for the sensor coated with 30nm Ta_2O_5 film. This corresponds to a minimum detectable analyte index change of 2.6 x 10^{-5} for a device operating in a sensitive region of its characteristics (or with an optimised 3 x 3 directional coupler) or a change in the modal effective index of approximately 6 x 10^{-8}.

With the developments in the semiconductor industry, integrated optical sensors have become more important in the direct detection of biomolecular interactions. This approach advances to mass production as well as the fabrication of nano-/macrosystems on the same platform by hybrid integration of sources, sensors, photodetectors and complementary metal-oxide semiconductor electronics, which is achieved by using silicon microelectronics technology (15; 16; 17; 18; 19). An integrated optical interferometric nanodevice, based on silicon technology, for biosensor applications has been reported (15). This device is based on evanescent field sensing in conjunction with a Mach-Zehnder interferometer (MZI) for increased sensitivity, in which a phase shift between the sensing and the reference arm is induced by a biomolecular reaction that causes an intensity modulation at the sensor output. The integration of semiconductor Vertical-Cavity Surface-Emitting Lasers (VCSELs) and PIN photodetectors for biomedical fluorescence sensing (17) sets a good example in terms of applying semiconductor technology into the sensor area. The VCSELs, optical emission filters, and PIN photodetectors were

fabricated as part of a monolithically integrated, near-infrared, fluorescence detection system. These micro-fabricated components with micro-arrays, flow channel arrays, and biochips are integrated to form a complete sensor, and the integration of all these components can drastically reduce costs and enable parallel sensing architectures.

Fluorescence-based array biosensors (20; 21; 12; 22; 23) hold much promise, due to their high specificity and tolerance to temperature changes and to non-specific binding, compared to refractive index based sensors. Current trends in the development of these biosensors are towards the application to the real environmental samples, and also taking into consideration aspects such as sample pretreatment, matrix effects and the validation of biosening measurements. As an example, a planar array immunosensor was used to detect multiple toxic agents. The structure of the biosensor is a patterned glass slide with covalently bound antibodies placed on the surface, evanescently illuminated by 635nm light from a diode laser. Bound antigens are detected in the sandwich assay format, where Cy5-labeled antibodies are used as the reporter antibody. The identity and amount of toxin bound at each location on the slide were determined by quantitative image analysis. The biosensor is able to detect quantities of three different toxins (ricin, Yersinia pestis and staphylococcal enterotoxin B) in the sub-nanomolar range ($ng.mL^{-1}$) simultaneously (6). It was the same research group who extended the detectable analytes up to 9 targets with the same detection level (24). It has also been reported, by researchers at Zeptosens AG in Switzerland, that a grating-coupled Ta_2O_5 thin-film (thickness $\leq 1\mu$m) on a glass planar waveguide array biosensor has shown a sensitivity improvement of about two orders of magnitude compared to conventional fluorescence excitation and detection systems (25). In conventional fluorescence excitation configurations, the part of the optical path with high excitation intensities is much larger than the beam waist (typically, four to six times larger, the beam waist is about 10μm to 30μm) and deeply penetrates the bulk medium. In contrast, for surface-confined excitation associated with light-guiding in an optical waveguide, the penetration depth of the evanescent field into the adjacent media is only some hundred nanometres.

The transducers used in the above experiment had a 320nm period diffractive relief grating. The resonance condition for red light coupling (635nm) is met at a launching angle of -10°. Consequently, under coupling angles between -20° and +30°, excitation light

covering the whole visible spectrum (from 450-700nm) can be coupled into these waveguides. This was allowed the use of all current commercially available fluorescence labels that can be excited in the visible range. Compared with the conventional fluorescence excitation configurations, there are a number of advantages of using the fluorescence excited via evanescent field where the light is coupled into the waveguide by means of gratings. Firstly, the location of launching the excitation light onto the coupling grating is a distance away from the area where the analyte fluorescence is excited. So, it is easy to discriminate the excitation light, in contrast with the classical configurations, where the areas of launching the excitation light and of fluorescence generation are identical. Secondly, the main critical and important parameter for light coupling using a grating, is the match with the coupling angle in order to satisfy the resonance condition, not the distance between the planar waveguide surface and the excitation light source, e.g. when using a parallel excitation light. Thirdly, it is more tolerant towards the roughness of the waveguide surface. For example, there is no effect on the available excitation light intensities in the range of more than 10-50μm, deviation from a perfect surface flatness over macroscopic distances, if the thickness of the waveguide layer remains constant and no light scattering is generated. This is in contrast to the described classical fluorescence excitation configuration. Fourthly, the system allows the use of multiple laser light sources emitting at different wavelengths, so more fluorescence labels can be applied for analyte detection in assays using the system. In addition to the above, the excitation field is not only more sharply confined to the sensing surface (by at least one order of magnitude compared with the convention excitation schemes), it is also simultaneously available along the whole propagation length of guided excitation light in the waveguide. Therefore, simultaneous fluorescence excitation on macroscopic surfaces combined with very high spatial selectivity of the excitation step (with respect to distance from the interacting surface) is enabled. Furthermore, real-time studies of the kinetics of analyte binding to the surface are enabled, which cannot be performed with scanning systems due to sequential excitation and detection along the scanned areas (25).

An important factor in biosensor construction is the development of immobilisation technologies for stabilising biomolecules and applying them to surfaces. Since the pioneering work of the incorporation of biological components in membrane structures was first described by Clark and Lyons (1962) (26), in which an enzyme-based glucose sensor was developed by the entrapment of glucose oxidase in a membrane enclosed sandwich, there

have been a number of methods which have been described for the immobilisation of enzymes and proteins on surfaces and within various matrices (12). The main methods of immobilisation are: a) physical or chemical adsorption at a solid surface (27); b) covalent binding to a surface (28; 29); c) entrapment within a membrane, surfactant matrix, polymer or microcapsule (30); d) cross-linking between molecules (31) and e) sol-gel entrapment, Langmuir-Blodgett (LB) deposition and electropolymerisation (32).

As mentioned in Section 1.1, the immunochemistry used in this research work is binding inhibition assay, which requires antibodies directed against specific analytes and analyte derivatives that can be covalently bound to a transducer surface. The previously immobilised aminodextran layer is used to reduce non-specific binding to the surface (33). Dried (immobilised) aminodextran layers on a glass substrate showed a thickness between one and three nm. The thickness of welled aminodextran layers were also verified by spectroscopic ellipsometry experiments and these experiments yielded values between 100 and 150nm. A huge number of polyclonal antibodies and their corresponding analyte derivatives have been produced for a variety of organic micro-pollutants. After being purified and labelled with a fluorescent marker, they were developed into immunoassays and used in this work. The sample containing the analyte is incubated in solution with the labelled specific antibody. Therefore, the antibody binds the analyte during the incubation step until a well-defined condition of the reaction is reached. When the sample is pumped over the sensor surface, only the antibodies with free binding sites can bind to the surface (33).

The development of biosensors has become more targeted towards integration in recent years, both in the variety of analytes detected (34; 35) and in the compactness of the sensing area, particularly for molecular arrays (36) and lab-on-chip devices (37; 38; 39). The standard of quantitative sensitivities has also been pushed to the lower levels required for clinical diagnostics (40), environmental monitoring (41), biohazard detection (40; 42). Optical methods play a significant role in all of these biosensors. The CCD detector (43), as an integral part of a biosensing system, has become very popular in recent years due to a few distinct advantages, such as the ability to image multiple zones on the sensor, the flexibility of defining the sensing configuration and the low noise performance of the detectors.

The trends of development of biosensors have strengthened the role of CCD detectors as part of the overall optical biosensor configuration. There are some research groups that use CCDs (44; 45; 46; 47; 48), while others use a CMOS-based system (49; 50) or photodiode arrays as the detection system(49; 39). After direct comparison of these three detectors, the CCD exhibited significantly better signal-to-noise and thus better discrimination of targets at a lower concentration than the CMOS and photodiode detectors(49). However, CMOS detectors are continually improving and have the advantage that the signal from each pixel is already digitised, which simplifies data acquisition. Photodiodes have proven to be useful for economical single point detection sensors. However, in situations where there are more complicated arrays of analytes, the tradeoff between ease of use and cost becomes more apparent(49).

1.3 Outline of the work

The main focus of the work is on developing a biosensor that employs fluorescence-based detection of the binding of tagged biomolecules to the surface of an optical waveguide chip. The fibre-pigtailed chip consists of a channel waveguide circuit which distributes excitation light to 32 separate sensing patches on the chip surface. Bio/immunochemistry may be used to sensitise each of the 32 patches to a specific analyte, and a microfluidic system is used to automatically handle the sample injection over the sensor surface, thus enabling rapid, simultaneous and high-sensitivity fluorescence detection of up to 32 pollutants. A fibre-coupled detection array monitors the 32 separate fluorescence signals, and the software controls the laser, fluidics, data acquisition and processing for the fluorescence signals and records the laser power and ambient and chip temperature.

A thorough study was undertaken theoretically and experimentally in order to optimise the sensor chip design, fabrication and sensing system. The surface intensity of the sensor region was also studied in depth, based upon BPM simulation of waveguides which gave the optimum fibre to waveguide coupling efficiency. The total power which will be emitted by fluorophores was estimated, which allows proper design of the fluorescence detection system.

Optics, electronics and fluidics are the three major parts of the instrument in terms of hardware requirements for the multi-sensor system. The photodiode-based detection schemes which consists of the photodiodes with integral amplifiers and an amplification and prefiltering stage, were experimentally evaluated for cost, noise, stability and detection limit.

The system detection limit was estimated theoretically based on immunoassay characteristics, and an equivalent detection limit of the system for dye solution was also predicted. Subsequently, extensive bulk dye fluorescence measurements were carried out, in order to confirm low-noise operation of the detection system and determine an ultimate detection limit in terms of the number of Cy5.5 molecules per unit area.

This thesis also addresses experimental results for the detection of a key pollutant, estrone, in water. Estrone pollution is potentially deleterious to human and animal wellbeing, due to its hormonal activity, and arrives in waterways as a byproduct of pharmaceuticals and contraceptive formulations. A characteristic immunoassay calibration curve has been generated that yields a lower detection limit of 1 ng.L^{-1} with a range (without dilution) up to about 1 μg.L^{-1}. Water samples can be analysed directly, without concentration or complex extraction techniques.

In addition, a detailed study was also carried out theoretically and experimentally in investigating a CCD detector system, an alternative detector system for the purposes of this research work. Direct comparisons between these two detector systems were also presented.

1.4 Structure of the thesis

The first chapter gives a brief introduction of the aims of the work and the structure of the thesis. It also describes the background of the optical biosensor technology and summarises the current status or the level of development in this field.

Chapter two describes how the optical sensor chip has been researched, including: mask design: layout, parabolic tapers' design and simulation, estimation of the power budget of the system, optimisation and characterisation of fabrication process parameters, fibre pigtailing, preliminary test samples' fabrication, optical loss measurement, optimisation

of silica isolation layer, Ta_2O_5 film, and a detailed study on fibre to waveguide coupling efficiency.

Chapter three describes the instrumentation and the system, which includes: the system overview and experimental setup, optical power estimation, optical component selection and testing, detection system and experiment, such as preliminary test of the photodetector/amplifier and assembly of a complete system and the system operation. In addition, a detailed study was presented on electronic signal filtering and processing, in order to justify the suitability of the selected filter for the system.

Chapter four addresses the fluorescence measurements and sensor chip characterisation, dye experiment, limit of detection (LOD), patch to patch uniformity, and a direct comparison of the sensor chips with and without a Ta_2O_5 film. Detailed comparison of theoretical and practical results are presented.

Chapter five describes the surface chemistry modification and estrone calibration experiment, including the calibration curve and LOD. This chapter also presents the multi analyte measurements as well as providing a direct comparison of the sensor system with conventional analytical techniques. In addition, this chapter also addresses the results of data processing in order to verify whether the data collected via the system would be affected by the influence of the presence of the photobleaching.

Chapter six addresses a detailed study on various aspects of the instrumentation of a CCD detector system, including the system overview and operation, the difference between the CCD and photodiode detectors, the collection efficiency of the CCD detector system and a comparison with the photodiode array system, estimation of the power flow, and Signal to Noise Ratio (SNR) and NEP analysis, as well as the result of the fluorescence measurement on bulk dye Cy5.5 and the detection limit of the system for Cy5.5. Detailed comparisons of theoretical and practical results are also presented.

Chapter seven presents the overall conclusion and highlights the remaining problems, the next steps and future directions.

Chapter 2

Sensor Chip Design and Fabrication

2.1 Introduction

The purpose of this chapter is to describe the design and fabrication of a sensor array chip with low loss and high signal strength. The literature was reviewed to determine the glass substrate materials and ion-exchange waveguide fabrication procedures appropriate for low-loss waveguides, with a modal spot size similar to that of optical fibre at 635nm, which would yield high surface intensity for the excitation of fluorescent molecules on the surface. Potassium ion-exchange in BK7 was selected to give a good index match to optical fibre and provide adequate surface intensity.

A dilemma is that the high signal strength will be accompanied by photobleaching of the dye molecules, thereby reducing the sensitivity of the device. In this study, a tapered waveguide section is introduced into the sensor chip design in order to reduce the power density of excitation radiation at the sensing surface and hence reduce the rate of photobleaching whilst maintaining the overall signal strength and the sensitivity of the device.

In order to achieve the best fibre to waveguide coupling, a thorough study was undertaken experimentally and mathematically. The surface intensity of the sensor region was also studied in depth, based upon BPM simulation of waveguides which gave the

optimum fibre to waveguide coupling efficiency and, finally, the total power which will be emitted by fluorophores was estimated to allow proper design of the fluorescence detection system.

In this chapter, a detailed optimisation of chip design and the fabrication process is presented, with the aim of achieving low loss and high signal strength for the sensor array chip. Estimation of the power budget through the sensor device is discussed in order to provide information to select the detection system, which will be described in the next chapter.

2.2 Optical circuit layout and mask fabrication

2.2.1 Design of curved waveguides and splitters

The optical waveguide circuit was designed using OlympIOs software and using the Beam Propagation Method (BPM) to ensure low-loss and adiabatic tapering. The software enables photolithographic mask design as well as the simulation for the adiabatic tapering and the optical power flow within the device.

The sensor chip design contained 32 sensing spots, as defined by the AWACSS project partners to detect 32 primary pollutants in river water (4). The partners with responsibility to realise the instrument, CRL and Siemens, decided that for the AWACCS project, 1mm diameter fibre would be used underneath each sensor patch for the collection of fluorescence, rather than using a CCD camera, for reasons of cost.

Potassium ion-exchange in BK7 glass was chosen for the fabrication of the waveguide sensor chip. BK7 has good optical quality and exhibits low fluorescence and the potassium ion-exchange process produces low loss waveguides, uses low cost materials and fabrication procedures, and had already been optimised for low loss coupling from optical fibres resulting in minimisation of scattered light in the substrate (51). In addition, waveguides made by ion-exchange have a flat surface, which is suitable for the attachment of flow cell, while other methods of making waveguides, such as by etching results in a non-planar surface unsuitable for applying a flow cell.

A silica isolation layer of approximately 1μm thickness was sputtered onto the sensor chip, with 32 windows being photolithographically defined in this film over the waveguides. The isolation layer prevents excess losses due to contact with the flow cell and environment outside the sensing regions. The evanescent intensity decays exponentially with increasing distance from the interface with an evanescent penetration depth of approximately 150nm in this case (a detailed calculation is given in Section 4.4.2.1). A silica thickness of 1 micron results in a surface intensity of approximately 0.1% relative to that directly on the waveguide surface, providing acceptable isolation of the waveguides from the analyte.

The sensing spot dimensions were chosen so that the emission falling upon the collection fibre end was within the collection cone of the fibre underneath each spot, in order to maximise the collection efficiency. The numerical aperture (NA) of the 1mm diameter fibre underneath the sensor patch is 0.51±0.3 and, taking the thickness of the substrate to be 0.8 mm, the length of the sensing window is chosen as 1.5mm, to ensure that light emitted from any point on the sensing window which falls on the fibre end-face is within the NA. The selection of the window width was based on the consideration of the waveguide width and the separation between the waveguides. Since the width of the taper section of the waveguide is up to 60 μm (section 2.2.2), 70 μm is the minimum possible window width to allow for alignment tolerances. The maximum window width is 0.8mm, to ensure that the window does not cross the adjacent waveguide. 0.3mm was chosen as the window width within this range.

An adjacent sensing patch in a multisensor must be placed to avoid crosstalk, so that it must not be within the collection cone of any other collection fibre. To avoid unnecessary breakthrough of additional pump scattering from adjacent waveguides, adjacent waveguides should also not pass through the collection cone of an adjacent fibre. The minimum waveguide spacing allowing for alignment tolerances is therefore 0.85mm, and 1mm was chosen for convenience and to ensure that the curved waveguide sections, which depend upon required separation, were not significantly longer than necessary. This waveguide separation ensures that no direct crosstalk and no direct pump scattering enters adjacent fibres. It was decided that the sensing patches should be laid out in the staggered configuration as shown in Figure 2.2 to allow easy machining and assembly of the block holding the 32 fibres.

The final step in the layout was to decide the number of rows and columns in the sensor patch array, and this was dictated by compactness, maximum chip size and surface intensity. To ensure low waveguide bend radius and hence low waveguide loss, a 1 x 2 waveguide splitter requires a length of 10mm and the 60 micron tapers for reduced photobleaching also require 10mm, as described in section 2.2.2). The maximum chip length is 75mm, defined by the mask aligner exposure area, but total of 8mm clearance is used at both ends to avoid edge effects in the photolithography and for cutting and polishing, so that the maximum device length is 67mm.

Consideration of patch length, patch spacing, splitter length and taper length, and the maximum chip length restricted the design for a 32 patch device to a 4 x 8 (or 8 x 4) array with either a 4-way splitter (20mm) or an 8-way splitter (30mm). The 4 way splitter and the design shown in Figure 2.2 was chosen to maximise the surface intensity at each patch for a given laser power, assuming that waveguides and sensing patches would exhibit low loss.

Three chip designs were reproduced on each wafer, and the size of each chip was set at 15mm x 67mm after considering any restrictions of the fabrication conditions in the ORC, for example, the maximum diameter of the wafer for the mask aligner of 75mm. Each design consists of (i) an alignment and sawing mark level, which will be used to align successive photolithographic stages and to guide the dicing of the chips; (ii) a waveguide level, which defines the waveguide circuit, including 1x4 splitters and tapered sections designed for adiabatic transformation of the mode and reduction of photobleaching, and (iii) an isolation layer level which isolates the waveguide from the analyte and flow-cell, except in thirty-two 1.5mm long and 300μm wide windows where the specific chemical will be deposited and the fluorescence excitation will take place. The wafer layout is given in Figure 2.1. Figure 2.2 shows a schematic diagram of a sensor design. The 32 windows were designed as a staggered array in order to use the area effectively and to reduce the crosstalk. In addition to these sensor devices, there are two sets of straight waveguides with different widths (from 1.5μm to 3.5μm with a constant increment of 0.5μm on each side of a single chip) as shown in Figure 2.1. One set of straight waveguides will be covered with a silica isolation layer and one will not, in order to characterise the fabrication conditions and hence to optimise waveguides for

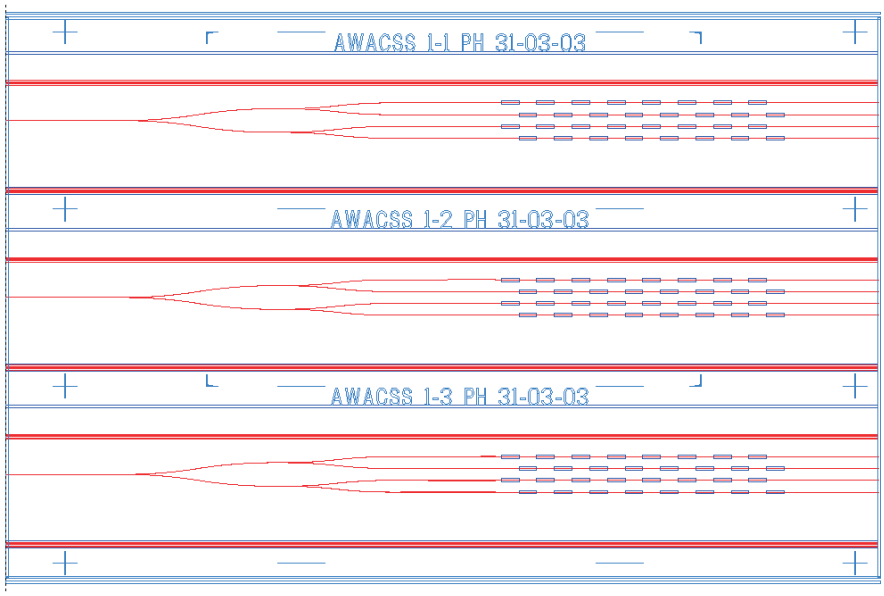

FIGURE 2.1: Wafer design comprising 3 chips.

transmission loss, the waveguide opening, fibre to waveguide coupling efficiency and the silica isolation layer.

2.2.2 BPM analysis of tapered waveguide structures

Since the sensitivity of the device will be reduced if significant photobleaching of the dye molecules occurs under the high optical intensity, it is necessary to keep the photobleaching rate level sufficiently low, by reducing the optical field power density, such that signals can be collected before they fade away. In this study, a taper section is employed to broaden the waveguide in order to reduce the power density of excitation radiation at the surface of the waveguide hence reducing the rate of photobleaching. Decreasing the rate of photobleaching offers two distinct advantages. Firstly, data acquisition becomes more straightforward as the fluorescence signal changes less rapidly. Secondly, a wider waveguide increases the number of bound fluorophores excited during the measurement leading to a greater measured signal. This second advantage is expected to lead to an increased signal to noise ratio, and hence an improved detection limit for the sensor (52). Theoretical modeling of tapered waveguides has been carried out using a commercial beam propagation method (BPM) package. The Finite Difference (FD) method is used with the software package. The FD method is based on discretisation of the 2D field equation that lies in the waveguide cross-section plane.

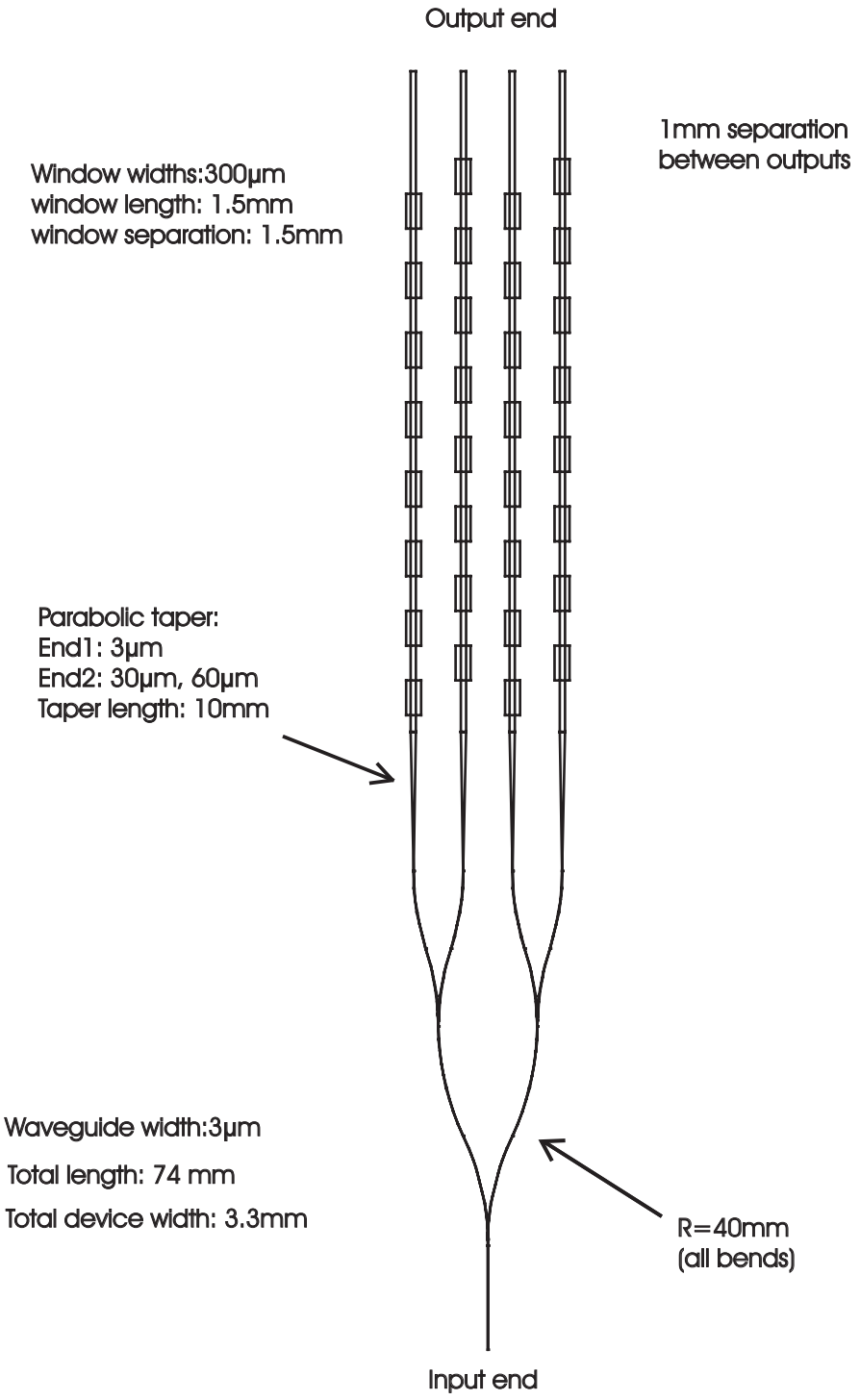

FIGURE 2.2: Schematic diagram of the sensor layout.

In order to maintain a uniform power distribution in a wide, and hence highly multi-moded waveguide, it is desirable to excite only the fundamental mode which is the lowest-order spatial mode of a channel waveguide. If the rate of increase in the width

of the waveguide is slow enough, the broadening of the modal field is essentially adiabatic and results in all of the launched light remaining in the fundamental mode of the waveguide. The concept of using tapered waveguides, to couple from broad to narrow channel waveguides, is well established. Various designs for the adiabatic expansion of the fundamental mode of a channel waveguide have been described in (53). A parabolic shaped taper can give a low-loss expansion to a width W if the length L satisfies the following condition (53):

$$L \geq \frac{W^2 n_m}{2\lambda} \tag{2.1}$$

Where n_m is the mode index, λ is the free-space wavelength, and the initial channel width is much smaller than W. Therefore, for a 0.633μm mode in BK7 glass ($n_m \sim 1.51$), a 100μm width can be reached in 12mm, and a 60μm width can be reached in 8mm.

A theoretical study and a simulation using BPM were carried out with taper widths of 30μm, 60μm and 100μm. A transition length of up to 10mm was studied for use in 67mm long waveguide devices. The device length is limited by the following factors:

- The cost of the glass substrates;
- The fabrication procedures, for example, the mask aligner used for the photolithography process;
- The sensor structure, i.e. whether the transition length of the taper section is sufficiently long to incorporate the required number of sensing patches.

Figure 2.3 shows that the peak intensity of radiation in the 3μm guide may be reduced to 8% of its initial value if the guide is broadened through a taper to a final width of 60μm.

Figure 2.4 shows the fundamental mode propagation from the narrow channel through the transition section in the case of a taper to 100μm. The power was not evenly distributed, compared to the result for the 60μm width taper (Figure 2.3), because the 10mm transition length is shorter than that required, which results in the excitation of the next even high order mode of the waveguide and the high order mode beating along the propagation direction causing the uneven power distribution. Figure 2.5 shows the

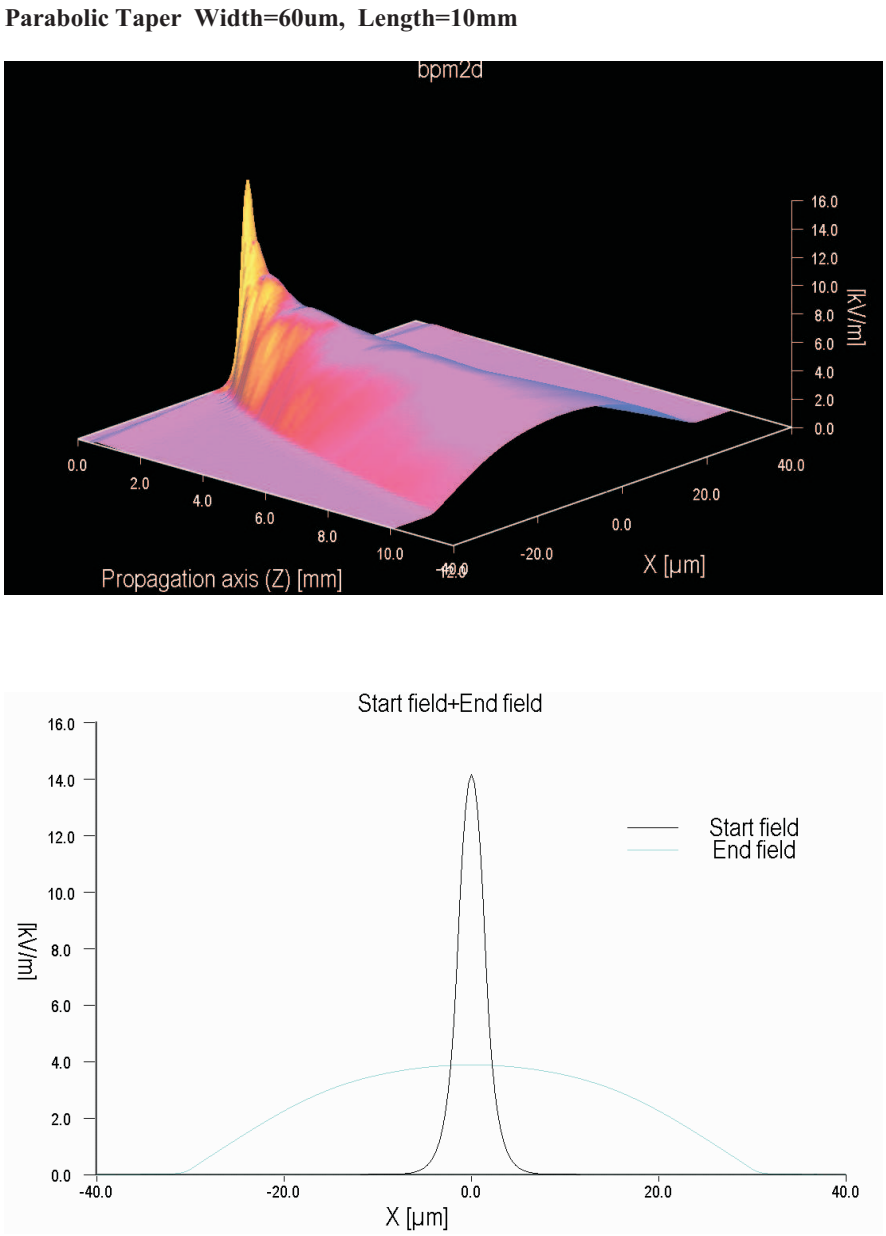

FIGURE 2.3: Taper width is 60μm and length is 10mm. Top: Electric field distribution along the taper. Bottom: the start field and the end field.

mode power evolution along the taper length in these two cases. Therefore, the taper width of 30μm and 60μm were chosen for the final mask design, to avoid significant excitation of higher order modes while keeping the taper length to 10mm, due to chip size constraints.

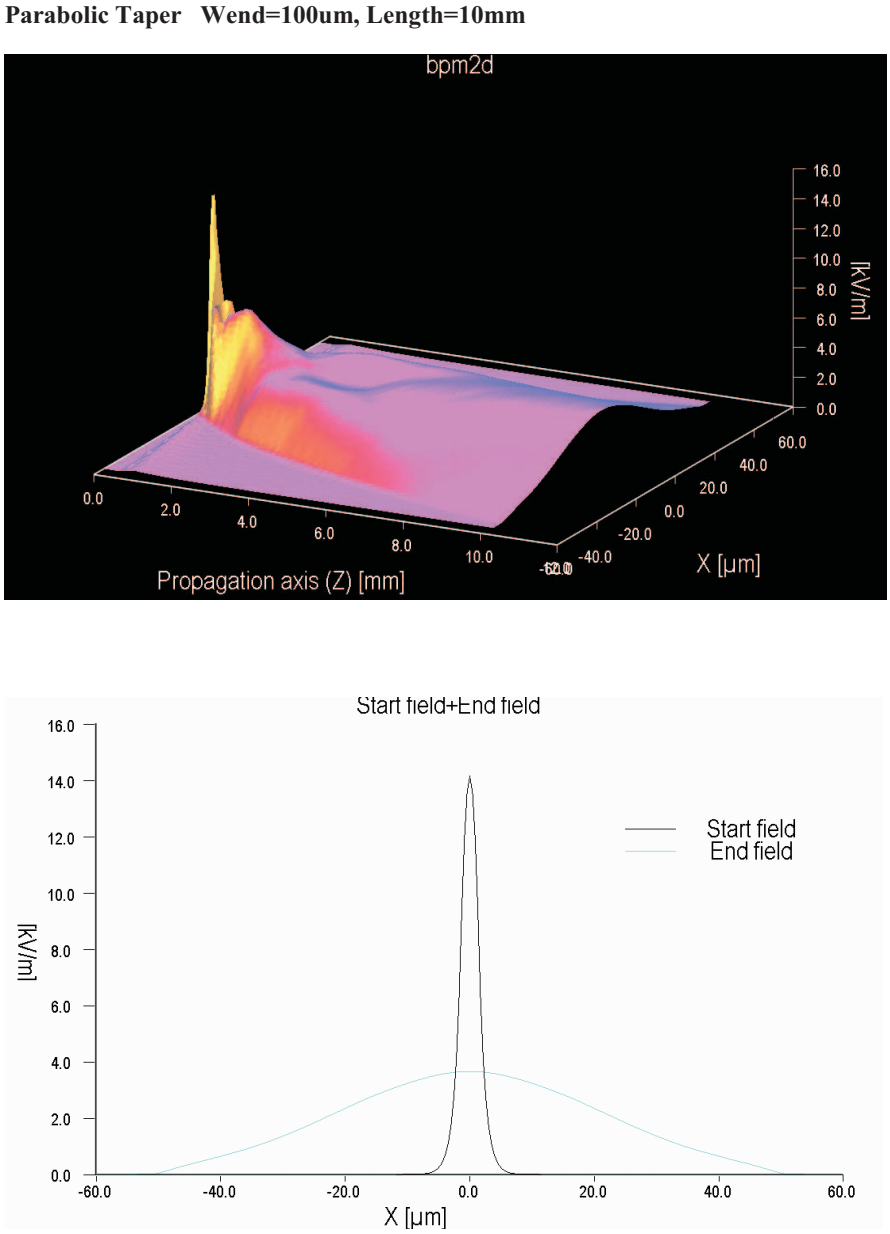

FIGURE 2.4: Taper width is 100μm Length is 10mm. Top: Electric field distribution along the taper. Bottom: The start field and the end field.

2.3 Optimisation of the fabrication process

2.3.1 Preliminary test waveguides' fabrication and optimisation

In order to determine the optimum production process for the sensor array chip, with low loss and high signal strength, a set of preliminary test waveguides was realised by potassium ion-exchange (IE) in BK7 glass (54), with widths between 1.5 and 3.5

Parabolic Taper Wend=60um, Length=10mm

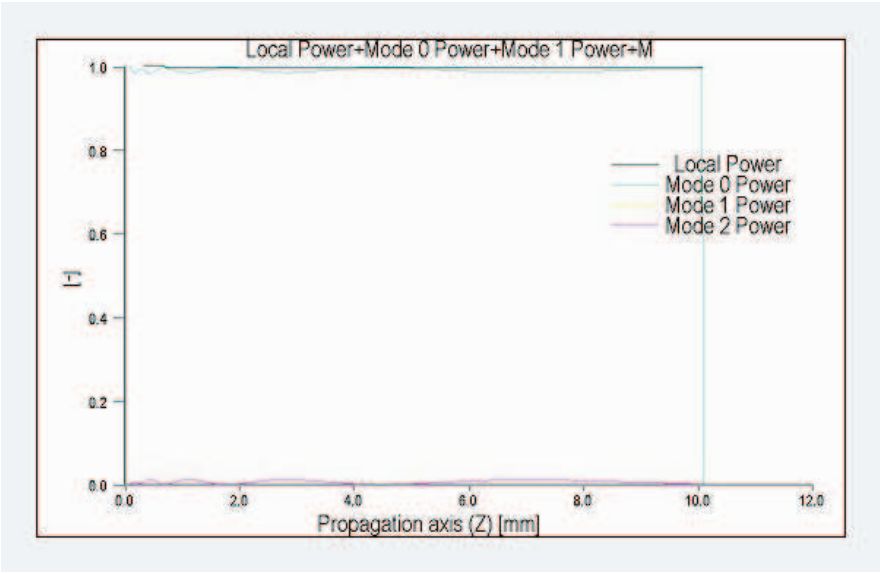

Parabolic Taper Wend=100um, Length=10mm

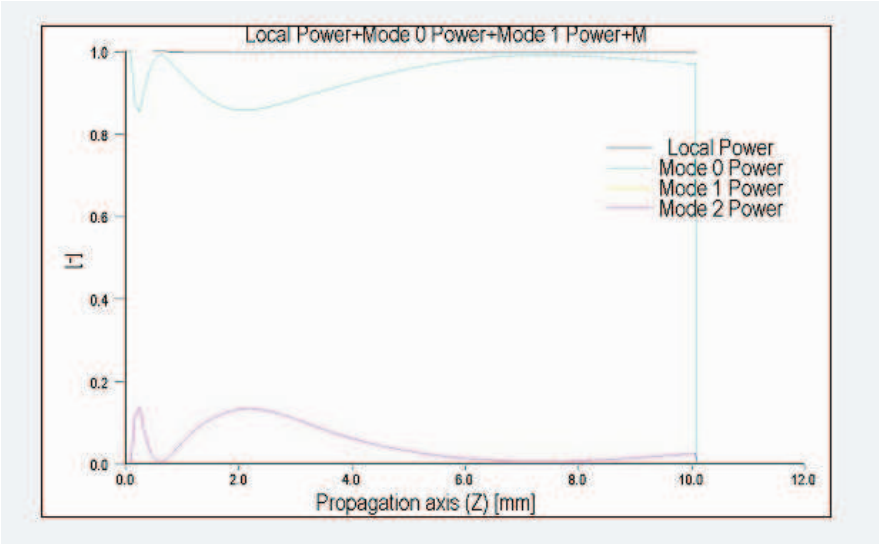

FIGURE 2.5: The mode power evolution along the taper length in 60μm taper (top); and in 100μm taper (bottom).

microns for diffusion times of 1.25-2.0 hours in molten KNO_3, at 400 °C. The size of the BK7 glass substrates was 50mm by 50mm; the reason for choosing this size, as preliminary test samples, was simply because they were available at the time the project started. Although these glass substrates were not long enough for the sensor device, they were sufficient for the purpose of establishing and optimising the fabrication process. An aluminium masking film was deposited on the substrate, and the waveguide

circuit was defined by opening tracks of 1.5 μm width in this film using conventional photolithography. Transmission measurements were carried out between all these test samples, using a pigtailed semiconductor laser emitting a power of $3mW$ @ 635nm (Point Source). The transmitted light power, from a semiconductor laser on its own and through the waveguide were recorded by a power meter, and the waveguide transmission loss in dB was calculated. Figure 2.6 shows the transmission loss against ion-exchange

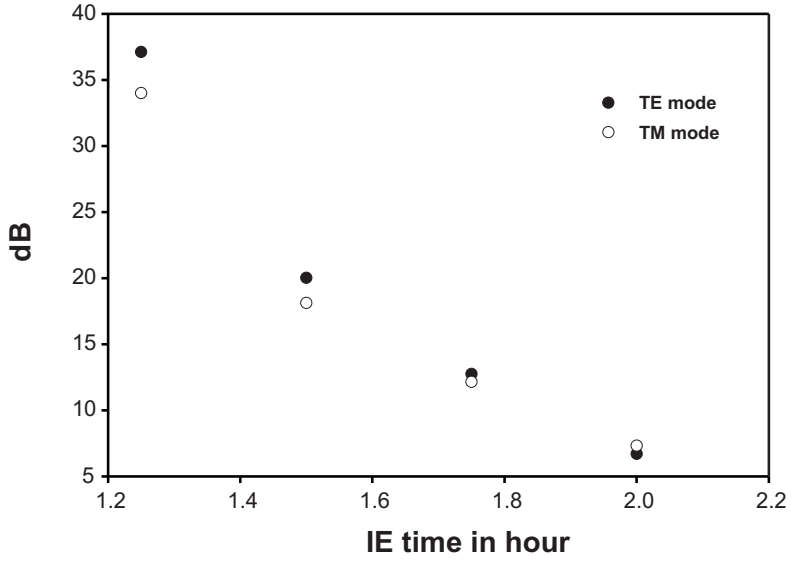

FIGURE 2.6: Excess coupling and propagation loss in device with the waveguide width of 3μm against IE time.

time for 3μm width waveguides, as an example. Note that the 6dB loss, due to the 4-way division, has been deducted from the total loss. Therefore the remaining loss is comprised of the excess loss due to modal mismatch, Fresnel loss due to reflections, propagation loss and misalignment.

In a conclusion, a set of preliminary test waveguides were realised, and the optimum condition for fabrication of low loss, single mode at 635nm and high signal strength waveguides has been established. As an example, for a 3μm waveguide opening, the optimum IE time is 2 hours.

2.3.2 Modal intensity profiles and fibre to waveguide coupling efficiency

The ultimate device discussed in this thesis would be a portable type of instrument which requires the sensor chip to be pigtailed with a fibre; this allows easy connecting

and coupling of light from a laser source. The purpose of this section is to optimise the fibre to waveguide coupling efficiency, thus enabling the optimisation of the sensor chip design.

The waveguide modal intensity profiles were measured and compared with the Point Source polarisation maintaining fibre, to be used for pigtailing. The modal intensity profiles were recorded using a CCD camera, measured with a micro-ruler under a microscope, and processed with a Vision XL software package. Overlap integrals were performed between the measured fibre field and the waveguide field, using equation 2.2, in order to predict the expected coupling losses for perfect alignment and thus obtain fibre-waveguide coupling efficiency, according to equation 2.2 (55):

$$\eta_c = \frac{[\int_{-\infty}^{\infty}\int_{-\infty}^{\infty} E_f(x,y)\, E_g(x,y)\, \mathrm{d}x\, \mathrm{d}y\,]^2}{\int_{-\infty}^{\infty}\int_{-\infty}^{\infty} |E_f(x,y)|^2 \mathrm{d}x\, \mathrm{d}y \int_{-\infty}^{\infty}\int_{-\infty}^{\infty} |E_g(x,y)|^2 \mathrm{d}x\, \mathrm{d}y} \tag{2.2}$$

In equation 2.2, η_c is the predicted coupling efficiency, $E_f(x,y)$ is the fibre field profile, and $E_g(x,y)$ is the waveguide mode field profile. Strictly speaking, $|E|^2$ is not equal to intensity, as there should be an impedance term present. However, we can use $|E|^2 \equiv I$ since the impedance term occurs on both the top and the bottom of the expression. Figure 2.7 shows how the fibre mode profile and waveguide mode profile evolve with ion-exchange duration.

Fibre-waveguide coupling measurements were made on these waveguides to confirm the optimum fabrication condition for fibre coupling. Table 2.1 gives mode dimensions of sets of straight waveguides, with waveguide widths from 1.5 μm to 3.5 μm, and the optical fibre (Table 2.2) to be used for fibre pigtailing.

X and Y in the Table 2.1 represent mode widths parallel and perpendicular to the waveguide input edge respectively. The mode width was defined as the width where the peak value falls to $1/e$ of its peak value. The table also gives a predicted coupling efficiency, calculated using equation 2.2, based on these measured mode profiles of fibre and the sets of straight waveguide with IE time from 1.25 hour to 2 hours. Both TE and TM modes were investigated. The best coupling efficiency, of 80.2% in the TE mode, was achieved and corresponded to the fabrication conditions of 2.5 μm waveguide opening and 2 hours of IE.

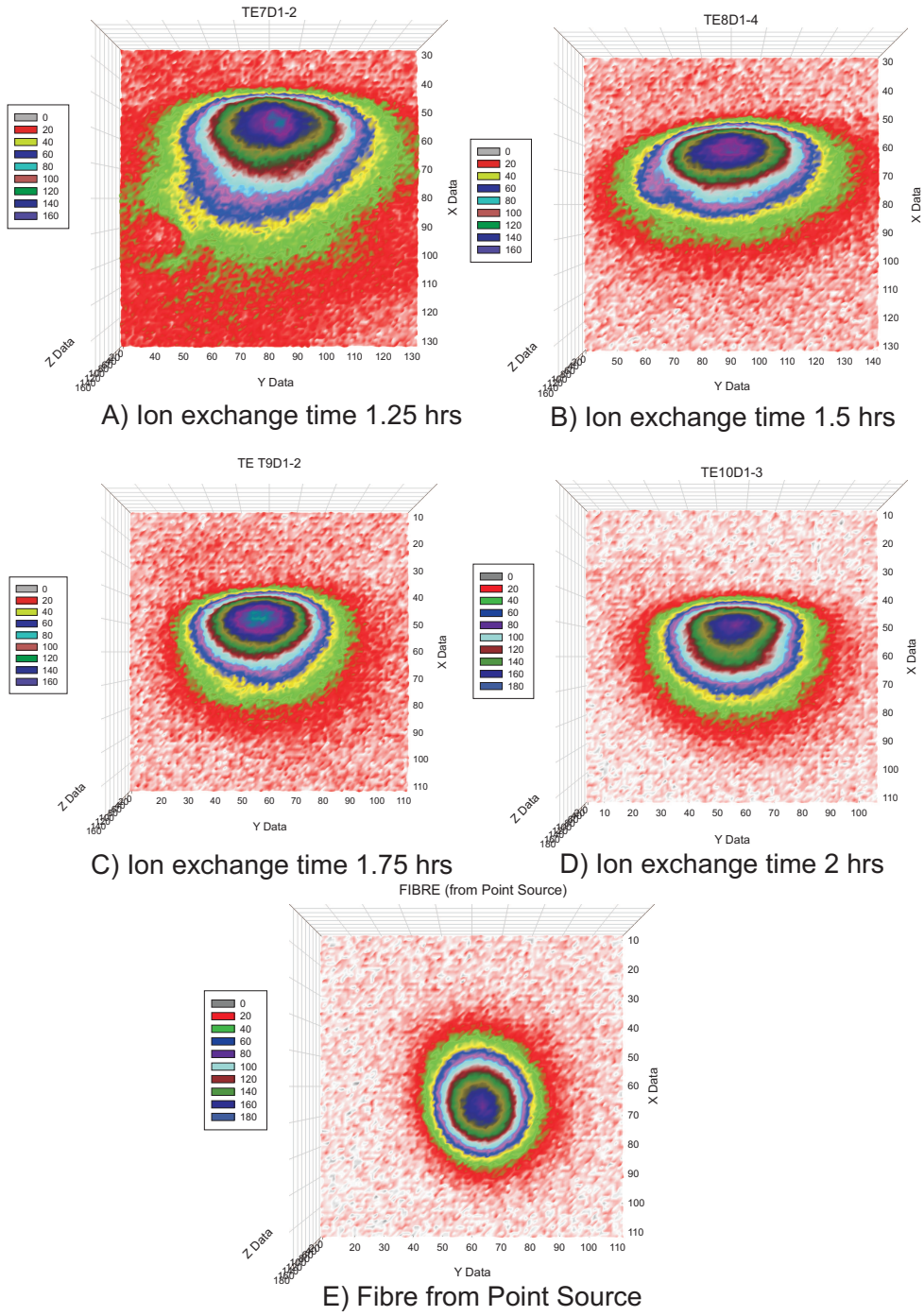

FIGURE 2.7: A)-D) waveguide (TE) mode intensity profiles (2D) with different IE time. E)Fibre from Point Source type(FDS-P-2-P-635-FCP-FCP). Note: The images show areas 10 μm square on the CCD where each unit on the x and y axis represents 0.1μm.

Figure 2.8 shows the calculated coupling loss, for different waveguide widths and IE times, in dB and for the TE mode only.

Figure 2.9 shows the direct comparison of the calculated coupling loss in dB with the

		Samples			
WG Opening		T7(IE1.25h)	T8(IE1.5h)	T9(IE1.75h)	T10(IE2h)
1.5μm	TE-X(μm)	–	6.22	5.51	4.75
	TE-Y(μm)	–	3.56	4.03	3.82
	Coupling Efficiency%	–	65.2	59.3	69.2
	TM-X(μm)	–	6.75	4.83	4.01
	TM-Y(μm)	–	3.47	3.15	3.71
	Coupling Efficiency%	–	65.4	65.1	67
2μm	TE-X(μm)	6.27	5.18	5.15	4.71
	TE-Y(μm)	4.05	3.48	3.42	3.57
	Coupling Efficiency%	49.1	67.4	77.3	76.7
	TM-X(μm)	4.86	5.94	5.65	5.23
	TM-Y(μm)	2.95	3.73	3.20	3.67
	Coupling Efficiency%	58.0	67.9	71.1	72.1
2.5μm	TE-X(μm)	6.87	5.26	5.01	4.79
	TE-Y(μm)	3.61	3.47	3.65	3.52
	Coupling Efficiency%	58.9	70.2	75.9	80.2
	TM-X(μm)	7.17	5.81	5.14	4.86
	TM-Y(μm)	3.51	3.56	3.32	3.33
	Coupling Efficiency%	56.2	68.7	72.0	76.2
3μm	TE-X(μm)	6.99	5.69	5.04	5.61
	TE-Y(μm)	3.40	3.71	3.38	4.01
	Coupling Efficiency%	52.1	68.3	78.6	73.9
	TM-X(μm)	7.43	5.98	5.92	5.53
	TM-Y(μm)	3.31	3.36	3.35	3.72
	Coupling Efficiency%	57.4	72.9	73.4	78.8
3.5μm	TE-X(μm)	7.93	6.56	5.47	5.22
	TE-Y(μm)	3.56	3.46	3.64	3.70
	Coupling Efficiency%	55.6	66.2	75.1	71.2
	TM-X(μm)	8.51	6.39	5.62	5.59
	TM-Y(μm)	4.09	3.25	3.45	3.59
	Coupling Efficiency%	62.2	70.5	76.8	82.6

TABLE 2.1: Mode dimensions of a set of testing waveguides fabricated with different waveguide openings and ion exchange times and the calculated fibre to waveguide coupling efficiency.

Point Source PM fibre mode dimension			
TE-X(μm)	TE-Y(μm)	TM-X(μm)	TM-Y(μm)
3.76	3.40	4.26	3.59

TABLE 2.2: Mode dimension of the Point Source PM fibre.

measured waveguide loss in dB for a set of 2.5μm width of straight waveguides against different IE times. About 5 to 8dB difference between the two curves can be seen, which is mainly due to the fact that some of the losses were not considered in the calculations, such as excess coupling loss, including Fresnel loss, propagation loss and misalignment loss, while in the measured loss they were all included.

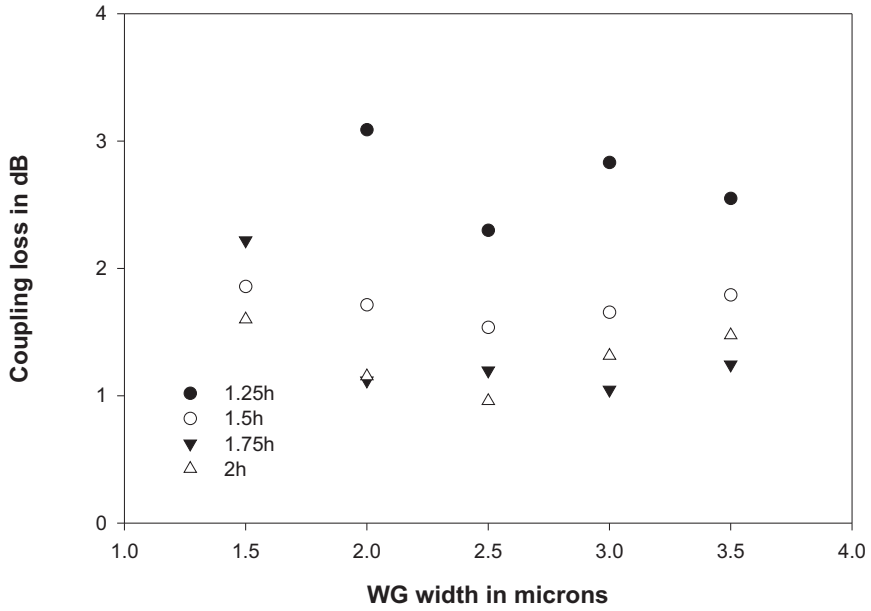

FIGURE 2.8: Coupling losses for different waveguide widths and IE times were calculated based on the measured fibre and waveguide mode profile (TE mode only).

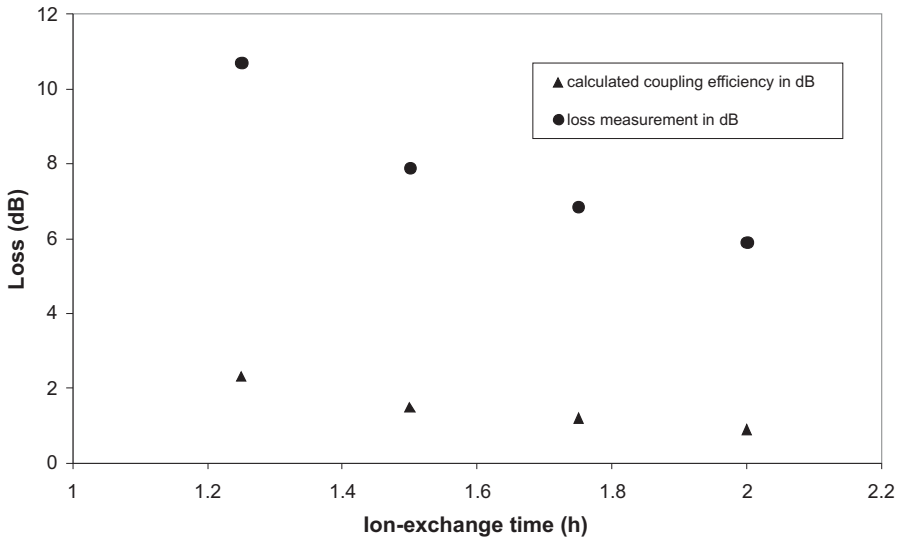

FIGURE 2.9: Direct comparison of the calculated coupling loss in dB and the measured waveguide loss for a set of 2.5 μm width waveguides with different IE times.

From the above calculation, the optimised parameters, based on the best coupling efficiency for the waveguide design, are 2.5μm for the waveguide opening and 2 hours for the IE process.

2.4 Optimisation of the isolation layer

2.4.1 Introduction

The isolation layer, which is used to isolate the waveguides from their surroundings except where the sensing patches are situated, has been studied and optimised in terms of the deposition process and annealing process.

Vacuum-deposited Teflon FEP has proved a useful isolation material for experimental devices (56), due to its low refractive index, low porosity and ease of patterning, but it has not, so far, proved acceptable for use in sensors which are to be handled repeatedly, as it is easily damaged. Development of these devices for prolonged use in an instrument requires optimisation of hard dielectric materials, such as sputtered silica films, as robust isolation layers. However, sputtered silica tends to exhibit higher optical attenuation than vacuum-evaporated Teflon, unless it is annealed in an oxygen-bearing atmosphere at high temperature. As the silica in these devices is to be deposited on substrates containing ion-exchanged surface waveguides, it is important to determine an acceptable deposition process without high-temperature annealing which would degrade the underlying waveguides by thermal diffusion.

This section addresses the research results and the comparison of using two methods of producing the silica isolation layer, the PECVD method and using the RF sputtering machine.

2.4.2 Silica layer deposited by PECVD

A trial of depositing a silica layer by the PECVD (STS Mesc Multiplex Chemical Vapour Deposition V1 Tool) method was carried out on the preliminary test waveguide samples, which were realised by potassium ion-exchange in BK7 glass, with widths between 1.5 and 3.5 microns for diffusion times of 1.75 hours in molten KNO_3 at 400 °C. The size of the BK7 glass substrates were 50mm by 50mm. The final length of the waveguide sample is 35mm. The 1 μm silica layer was deposited under a chamber pressure of 1 Torr, 156 sccm 5% SiH_4 in N_2 and 710 sccm N_2O, at the power of 19 W and temperature of 300 °C, for 20 minutes.

As a result, an additional loss of 7dB was measured for the 3μm width waveguide after adding the silica layer using the PECVD method. Figure 2.10 shows the waveguide loss before and after the silica layer was deposited using the PECVD method over the straight waveguides set, the waveguide widths were from 2μm to 3.5μm with steps of 0.5μm.

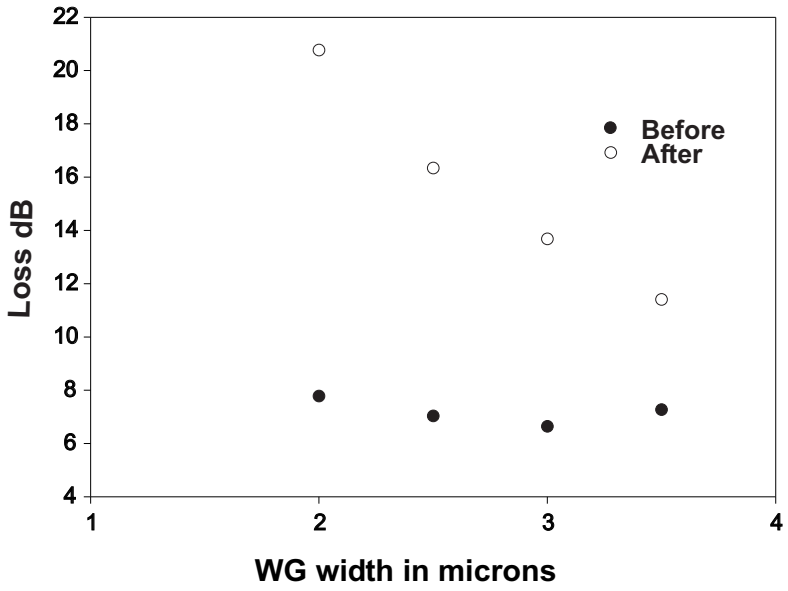

FIGURE 2.10: Waveguide loss measured before and after the silica layer was deposited on sample No 9 by the PECVD method. The IE time was 1.75 hours, the length of the sample is 35mm.

2.4.3 Silica layer deposited by RF sputtering

A test trial was then carried out using the RF sputtering machine (model: Plasmalab 400 RF, Oxford Instruments Plasma Technology). Note: due to the time constraints at the time, the RF sputtering was done on the 4-way waveguide under the same substrate and same fabrication parameters. The silica layer was deposited at the sputtering condition of 250 W in 10 mTorr argon, 1mTorr oxygen for 2.5 hours at 10 °C, followed by annealing in oxygen for 1 hour at 250 °C. Figure 2.11 shows the insertion loss for all four linear channels before and after annealing.

Annealing gives an 8dB improvement in transmission, and produces reduced porosity of the silica layer (13). The remainder of the attenuation is due to the 4-way division (6dB), propagation losses and fibre/guide coupling losses (6dB). The outcome of using the RF sputtering was better in comparison with using the PECVD method, since the length

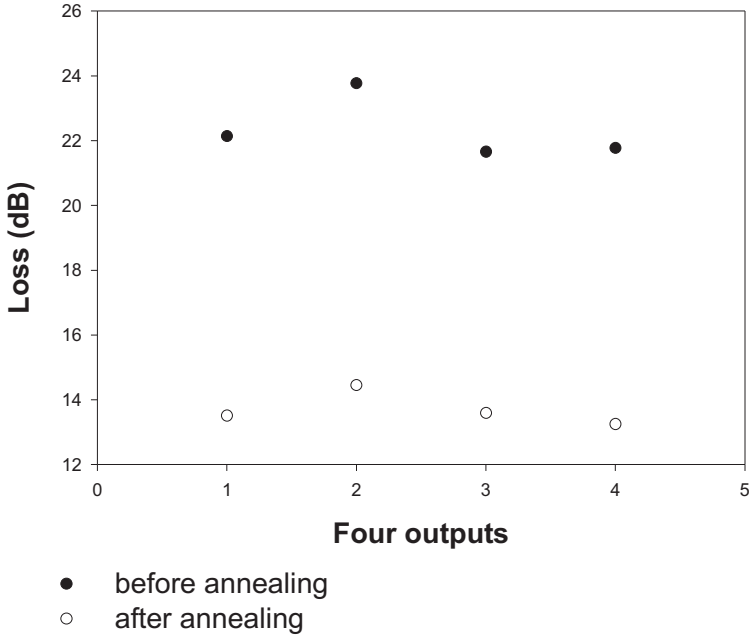

FIGURE 2.11: Insertion loss measured before and after 1 hour annealing at 250 °C. Sample No.11.

which was covered by the silica film was 43mm and the measurement was also carried out on a 4-way splitter, while the length of the sample coated with silica by PECVD was 35mm, and the measurements were carried out on a set of straight waveguides. The loss measurement results were 0.4 dB.mm^{-1} and 0.17 dB.mm^{-1} for PECVD method and RF sputtering respectively. Therefore, the RF sputtering silica method was selected for the final fabrication process.

2.5 Predictions on sensitivity enhancement by coating with a high-index film

This section will explore the possibility of enhancement of the sensitivity of the sensor chip. The integrated optical fluorescence multi-sensor described in this thesis exploits the fluorescence immunoassay in an evanescent field of optical channel waveguides. Its mechanism is based on the fact that the evanescent field will interact with organic pollutants. One of the major objectives of the research work in the past, on this type of sensor, has been to improve its sensitivity. Stewart and Culshaw achieved a theoretical

enhancement in the sensitivity of an evanescent wave methane sensor by adding a high index overlay, using modeling, as described in their paper (57). They theoretically predicted an enhancement of greater than an order of magnitude for their sensor design. Quigley and Wilkinson have put these theories into practice (1).

Figure 2.12 shows the theoretically predicted enhancement factors against various thick-

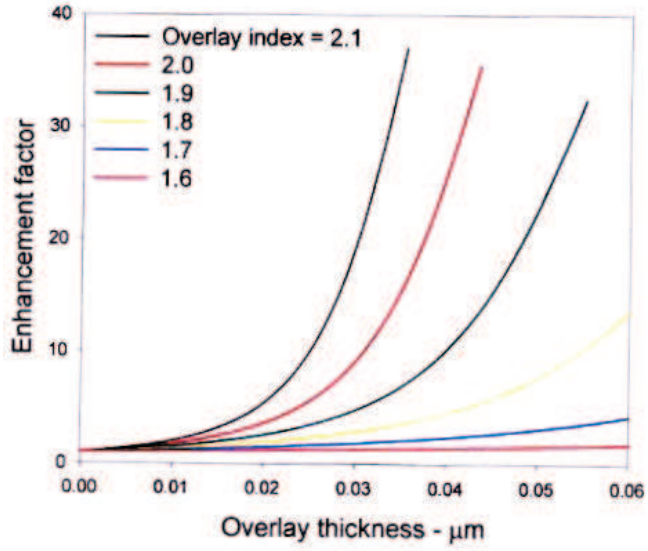

FIGURE 2.12: Enhancement factor against various thickness and refractive indices of the overlay of high-index films from (1).

ness and refractive indices of the overlay of high-index films. The intensity enhancement in the evanescent field is mainly due to the thin high-index film overlays which modify the distribution of light in the optical waveguide. Consequently more power is carried in the superstrate evanescent field as shown in Figure 2.13.

The fluorescence sensing experiments aimed at testing the high index films were performed on sensor chips which were fabricated and capable of measuring fluorescence at 2-4 discrete sensing positions simultaneously (51). The chip has a channel waveguide with a structure of one split only. The loss of the waveguide was about 5-6dB.cm^{-1} (targeted at 2.5dB.cm^{-1}), and discrete sensing patches were located on one of its branches. Patches were coated with or without high index film Ta_2O_5. The measurement of concentrations of simazine and isoproturon in water were carried out and sensitivities as low as 0.03ppb were reported. According to the outcome of the experiments, the highest sensitivity came from a sensing patch which was not coated with the Ta_2O_5 film. It was found, after investigation into the use of high index films on these fluorescence

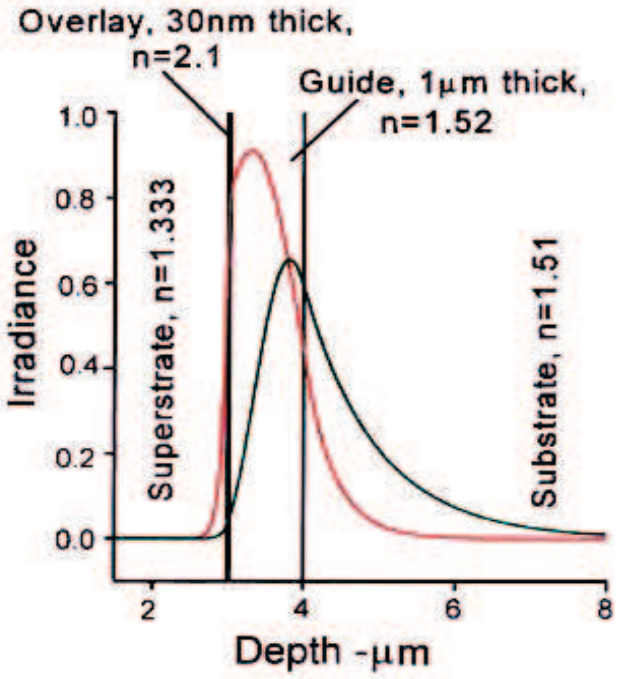

FIGURE 2.13: The field in green is before adding the high-index film. The field in red is after adding the high-index overlay from (1).

sensors, that outcomes of these sensors are not limited by low intensity of illumination or excitation, but by the photodegradation of the fluorophores (51).

It was pointed out that applying the high index films onto the surface of a low NA waveguide to increase the interaction of the guided mode with the superstrate medium, is more favourable to refractometry. However, it is also applicable to large array sensors, in which the input power may be divided between more waveguides. In this case the use of high index films would permit low power light sources to be used without compromising sensitivity (57; 1; 51). Preliminary work by Harris (52) showed that a 20nm film of Ta_2O_5 on waveguides similar to those described in this thesis enhanced fluorescence signal strength by a factor of 6 for a fluorescence-based immunoassay. Work by the present author on a refractometer (13) confirmed this behaviour and showed that much higher enhancements, due to increased surface intensity, could be achieved with thicker Ta_2O_5 films. In that work, a set of identical chips coated with different thicknesses of Ta_2O_5 films, were measured of their response to liquid analyte index by passing aqueous sucrose solutions over the sensor surface. The use of these films is shown to increase sensitivity by a factor of up to eighty with a film thickness of 45nm.

The experiments demonstrated that adding a thin Ta_2O_5 film over the window of the refractometer substantially increases the sensitivity of the device to changes in analyte index, with the sensitivity enhancement increasing rapidly with Ta_2O_5 film thickness. It also shows that the sensitivity increases with increasing analyte index. Both these effects are due to enhancement of the proportion of modal power travelling in the analyte (1). For the fluorescence-based immunoassay, the fluorescence intensity is proportional to the surface intensity. The above work also showed that the window attenuation is insignificant for the device without Ta_2O_5 coating and for that with a 15 nm Ta_2O_5 film. The attenuation becomes significant for a film thickness of 30nm and becomes catastrophic for films over 45nm thick, with attenuation of over 30dB. Annealing the device reduced the attenuation from 30dB to 14dB, due to reducing the optical absorption in the Ta_2O_5 film (13).

In this research, a four-way split structure is adopted for the sensor chip in order to accommodate more sensor patches on a chip. So, the power in the waveguide will be further reduced by 6dB at least, due to the four-way split, plus other losses in the waveguide. Therefore, adding high index films onto the surface of sensor chips, as one of options to enhance the sensitivity, is also considered as a part of this study.

2.6 Fibre pigtailing

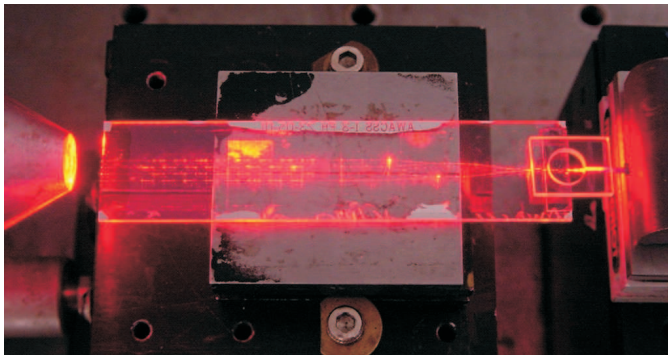

FIGURE 2.14: Fibre-pigtail setup.

The reason behind applying fibre pigtailing to the sensor chip is the requirement for the prototype device to be portable, plug-and-playable, user-friendly, and fully automated. Furthermore, the fibre pigtailing also contributes towards signal stability and reliability. Since submicron alignment is one of the features of fibre pigtailing, the actual fibre to

waveguide bonding process will become very difficult. For this reason, a multi-stage bonding process was used in order to achieve near-lossless and robust bonding between the fibre and waveguide.

Figure 2.14 shows a pigtailed chip, where the fibre is bonded to the chip at the right end in the photograph.

The support piece is bonded on top of the substrate near the input end. The fibre tip is pre-bonded to the input of the waveguide using UV curing epoxy (Lensbond Type VTC-2, P-92 and SK-9 purchased from Electromotif). The fibre is finally bonded to the waveguide for additional robustness and the fibre is then bonded to the support piece. Further improvement has been achieved by pigtailing fibre in a ferrule, which is considerably more robust and stable compared to pigtailing the bare fibre. Excess loss due to the fibre pigtailing is 0.1dB.

2.7 Estimation of the power budget

In order to select the most suitable detection system for this study, it is necessary to know the power distribution along the optical chip and the amount of fluorescence power reaching the receiving end of the detection system. This can be achieved by calculating the surface intensity over the sensing region using the BPM method followed by analysis of absorption and emission of fluorescence molecules.

The input parameters in the calculation were based on the fabrication condition adopted for the integrated optical chip.

A set of fabrication parameters has been established, as described in the previous section, which were optimised for the best coupling efficiency of the modal intensity between fibre and waveguide. In this section, a detailed study on 2D index profile, waveguide surface intensity and quantified emitted fluorescence are presented.

2.7.1 2D index profile model

Having a precise refractive index profile of a waveguide is essential for design, optimisation and fabrication of the waveguides as well as for analysing their properties.

There have been numerous studies on the "exhausted source" diffused waveguides, such as channel waveguides formed by diffusing transition metals into $LiNbO_3$ or $LiTaO_3$ (9; 58; 59), using the effective index method(9) and Fick's equation of diffusion theory (58), or a numerical approach (59). But the results achieved by these studies were more or less the same in terms of 2-D index profile as for diffusion from a metal strip. A common feature of these results is that the index profile follows a Gaussian distribution in the diffusion depth, and has the shape of an error function (erf) in the lateral direction.

There are also studies on "non-exhausted source" diffusing waveguides, such as potassium or silver ion exchange in glass (60; 61; 62; 63; 64; 65). The results of the index profile differed from each other among those studies. For the potassium ion exchange channel waveguide in a 2-D profile, as an example, the complementary error function of index profile in the diffusion depth has been recognised by the majority (60; 61; 62; 65), However, in a lateral direction the Gaussian (61) or erf (64) profiles are widely used; either of which only suits narrow waveguide openings, and cannot be applied to wider waveguide openings, e.g. for the tapered waveguide in this case.

Why is there a difference between exhausted and non-exhausted source diffusion? The key difference is the boundary condition on the interface, the ion source, and the substrate. For the exhausted source, the source concentration will gradually decay during the diffusion process; therefore the index profile in the substrate has a continuous and smooth pattern which can be described by a mathematical function such as a Gaussian distribution or error function. On the other hand, in the non-exhausted source diffusion case, the ion concentration at the surface will remain constant during the diffusion process. This constant ion source will result in a non-smooth or non-differentiable point in the index profile in the area under the edge of the mask. No simple analytical mathematical expression exists for the resulting index profile.

So far, the profile parameters of non-exhausted ion exchanged planar or channel waveguides are normally determined either by mode-index measurements (60; 61), using the prism coupling method (66), or a numerical approach (62; 63; 64).

In section 2.2.2, a constant index profile was used in order to simplify the calculation in a 2D simulation process using BPM to optimise the tapered waveguide parameters. In this section, a 2D index profile is derived which reflects the real IE waveguide in this study, and thus enables the precise calculation of the optical intensity distribution

along the tapered waveguide. In the next section, a three dimensional analysis will be introduced in order to describe the flow of intensity.

For channel guides, it has been found that, although the surface-index change Δn of channel waveguides is almost the same as that of the corresponding planar guides, the diffusion depth is different and depends on the mask width and the extent of the side diffusion or lateral diffusion under the mask, which is relatively independent of the mask width (61). According to H.F Taylor (62), the ratio of the extent of lateral diffusion to the depth diffusion, defined at the $1/e$ concentration point, is of order of 0.43 for the case where the waveguide width is greater than the diffusion depth, and an exponential function is a close fit to the lateral diffusion profile under the mask.

The optimum condition for the fabrication of a potassium ion-exchanged channel waveguide in a BK7 substrate at a wavelength of 635 nm, was found to correspond to an effective diffusion depth, d, of approximately 3 μm with a waveguide width between 2.5μm to 3μm. The effective depth was plotted against the square root of the diffusion time, t, (t=2 hours in this case) and an effective diffusion coefficient D_e =1.42x10^{-15} m^2.s^{-1} (60) using the relation d=$\sqrt{D_e t}$.

The non-exhausted source induced 2-D index profile in a tapered waveguide can be modelled section by section along the lateral direction of the taper as below:

$$n(x,y) = n_s + \Delta n f(y) f(x) \tag{2.3}$$

where

$$f(y) = erfc(y/d_y)$$

$$f(x) = exp[-(x-w(z)/2)/d_x], if\ x \geq w(z)/2$$

$$f(x) = exp[(x+w(z)/2)/d_x], if\ x \leq -w(z)/2$$

$$f(x) = 1, \text{ if } -w(z)/2 \leq x \leq w(z)/2$$

In which, x is in the lateral direction; y is the diffusion depth; w is the width of the mask; n_s=1.5151(substrate index), Δn=0.0094 (the peak change in refractive index),

dy=3μm(diffusion depth), dx=0.43dy. Figure 2.15 shows the waveguide surface index profile of the 30μm width section of taper, modelled in this way.

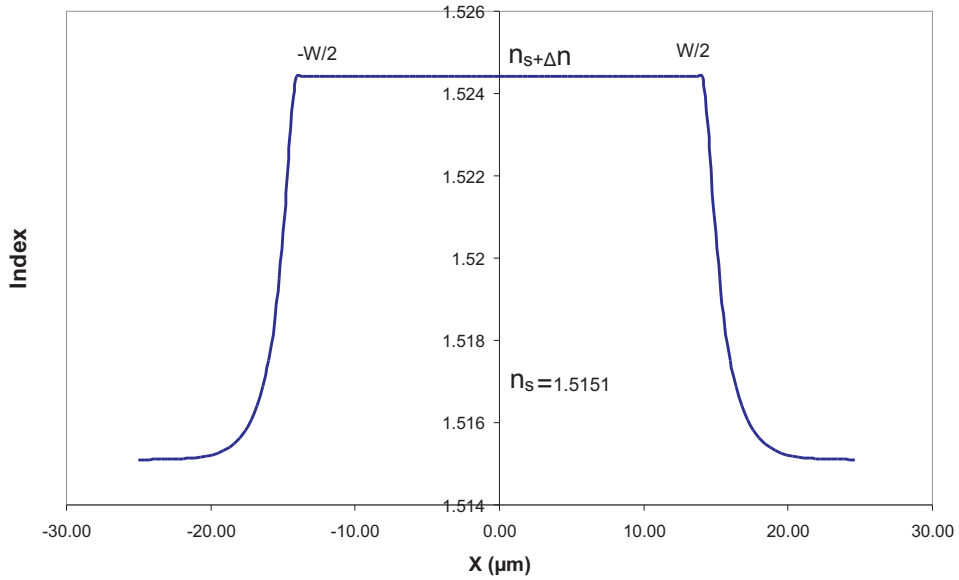

FIGURE 2.15: The index profile of a 30μm taper at the waveguide surface

2.7.2 Waveguide surface intensity

In section 2.2.2, a set of tapered waveguide parameters was optimised by using 2D BPM simulation. In this section, the OlympIOs 3D BPM simulation is used in order to obtain the waveguide surface intensity, determined from the field distribution at the cross-section of the waveguide.

The 3D simulation was carried out for tapered waveguides, tapering to a width of both 30μm and 60μm, using OlympIOs BPM in conjunction with the 2D index profile, equation 2.3, and assuming an input power of $1mW$. As an example, Figure 2.16 shows the start field and the end field of 60μm width tapered waveguides.

Intensity can be obtained from the square of the field strength:

$$\begin{aligned} I_{waveguide} &= \sqrt{\frac{\mu}{\epsilon}} \times H^2 = \sqrt{\frac{\mu_0}{\epsilon_0}} \frac{1}{n_{eff}} \times H^2 \\ &= \frac{377}{n_{eff}} \times H^2 \end{aligned} \tag{2.4}$$

In which the mode index $n_{eff} \cong 1.52$.

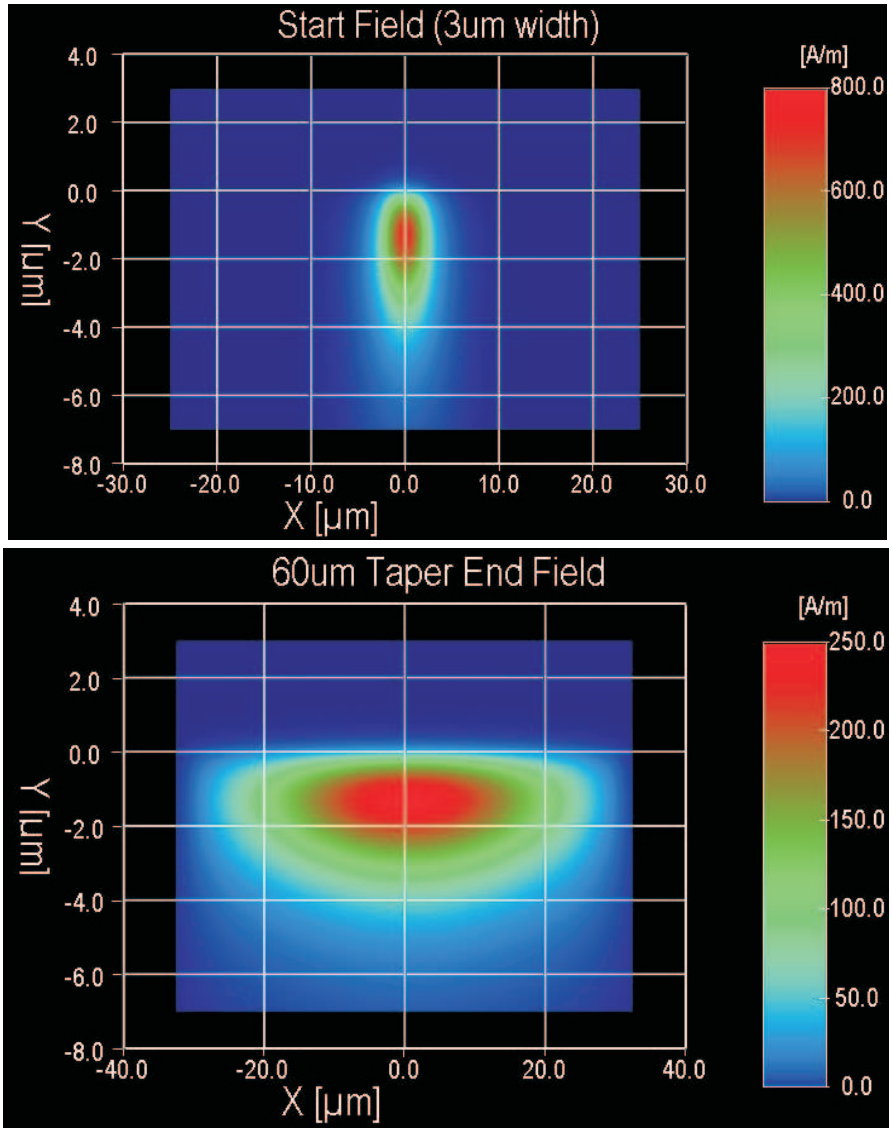

FIGURE 2.16: The start field and the end field of 60μm taper waveguides

Figure 2.17 shows the maximum intensity of the start waveguide of 3μm and the end of 30μm and 60μm taper waveguides in the diffusion -y direction, in $W.\text{mm}^{-2}$, obtained from the model. The maximum intensity means the mode intensity in the depth direction through the centre of the waveguide.

Figure 2.18 shows an expanded view of the intensity distribution at the waveguide/analyte interface, which indicates the waveguide surface intensity.

Figure 2.19 shows the surface intensity of the start of the waveguide and the end of 30μm and 60μm taper waveguides in the lateral direction (across the surface of the

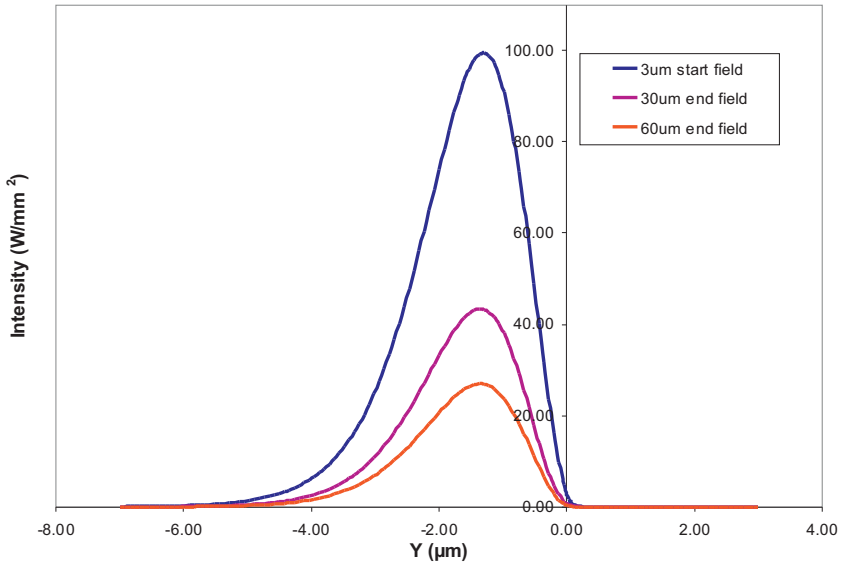

FIGURE 2.17: Maximum intensities of the start (3μm) and the end of 30μm and 60μm taper waveguides in the diffusion -y direction, which are 100 $W.mm^{-2}$, 43 $W.mm^{-2}$and 27 $W.mm^{-2}$ respectively

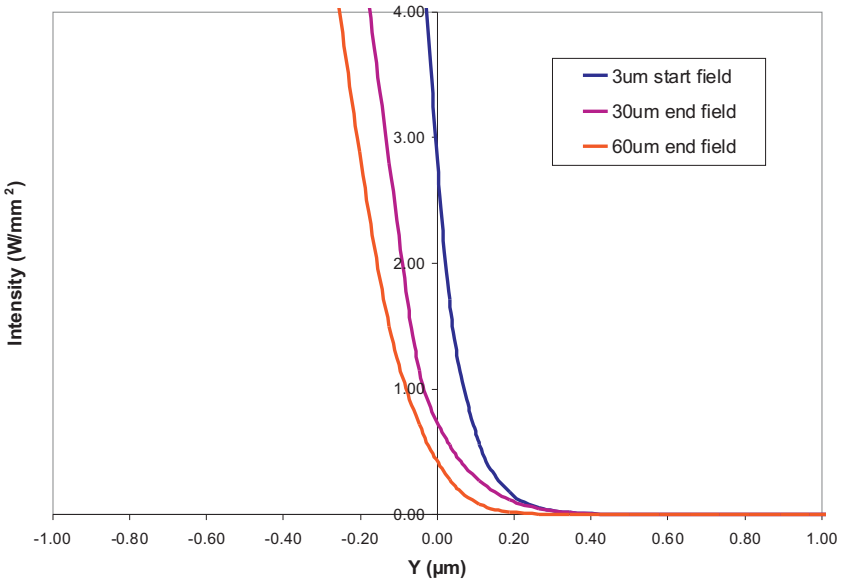

FIGURE 2.18: An expansion of the interface shown in Figure 2.17

waveguide), with an input power of $1mW$. The predicted emitted fluorescence intensity is also plotted on the same chart (as explained in the section 2.7.4 below).

Therefore the peak surface intensities for $1mW$ propagating in the waveguide, for 30μm and 60μm taper waveguides, are 0.804 $W.mm^{-2}$ and 0.502 $W.mm^{-2}$ respectively.

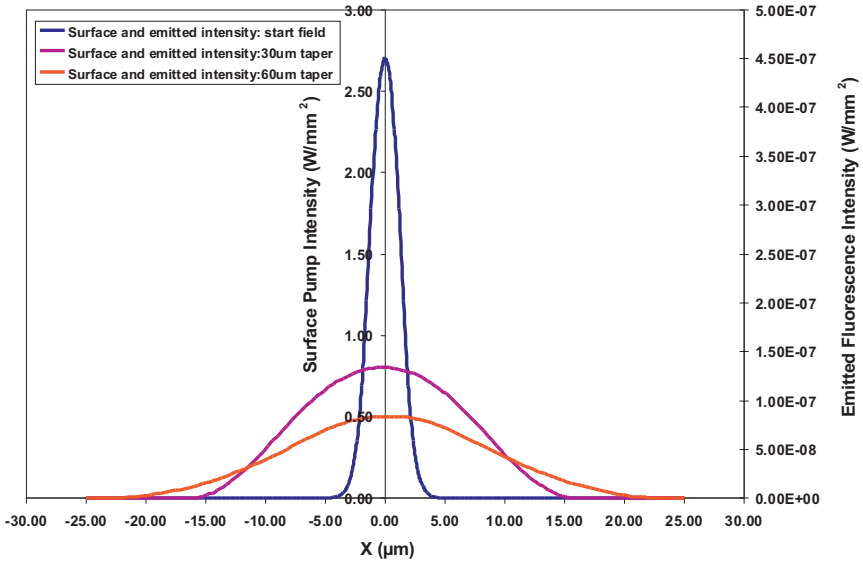

FIGURE 2.19: Surface intensity of the start (3μm) and the end of 30μm and 60μm taper waveguides in the lateral direction and emitted fluorescence intensity, detail of the latter is given in the section 2.7.4

2.7.3 Estimation of detection limit for the system

This section will study the possible detection limit for the detection system, in theory, based on the immunoassay characteristics, and an equivalent detection limit with dye solutions for the system is also predicted.

In an immunoassay with a binding inhibition format, analyte specific antibodies which are not occupied by analyte are quantified. In this type of assay the number of binding sites supplied by the antibodies should not, by far, exceed the number of target analyte molecules. This results in an upper limit of about 10 nmol.L^{-1} (<1 mg.L^{-1} IgG) for the analyte specific antibody (67). For binding, the analyte/antibody mixture has to be brought into contact with the sensor surface. By using of a flow injection system the diffusion layer thickness can be minimised and the mass transport to the surface can be optimised. Under practical conditions a diffusion layer thickness, d, of 10^{-5}m may be reached (67). For a given antibody concentration, c_{ab}, the maximum binding rate, Γ_{max}, can be derived from Fick's first law assuming a surface concentration of free antibody of zero and taking into account the diffusion coefficient for IgG (D_{ab}=6x$10^{-11} m^2.s^{-1}$):

$$\Gamma_{max} = \mathrm{D}_{ab}\frac{c_{ab}}{d}$$

A maximum binding rate of 6 pmol.m^{-2}.s^{-1} can be extimated. The corresponding maximum change in surface mass coverage is about 4.5 μg.m^{-2}.s^{-1} or 1% of a protein monolayer per second (assuing an IgG monolayer coverage of about 5 mg.m^{-2} (68)). In practice, limited convection may lower the binding rate by up to one order of magnitude. Acceptable measurement times will dictate incubation times below 1000s but, preferably, times of approximately 100s are targeted. Therefore, a maximum surface coverage of 0.6 nmol.m^{-2} can be expected, in binding inhibition assay formats this corresponds to the maximum assay response (blank measurement), which will decrease with increasing analyte concentration. So, the detection system should resolve this value to 1 % or less (i.e. 6 pmol.m^{-2}) (67).

A simple estimation for the performance of a sensor device can be obtained by exposing it to a dye solution. The fluorophores' excitation will take place only within the penetration depth of the evanescent field (a few 100nm), corresponding to a volume per square metre of about 5 x10^{-7}m^3.m^{-2} (0.5 ml.m^{-2}). A 1.2 x10^{-8}M fluorophore solution will bring the same number of fluorophores into the excited volume as a surface concentration of 6 pmol.m^{-2}. Therefore, a possible detection limit for the optical detection system with dye solution with concentrations down to 10^{-8}M is desirable.

2.7.4 Emission by dye molecules

A crucial issue in the power budget analysis is estimating how much fluorescence will be emitted by dye molecules on the sensor surface with a certain surface pump light intensity.

In this section, the emission in a situation of the minimum surface coverage necessary to detect of 6pmol.m^{-2} is considered, in which the number of antibody molecules per m^2 is equal to:

$$6\text{pmol.m}^{-2} \text{ x } 6.02 \text{ x } 10^{23} \text{ mol}^{-1}\text{(Avogadro's Number)} = 3.61 \text{ x } 10^{12} \text{ antibodies.m}^{-2}$$

Since about 2 to 6 Cy5.5 molecules will bind to each antibody (67), the worst case of the density of Cy 5.5 molecules in the same surface coverage is 7.22 x10^{12} (Cy5.5molecules).m^{-2}.

The fluorescence emission intensity $I_{emitted}$ is given by:

$$I_{emitted} = D \times \eta \times (\lambda_p/\lambda_e) \times \sigma_a \times I_s \tag{2.5}$$

In which D is the molecule surface density, η is the quantum efficiency of Cy 5.5 which is 0.28, λ_p is the pump wavelength (638nm) and λ_e is the emission wavelength of Cy 5.5 (700nm), σ_a is the absorption cross-section of Cy5.5, which is 3.6 x10^{-20}m^2 (69) and I_s is the surface intensity.

Thus, for the minimum dye molecule density which must be detected, the emission intensity is given by $I_{emitted} = 6.6 \times 10^{-8} \times I_s$

As an example, for a 30μm taper waveguide with $1mW$ input power, the $I_{emitted}$ at the peak surface intensity is 53 nW.mm^{-2}.

In Figure 2.19, the axis on the right side corresponds to the emitted fluorescence intensity. The total emitted fluorescence $P_{emitted}$ from the area of a 30μm taper waveguide (30μm x 1.5mm, the length of the sensor patch) is

$$P_{emitted} = \int_{-\infty}^{\infty} I_{emitted} dx \times 1.5(mm) = 1.4nW \tag{2.6}$$

The total emitted fluorescence from the area of a 60 μm taper waveguide is $1.1nW$.

For the minimum surface density of fluorescence molecules to be detected (7.22 x10^{12} Cy5.5-molecules.m^{-2}), the total emitted fluorescence power is predicted to be $1.4nW$ for the 30μm taper waveguide area of 30μm x 1.5mm per mW of pump power in the waveguide. And for the 60μm taper waveguide with the area of 60μm x 1.5mm, the total emitted fluorescence power is predicted to be $1.1nW$ under the same pump power in the waveguide. This established a design parameter for the next chapter which describes the instrumentation in more detail.

2.8 The first generation sensor chip fabrication process

The results of the design procedure are summarised here. The multisensor chip was fabricated by potassium ion-exchange in BK7. Since the BK7 glass has good optical quality and exhibits low fluorescence, and the process produces low loss waveguides,

uses low cost materials and fabrication procedures, and had already been optimised in our laboratories for low loss coupling from optical fibres resulting in minimisation of scattered light in the substrate.

The overall chip dimensions were 67mm x 15mm, constrained in length by the exposure area of the mask aligner and in width by ease of handling. The waveguide circuit was defined by opening tracks 3μm (for a signal mode waveguide at 633nm) wide in this film using conventional photolithography, following the layout shown in Figure 2.1. Ion exchange was carried out by immersing the masked substrates in KNO_3 at 400 °C for 2 hours to produce single mode channel waveguides with good coupling to optical fibre. Parabolic taper waveguides widening to 30μm and 60μm were introduced into each waveguide branch after the Y-junction splitters in order to reduce the optical power density at the waveguide surface, and hence to reduce the rate of fluorophore photobleaching. The purpose of broadening the waveguides was to maintain the emitted fluorescence power while reducing the pump intensity incident upon each dye molecule and thereby reducing photobleaching and allowing longer acquisition time and hence improved signal to noise ratio.

A silica layer thickness of 1 micron ensures that the intensity at the surface of the isolation layer is much less than 1% of the intensity within the window, effectively isolating the chip from the analyte outside the window.

Deposition of the Ta_2O_5 film was used for some devices to explore its effect upon sensor system performance. In order to enhance the surface intensity in the sensing windows, a 25nm thick film of Ta_2O_5 was deposited over the entire surface of the chip by RF sputtering in an atmosphere of 1 : 9 oxygen : argon at a total pressure of 11mTorr, which resulted in optimised films with low loss as showed in Figure 2.21. A factor of 10 enhancement of the surface intensity is expected with the 25 nm Ta_2O_5 film, which would lead approximately to a factor of 10 enhancement in peak signal strength. A polarisation-maintaining (PM) fibre pigtail with a PM connector was permanently bonded to the input end of the sensor chip with UV-curing epoxy.

Figure 2.20 shows a photograph of one of the sensor chips.

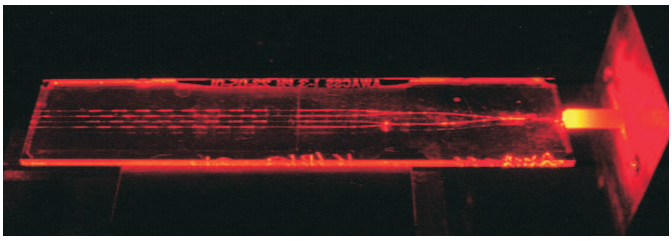

FIGURE 2.20: Photograph of the sensor chip.

2.9 Further improvements on the new generation sensor chip fabrication

Based on the outcome of the fabrication of the first generation of sensor chips and the calculation result of overlap integrals, the new waveguide diffusion mask width has been changed from 3μm to 2.5μm, in order to improve the fibre/device coupling efficiency, as mentioned in early of this chapter. Further, the chip is now entirely covered by the silica isolation layer apart from the sensing windows themselves, in order to prevent the waveguide from being disturbed by anything dropped on the sensor surface. In the previous case, only 50% of the sensor area was covered by the silica isolation layer, because the silica layer used was very lossy (13).

The following improvements in the fabrication process have been implemented: the thickness of the new chip substrate was reduced from 1mm to 800μm, which also reduced the substrate absorption and scattering, and hence improved fluorescence collection; the silica layer was sputtered with an oxygen partial pressure of 20 mTorr, rather than 10 mTorr argon (section 2.4.3), during the deposition; excess loss due to the silica isolation layer was reduced to ~1dB. Tantalum pentoxide films of 25nm thickness have been deposited on one of the new sensor surfaces to increase signal strength, the sputtering process has been improved by using a rotating table and adopting a chamber temperature of 250 °C in order to improve film uniformity, which also resulted in negligible excess loss. The loss measurement was shown in Figure 2.21. The fibre in a ferrule has been introduced for fibre pigtailing, which is considerably more robust and stable compared to pigtailing the bare fibre. Excess loss due to the fibre pigtailing is now less than 0.1dB. Figure 2.21 shows the loss measurement for the same new chip in different fabrication stages, in which the 6dB loss due to the 4way split is not included. The rest of the fabrication process is the same as in the last section.

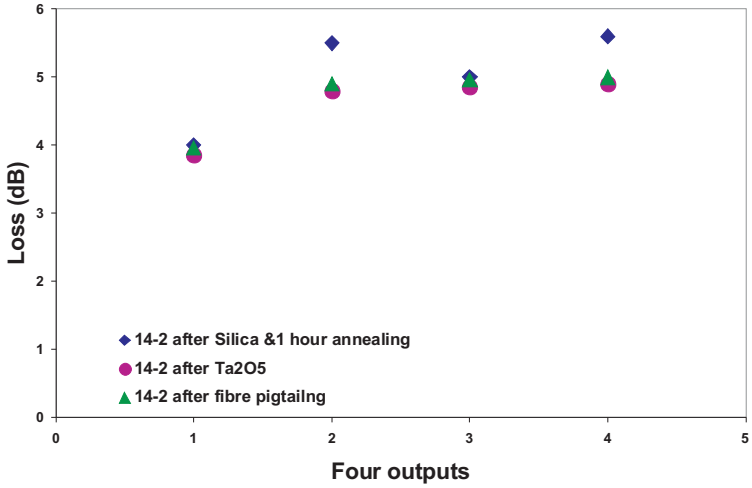

FIGURE 2.21: Loss measurement of the new generation sensor chip.

2.10 Conclusion

The optical waveguide circuit has been designed using OlympIOs software to ensure low-loss and adiabatic tapering. Near-field modal intensity profiles have been measured and compared with those of the selected polarisation-maintaining fibre; coupling losses were predicted using overlap integrals. Waveguide losses and fibre coupling losses have been measured directly and an optimised fabrication process has been selected for the sensor chips.

The first generation sensor chips have been fabricated and further optimised by achieving low-loss silica isolation layers in a newly-commissioned RF sputtering machine. Tantalum pentoxide films of 25nm thickness have been deposited on the sensor surface to increase signal strength with negligible excess loss.

A detailed study has been carried out to estimate the power budget over the waveguide region and to derive the 2D-index profile theoretically. A precise model, which describes the characteristics of the devices, has been established after a thorough study process of simulation and optimisation; this will contribute greatly to the future devices' design and fabrication.

New generation sensor chips were realised based on the outcome of the calculation and optimisation of the previous fabrication process, in terms of low loss and high signal strength.

The minimum fluorescence output power to be detected has been estimated, allowing the design of suitable collection optics and detection electronics in the next chapter.

Chapter 3

Multi-Sensor System I: Fibre collection and photodiode detection system

3.1 Introduction

The integrated optical fluorescence multi-sensor instrument, described in this thesis, is based on evanescent field technology. Laser light is coupled into an optical transducer and guided down to the multi-sensing area, which contains 32 patches in this case. The transducer surface is chemically modified in spatially distinct loci with analyte derivatives. Analyte-specific antibodies are labelled with a fluorescent marker which, upon binding to the transducer surface, are excited in the evanescent field. The emitted light is then collected for detection with 32 polymer fibres. The design allows for the simultaneous measurement of multi-analyte spots.

Optics, electronics and fluidics are three major parts of the instrument in terms of hardware requirements for the multi-sensor system. The development of miniaturised fluidics for the consumption of solutions, the provision of a sample handling system and the setting up of a detection system were the next major tasks after the design and realisation of the integrated optics. The microfluidic circuit was designed and fabricated by the former Central Research Laboratory (CRL) in London. This microfluidic circuit was

complementary to the sensor array and enabled the test sample to be presented to all 32 test spots, and allowed the access to the input and output ports of the fluidic circuits. It had been agreed among the research partners to use photodiodes in the instrument rather than a CCD array. Therefore the photodiode-based detection schemes, which consist of the photodiodes with integral amplifiers, an amplification and prefiltering stage, were experimentally evaluated for cost, noise, stability and detection limit. This chapter addresses various aspects of the instrumentation of the sensing system including a preliminary test of the photodetector/ amplifier, microfluidic and electronic components, optical component selection, testing, the basic concept of signal filtering and processing, the estimation of the optical power within the sensor device, the detection system, and the system operation.

3.2 System overview and operation

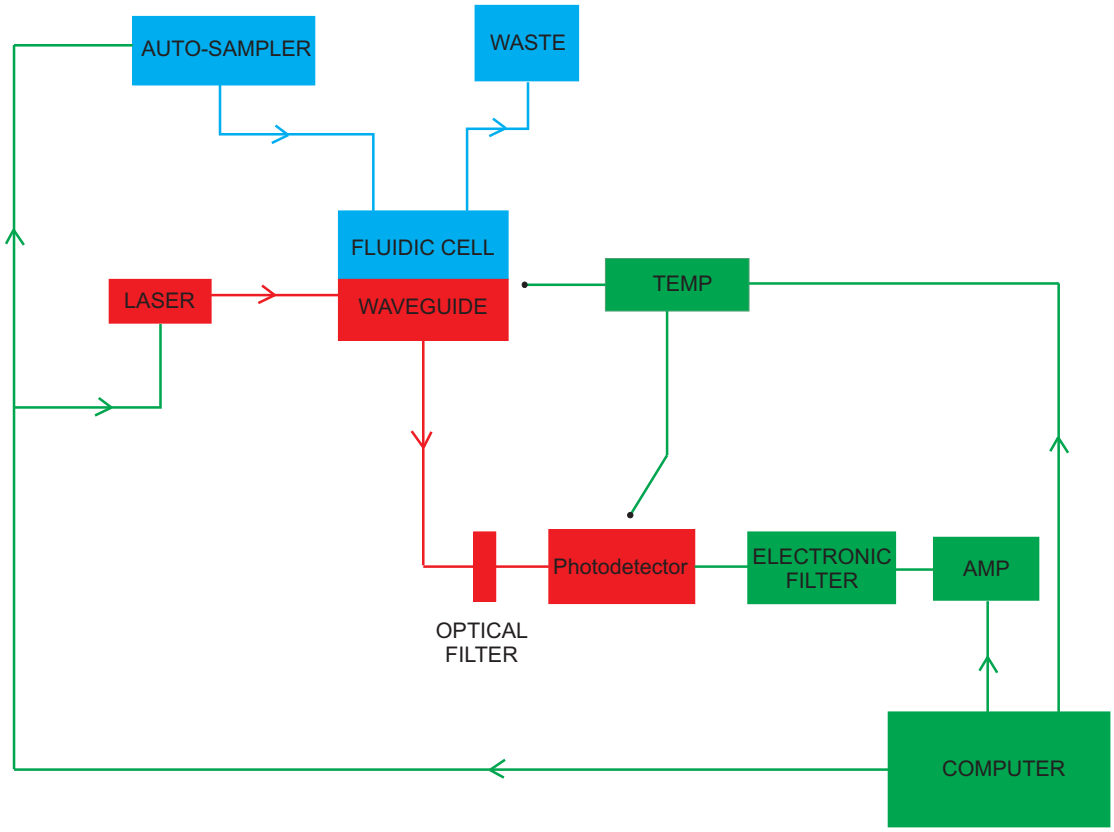

FIGURE 3.1: The flowchart of the multi-sensor system

Figure 3.1 is the flowchart for the multi-sensor system; it illustrates the three major parts of the instrument. The waveguide, laser and detector are the optical part, which forms

the heart of the instrument. This part is comprised of integrated optical fluoro-sensor arrays with potential for multi-analyte operation combined with pigtailed laser diodes for stable and precise control of fluorescence excitation. The fluidics part consists of an auto-sampler and the microstructured fluidic cell, which delivers fluid to the sensing system with small sample and reagent volume. The rest are electronics components including a photodetector (PD), amplifiers, temperature sensors and an electronic filter, which carries out measurements and data processing. All these three major parts are controlled by a computer.

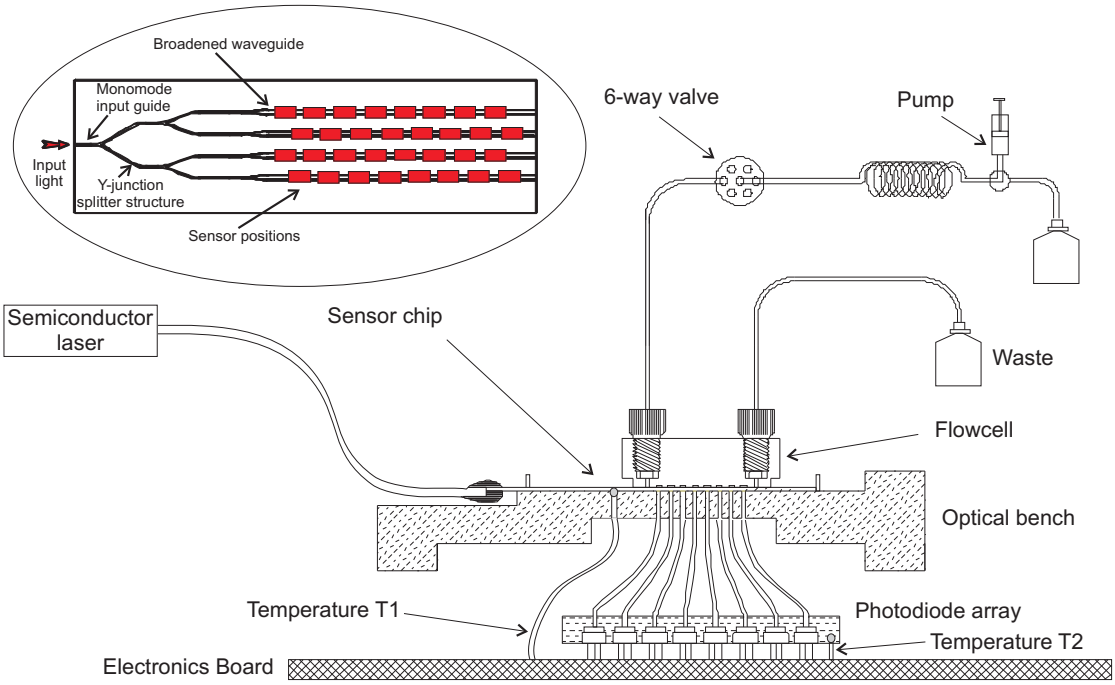

FIGURE 3.2: Experimental set up.

The complete apparatus for immunoassay measurements is shown in Figure 3.2. Light from a semiconductor laser is coupled into the input waveguide of the sensor chip, this input power is divided equally into four parallel waveguides through three Y-junction splitters and, in the 32 exposed sensing regions, the evanescent field is able to interact with the analyte, forming spatially separated sensing spots. If a fluorophore is brought within a few 100nm of the sensing spot the evanescent field of the guided light will excite the fluorophore, resulting in fluorescence. The fluorescence is collected by an array of 1mm core diameter high numerical aperture polymer optical fibres located under the sensor chip, then filtered to remove stray pump light, and detected by a silicon photodiode.

A micro-flow-cell is affixed to the chip over the 32 patches to supply sequences of solutions to the sensor surface. The pumps and valves which supply the solutions, the laser, and the data acquisition system are controlled by a computer that is integrated in the housing. The fluorescence power from each sensing site, the laser power, the ambient temperature and the temperature at the sensor are recorded, and the data are logged and analysed on the computer.

3.3 Optical power estimation

It was established in Section 2.7.4 of the last chapter that, for the 30μm taper waveguide and 1mW of waveguide power, the total emitted fluorescence power from a sensing spot would be 1.4nW. In this section, the power collected by the photodiodes is discussed, which is vital to the instrumental design.

As mentioned previously, the emitted fluorescence will be collected by a 1mm core diameter, high numerical aperture, polymer optical fibre, that is located under the sensor patch since the flowcell is clamped on top of the sensor chip. The collected fluorescence is then filtered to remove stray pump light, and detected by a silicon photodiode.

As an example in Appendix A, the fluorescence collected from the 30μm taper waveguide patch is calculated, assuming that the dye emission is isotropic, and that the numerical aperture of the fibre is about 0.51$\pm$0.03 (and 0.48 was used for the calculation). The calculation shows that approximately 3.7% of the emission from a 1.5mm long 30μm wide fluorescent strip would be collected by the fibre beneath the patch.

By integration of the transmission spectrum of the optical filter with the emission spectrum of the dye Cy5.5, it is estimated that about 20% of the collected fluorescence passes through the filter.

Due to the thickness of the filter (a typical thickness of a suitable filter is about 3mm), and again the high numerical aperture of the fibre, only about 11% of the collected fluorescence light would reach the detector.

Combining the above figures, we can estimate that 0.08% of the emitted fluorescence will be collected and reach the silicon photodiode detector (details of optical component optimisation and selection will be given in section 3.4.3 of this chapter).

With 1mW power input to the waveguide, the collected fluorescence $P_{collected}$ from the 30 μm taper waveguide patch is:

$$P_{collected} = P_{emitted} \times 0.08\% = 1pW \tag{3.1}$$

With the same imput power to the waveguide, the total collected fluorescence from the 60 μm taper waveguide patch is 880 fW. Therefore, a detection system which can detect to its minimum power of 880 fW or less is adequate for this project.

3.4 Instrumentation

This section will study electronics, fluidics and the rest of the optical and electronics components in detail, plus the electronic signal filtering and processing.

3.4.1 Photodetector/amplifier selection and preliminary test

In theory, a worst case example is 1pW of fluorescence being collected by the detector under the condition of 1mW power input to the 30μm taper waveguide sensor spot, and 880fW for the 60 μm taper waveguide sensor spot under the same input power. Therefore, a detection system which can detect to its minimum power of 880fW or less is adequate for this study.

In practice, a peak fluorescence signal (blank measurement) of 5pW (without tantala high-index film) was achieved by Harris et al. in their waveguide immunofluorescence sensor for water pollution analysis (52). It can be estimated that, to achieve a 10 ng.L^{-1} detection limit, the reduction in fluorescence power from the blank value to 1% would have to be resolved. For example, 3σ=1% of 5pW is 50fW (σ is the standard deviation of the measurement). However, if a 10 times improvement can be achieved in signal by using tantala then the optical detection requirement can be increased to 500fW. This should be achievable by using the Centronics diode, which was chosen if the bandwidth was about 1 Hz, as the NEP is 150fW.(Hz)$^{-1/2}$, and 3 x NEP = 450fW. This leaves some room for degradation by CRL's amplifier. It is also worth mentioning that the former river analyser project (also called RIANA) aimed at achieving a detection limit of 100fW of fluorescent power incident on the photodetector. A practical detection limit of 120fW

was found in subsequent testing of the prototype unit which was considered acceptable (70). Based on these results, the same Centronics diode was selected as detector.

The purpose of this initial photodetector/amplifier hybrid selection test is to determine whether noise performance is acceptable without lock-in amplification. The experiment consisted of three steps.

The first step was to test the drift of the photodetector/amplifier in a constant temperature environment: a selected Centronic OSI 5 - IR - 100M/1k photodetector with an integrated amplifier was packaged with a Schott fluorescence emission filter and the input feed through for a 1mm core diameter polymer fibre was capped off with black tape. The aim of using a fluorescence emission filter is to filter out direct illumination from the pump source. The chip was powered by ±12V from batteries and placed in an environmental chamber (stabilised at 30±0.2 °C) for 12 hours, and the output was recorded. The sensitivity of the detector/amplifier is specified to be approximately 40 μV.pW^{-1} at a wavelength of 700nm. The output drifted by about 0.06mV over the full period, equating to about 1.5pW equivalent optical power.

The second step was to test the drift of the photodetector/amplifier in a variable temperature environment: the environmental chamber was set at temperatures between 25 °C and 50 °C at 5 °C intervals and allowed to settle for approximately 1hr at each temperature. The output voltage was recorded and the results plotted in figure 3.3, in terms of the equivalent optical power (to the DC offset voltage) against temperature. At 27 °C the DC offset voltage shifts by about 0.06mV. °C^{-1}, equivalent to 1.5pW. °C^{-1}. At 40 °C, the DC offset voltage shifts by about 0.47mV. °C^{-1}, equivalent to 11.85pW. °C^{-1}.

The third step was to identify whether the detection of a "pulse" of fluorescent radiation with a resolution of order 100fW was achievable. The detector/amplifier was removed from the environmental chamber and approximately 1 metre of 1mm core diameter polymer fibre was fed into the detector/filter housing. An instrumentation amplifier with a voltage gain of x1, x10, x100 or x1000 and low-pass filtering at 1Hz or 1kHz was constructed. The instrumentation amplifier was fed by the output of the photodetector/amplifier hybrid and powered by ±12V from batteries. Light from a white light source was passed through a chopper and variable attenuator, collected by the polymer fibre and passed through the Schott filter onto the photodetector surface. With the

amplifier set to x1000 gain and using the 1kHz band-pass filter, a peak-to-peak signal of 400mV (10pW) was established. The chopper was then removed, a 20dB filter was placed between the light source and the fibre to provide an illumination level of 100fW, the instrumentation amplifier filter was set to 1Hz, and the amplifier output was recorded continuously. After recording for some minutes, a piece of black card was inserted between the light source and the polymer fibre. After approximately 1 minute it was removed again. Despite evidence of drift and noise, there was clearly a reversible step change in the recorded signal, which was greater than the short-term noise. In the

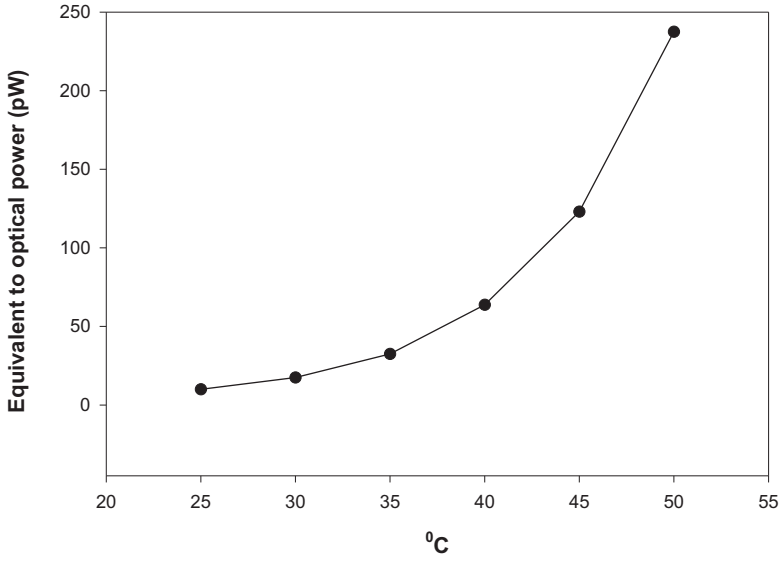

FIGURE 3.3: Dependence of equivalent optical power to DC offset on temperature

case of short-term non-automated measurements in a well-controlled laboratory environment, the detection of a "pulse" of fluorescent radiation with a resolution of order 100fW was determined to be feasible using the chosen detector/amplifier combination. However, in an instrument where temperature drifts considerably, where there may be other environmental noise sources at very low frequency, and where the signal acquisition must be automated, it will be necessary to employ some form of noise/drift reduction. While it would be undesirable to add unnecessary extra costs to a production instrument, there is a good case for adding extra flexibility to a research instrument, which can be removed in a production instrument after the R and D phase is complete. The most flexible way to provide a means to study different noise-reduction techniques, including "lock-in" detection, would be to implement them in software, as suggested by Siemens, a partner of the consortium. The most cost-effective means to realise the instrument that is required to provide an on/off modulation of the laser input at frequencies up to, say,

300Hz, for acquisition of the modulated fluorescence signal, and for digital lock-in techniques. However, for cost reasons, lock-in detection was not selected by the AWACSS consortium, but it was decided to include temperature monitoring of the detectors.

3.4.2 Microfluidics and electronic components

Optimal performance of the immunoassay system is dependent upon the efficient utilisation of fluorescence-labelled antibodies to detect the presence of specific analytes in the water sample. These analytes are transported to the sensor transducer by the microfluidic system where they bind to specific regions on the sensor surface to produce the transducer signal. The signal intensity is therefore dependent upon the binding efficiency and contact time between antibodies and binding sites. The proportion of antibodies that is made available for binding is also dependent upon the dimensions of the flow cell. As the depth of the flow cell is increased, less of the antibodies fall within the diffusion capture range of the binding site and the sensitivity of the assay decreases. The concentrations of antibodies required to give optimal performance are calculated during the calibration runs, but if the depth of the flow cell varies significantly from one binding region to the next, assay performance will be compromised. The flow cell used in this study was designed and fabricated by CRL. Prototypes of the microfluidic channel were fabricated in acrylic polymer by CRL using a hot emboss technique (71; 72), and trials of fluid flow through the device were carried out.

Figure 3.4a shows plan and elevation views of the flow-cell. The width is 5mm, to cover the 3mm wide waveguide region and the length is 24 mm. The targeted channel depth of the flow-cell is 35μm, but fabrication tolerances caused it to vary between 35μm and 50μm from device to device. The flow channel height is chosen to be as small as possible so that transport of molecules to the sensor surface is fast and measurement times are kept low, but not so small that it is easily blocked or so that manufacturing tolerances become impractically stringent (73). The shape of the flow-cell from the plan view is designed to result in laminar flow with the velocity profile shown in Figure 3.4b. While the flow rate over the outer rows of sensing patches is 80% of that over the central rows, differences in resultant binding fractions are expected to be corrected in calibration of the sensor.

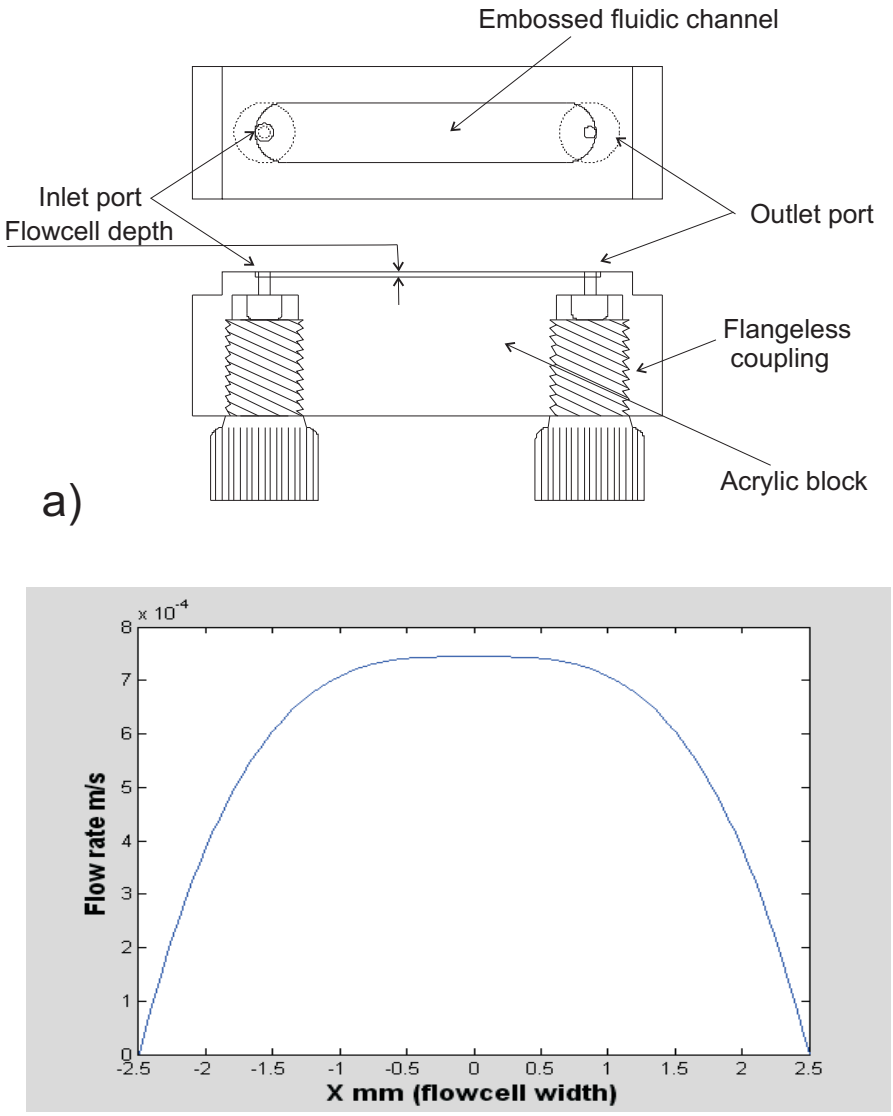

FIGURE 3.4: Flowcell schematic. a) The flowcell design (dimension 24mm x 5mm x 50μm approximately), and b) The flow profile across the flowcell with 0.1ml.min^{-1} flow rate.

The design and fabrication of the trial sensor mounting block contains 32 fibre optic cables (optical fibre single core polymer 368-047 (RS Components)) which conduct the fluorescence from the chip to the detectors. There are two built-in temperature sensors which monitor the temperature of the sensor surface and the photodiodes. The sensor block is interfaced with an array of 32 independent photodiodes and filters, which are hard-wired to amplifier circuits and, via low noise interconnects, to the interface with the main pc controller, supplied by Siemens. The technology for precise and semi-automatic cutting of sensor chips to align with the collection fibres to within $\pm$50μm has been

established. Figure 3.5 shows a sensor chip attached to the CRL block.

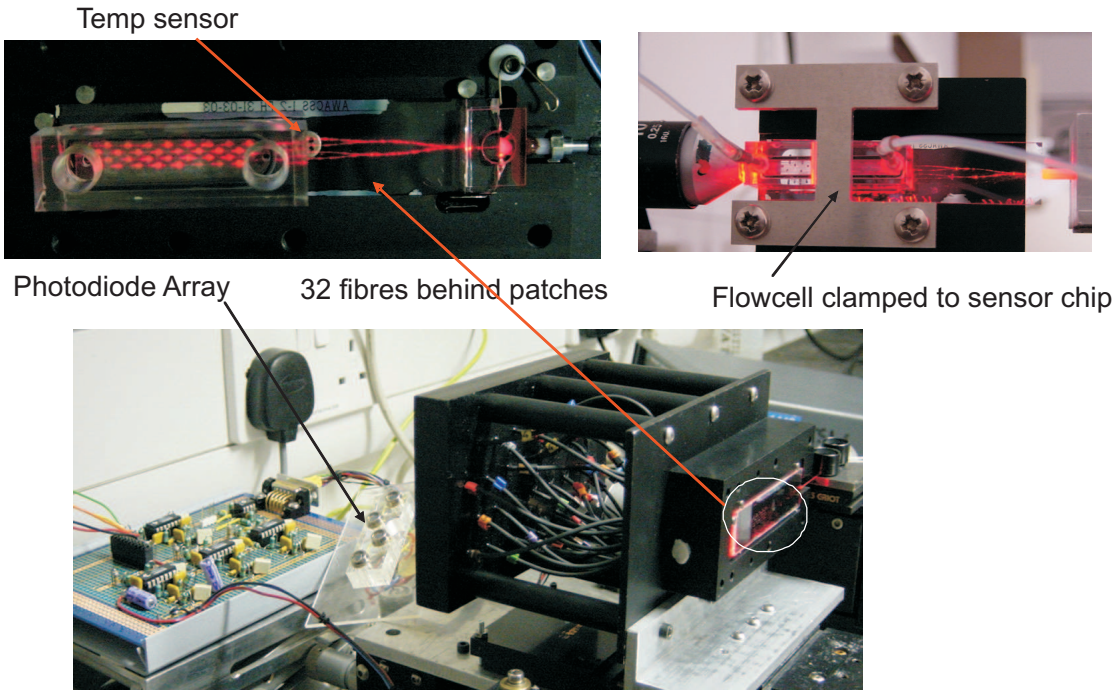

FIGURE 3.5: Photo shows a sensor chip in a CRL block.

3.4.3 Optical component selection and testing

Having selected the photodetector and receiver electronics, the peripheral optical components were specified, selected and tested. The testing work was carried out jointly with Patrick Hole. A Point Source laser diode module (iFLEX-1000), which emits approximately 5mW at 637±2nm and is connected to a polarisation-maintaining fibre, was selected since it met the power and wavelength specifications and was packaged ready for use. Although a 635nm version was considered, in order to reduce pump breakthrough of the fluorescence filter, this had the disadvantage of lower power and a reduced power reliability. The latter was, however, used for the dye fluorescence measurements, described in the next chapter, due to the laser diode module (iFLEX-1000) not being available at the time for the dye experiment. Measurements on suitable fluorescence filters and on the 637nm versions showed that there was little difference in the behaviour of these modules, so that the standard 637nm version was selected. The power spectra of the two lasers used in the experiments are shown in Figure 3.6. The wavelength for both lasers are 635.5nm and 637.7nm respectively.

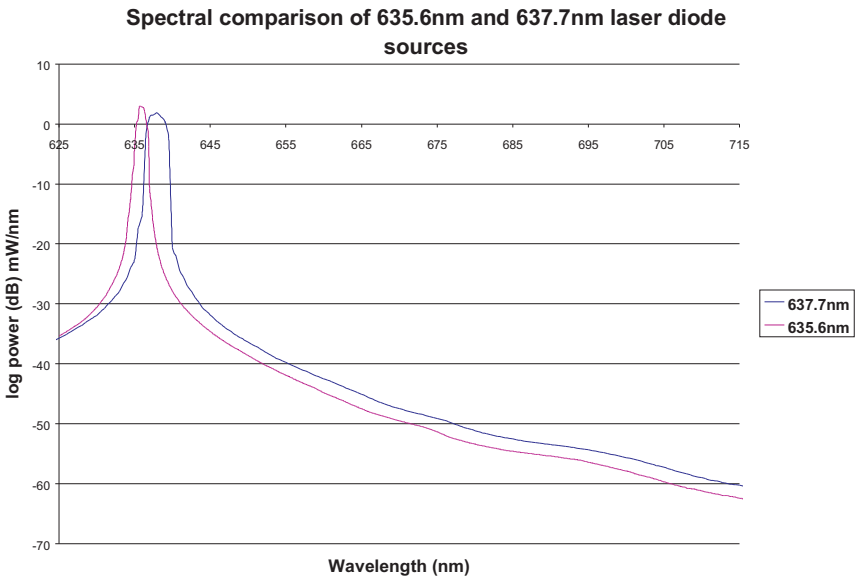

FIGURE 3.6: Laser power spectra.

Sample filters had been provided by NDC Infrared (74) for testing. These included 690/4, 690/6, 700/4 and 700/6 (centre wavelength/fractional wavelength% (74)), and the relative transmission from fluorescing Cy5.5 was measured for each one. Figure 3.7 shows the emission spectrum of Cy5.5 dye excited at 633nm. Figures 3.8 and 3.9 show the transmission spectrum of the selected filter. The diameter of the filter is 5mm±0.1mm and the thickness is 2.7mm±0.1mm. In trials, pump breakthrough occurred with the 690/6 filter. The pump breakthrough is a potential problem, as it tends to saturate the detection channels and, furthermore, any fluctuations in the pump breakthrough will manifest itself as noise in the received signal, causing the detection limit to deteriorate. Overall, the 700/6 combined with absorbing and interference layers was found to be the most suitable filter. Subsequently filters with 695/2.5 characteristics also became available, but it was felt that these would probably restrict the amount of light transmitted.

3.4.4 Electronic signal filtering and processing

The outcome of the preliminary test of the photodetector/amplifier (described in Section 3.4.1 of this chapter) has shown that at 700nm wavelength the photodiode has a response of approximately 24mV/100pW incident power. A non lock-in detector system was selected for the instrument which included a 4^{th} Order Butterworth Low-pass Filter,

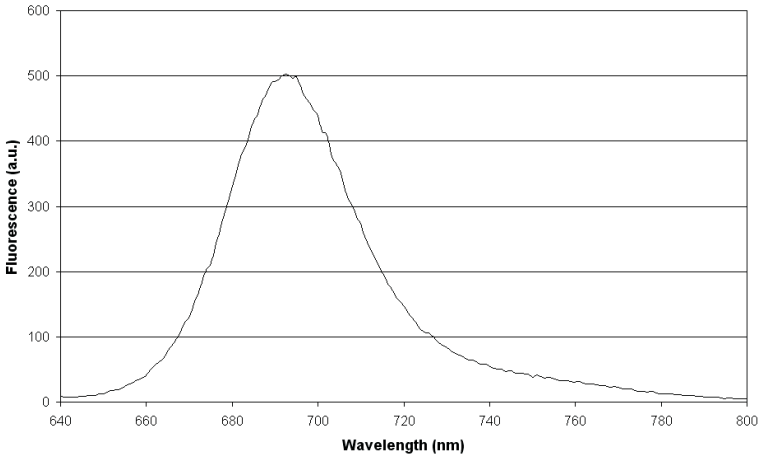

FIGURE 3.7: Emission spectrum of Cy5.5 dye excited at 635nm.

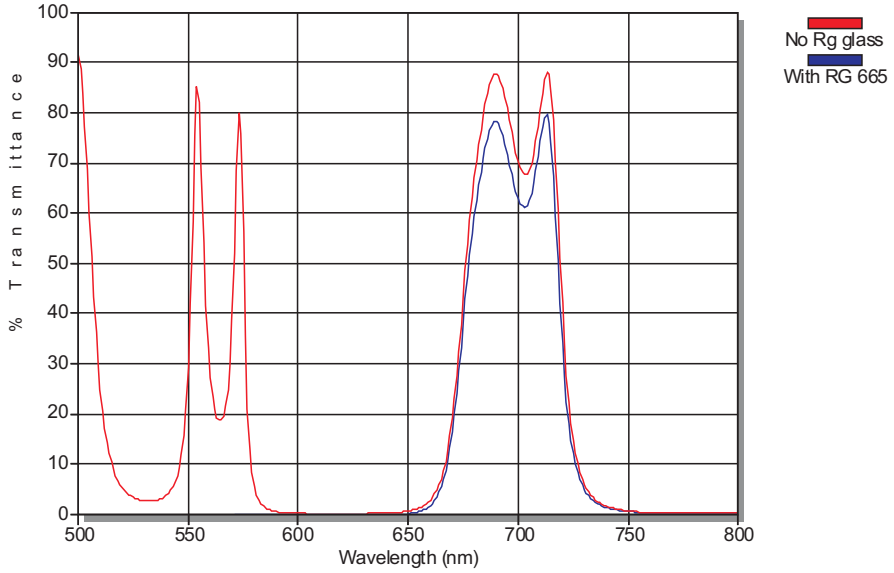

FIGURE 3.8: Transmission spectrum of 700/6% filter.

this approach was suggested by CRL, and was approved by the project partners, who were involved in design of the detection system including the author. In this section, a description of the 4^{th} Order Butterworth Low-pass Filter used in the system in order to suit the above requirement is given, with detailed analysis in Appendix B.

3.4.4.1 The 4^{th} Order Butterworth Low-pass Filter in the system

In order to accommodate the requirements of the system, as mentioned at the beginning of this section, the 4^{th} Order Butterworth Low-pass Filter was chosen for the system.

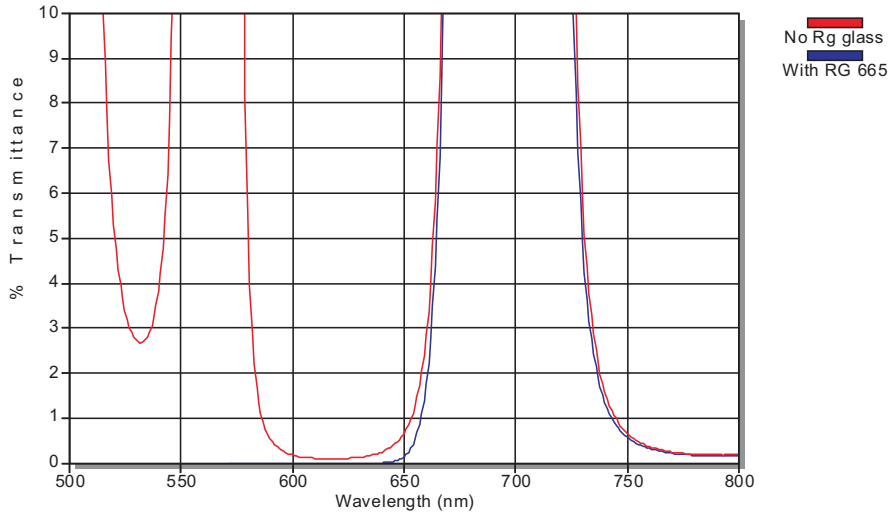

FIGURE 3.9: An expansion of transmission spectrum of 700/6% filter.

The circuit shown in Figure 3.10 addresses the requirement of the system.

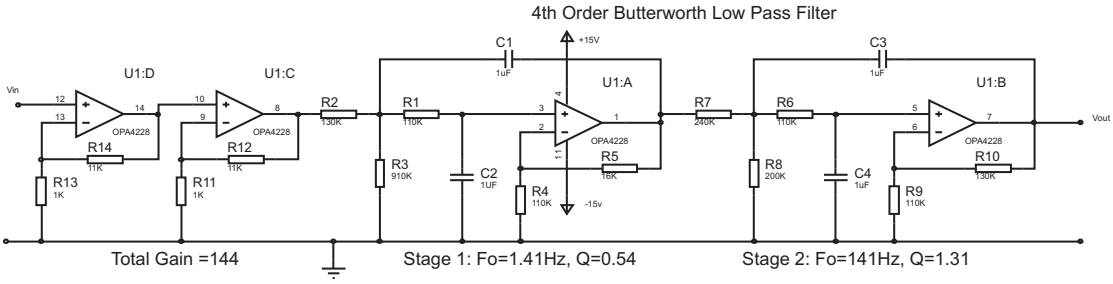

FIGURE 3.10: AWACSS Photodiode Circuit: Amplifier-Filter Stage

Note that the final magnitude of the gain is dependent on the actual light output of the sensor device and the output measurements indicated that a gain of approximately 1350 was required and designed.

Based on the value of resistors and the capacitors given in the circuit Figure 3.10 and the parameters of the transfer function, equation 3.2 can be obtained via solving the set of nodal equations.

$$H(s) = \frac{1}{(0.0125s^2 + 0.2067s + 0.9977)(0.0121s^2 + 0.0909s + 1.0076)} \tag{3.2}$$

in which $s = j\omega$. More details about the transfer function in equation 3.2 and data processing will be given in Section 5.5 in Chapter 5.

3.5 Detection system

Fluorescence measurements were carried out in order to characterise the sensor system in terms of patch-to-patch uniformity and the system detection limit. Detailed fluorescence experiments are given in the next chapter.

It has been mentioned, in Section 3.4.1 of this chapter, that a worst-case detection limit for changes in fluorescent intensity of about 100fW was projected based on the RIANA project (70). Based upon this data, the decision to employ a preamplifier detection system based on a photodiode array in the sensing system was made, and the detection system was then designed and built by CRL. Each channel gain has been adjusted to 1350, allowing a maximum signal of about 200pW and the detection limit is below 0.5pW corresponding to a NEP of about 160fW for a bandwidth of 1.4 Hz. This is very close to the specification and the detection limit, using this system with the pigtailed chips and a commercial FIA, details are given in the next chapter.

The limit of detection is defined as the concentration at which the signal equals the mean value plus three times the standard deviation and is expected to allow detection below 1% of the blank value (75).

A preliminary measurement of the photodiode (PD)(Centronic OSI 5-IR-100M/1K) signal to noise distribution at room temperature (RT) was performed without using the built in amplification and filter circuitry. The investigation of the noise spectrum of the photodiode, with an integrated pre-amplification circuit, yielded a minimum near 1Hz. Measurements at different stages within the CRL detection unit circuitry confirmed the good operation of amplification and filter stages. Using the Lock-In method @ 177Hz chopper frequency and the built in amplification circuit a PD signal standard deviation of about 1.7mV was measured. The slow integrating DC measurement with use of the built in amplification and a 1 Hz low-pass filter circuit yielded a standard deviation of below 1mV. This result compares well to the noise spectrum minimum value at 1Hz. 1mV signal was found to correspond to 160fW, so that the minimum detectable signal

change, corresponding to 3 standard deviations, was found to be 500fW. This confirmed what was discussed in section 3.4.1.

All components of the system were assembled, including the CRL final instrument, computer control hardware and software, auto-sampler and sensor chip. The hardware (optical, electronic and fluidic) and software has been tested. Figure 3.11 shows a photo of the interface between optical bench and electronics.

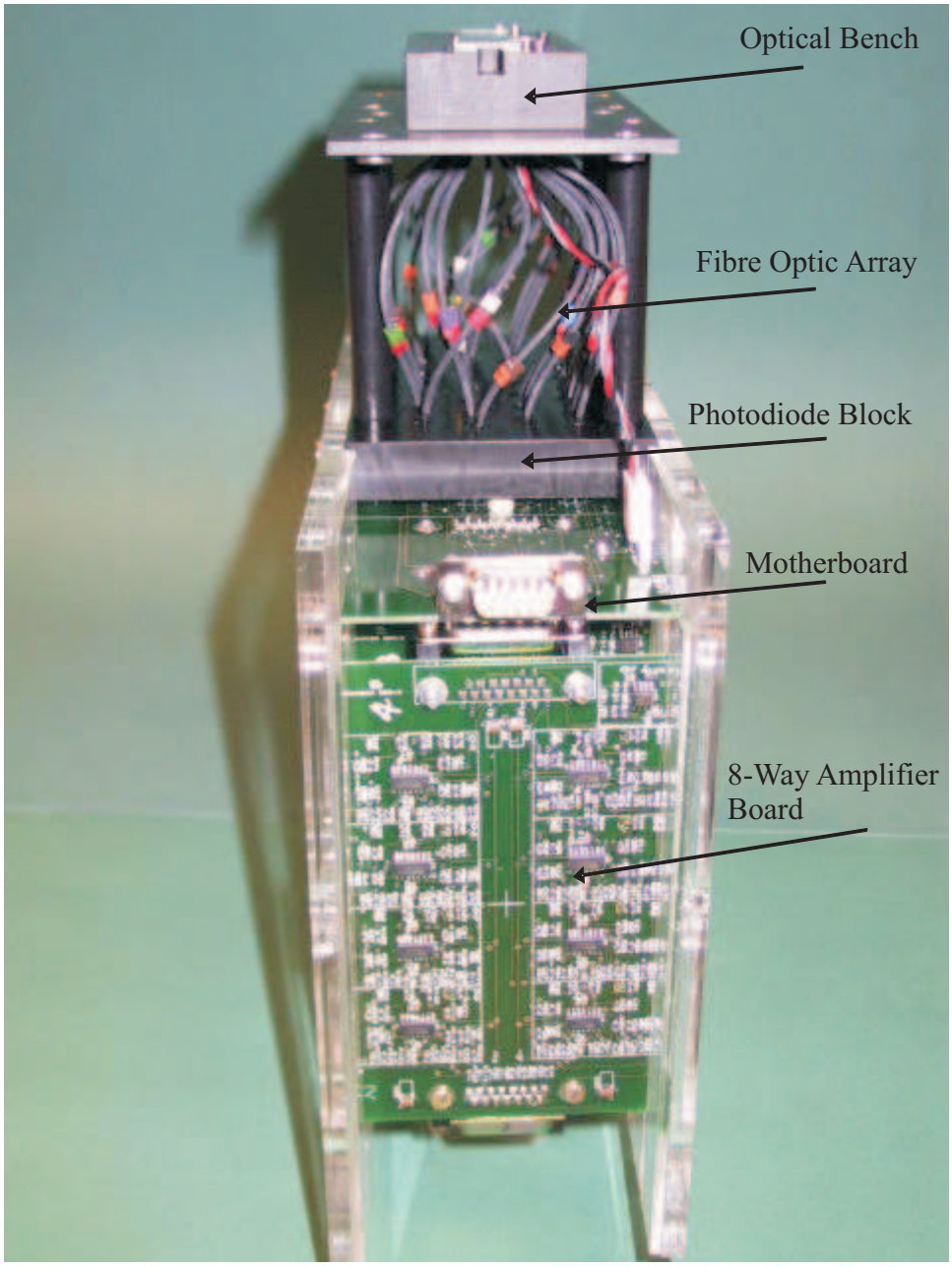

FIGURE 3.11: Interface between Optical Bench and Electronics, constructed by CRL.

3.6 Conclusion

This chapter addresses detailed study on electronics, fluidics and part of optics and their selection for the instrumentation, in terms of hardware requirements for the multi-sensing system. A study on optical power estimation of the system was delivered hence enables a detailed design of the detection system.

The author has worked closely together with CRL, Siemens and Tübingen University in the design of the final detection system, the involvement including, the laser selection, laser to chip connection, detector selection, filter selection, detector pre-amplifier, signal processing, and the integration of sensor chip to the microfluidics system and to the optical fibre array connection. In addition, the author supplied pigtailed sensor chips to other partners for varies trials.

The choice of using the detection system discussed in this chapter mainly because of its low cost. Preliminary research and experiments have been carried out and have proved the feasibility of the sensing system. The complete system, including components of optics (the sensor chip), hardware (instrument, computer, and auto-sampler) and software, was assembled and tested. The optical detection limit of the full system, defined as 3 x NEP, has been found experimentally to be equivalent to ∼500fW of fluorescence power.

A detailed analysis was given on how the signal filter works and also a brief introduction of the 4^{th} Order Butterworth Low-pass Filter used in the system. The photodiode itself operates best at 1 Hz measurement frequency. Fast signal changes induced by the laser, power supplies or fluidic components could not be eliminated by any of the investigated measurement techniques. But, by optimizing the design and construction of the system, these changes can be reduced or eliminated. Influences of slowly varying ambient light changes or thermal drifts could be avoided by the use of Digital Lock-In methods which involves controlling the computer and software environment or a more adequate construction of the unit housing.

Chapter 4

Fluorescence Measurements and Sensor Chip Characterisation

4.1 Introduction

Fluorescence power measurements have been carried out using various concentrations of bulk dye solutions of Cy5.5 in water, using a commercial flow-injection system to supply sequences of solutions to the sensor surface, in order to confirm low-noise operation of the detection system and determine the ultimate detection limit in terms of the number of Cy5.5 molecules per unit area. Signal strength, noise and drift have been quantified for the detection system.

This chapter presents the bulk dye experiment in detail and the results obtained, and compares these results with the theoretical predictions.

During the characterisation process, improvements were implemented in adjusting the optical circuit layout and in the fabrication process (which was addressed in Chapter 2), hence, a direct comparison between two generations of sensor chips has also been possible.

4.2 Fluorescence measurements

Preliminary tests were initially carried out with a custom made optical block in which the sensor chip can be fitted and the fluorescence can be collected from the backside of the sensor chip via a single fibre, which can be moved from one patch to another manually. This approach was aimed at using the available resources more efficiently, as the sensor chip characterisation could be carried out at the same time as the final AWACSS instrumental block was being prepared in CRL.

Figure 4.1 shows a sensor chip fitted in the optical block and with a flowcell attached.

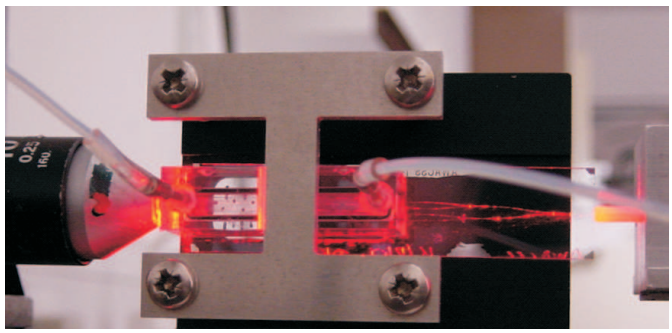

FIGURE 4.1: Sensor chip and flowcell mounted in a home-made block.

Light from the semiconductor laser, with an output power of 3mW at 635nm, was coupled into a single-mode polarisation-maintaining fibre, which was butt-coupled to the sensor chip instead of using fibre pigtailing thus resulting in less stable coupling in this case. A microscope lens was located at the output end for optimising the coupling light. The chip was deposited with 25nm tantalum pentoxide in order to enhance the signal. Cy5.5 dye from Amersham Pharmacia was chosen for the bulk dye experiments. Sequences of solutions of deionised water and bulk dye with concentrations between 10^{-6} to 10^{-8} Molar Cy5.5 were delivered to the sensor surface via a lab flow-injection analyser (FIA). An OSI 5-IR-100M/1K photodiode was used as a detector and signals acquired with a commercial lock-in amplifier. The fluorescence was excited with a peak wavelength of approximately 700nm and was collected by a high numerical aperture polymer optical fibre located under each sensing spot of the sensor chip; the pump light was removed from the signal by a filter before the photodiode. The diode signal was acquired by a commercial SR810 lock-in amplifier (from Stanford Research Systems) and recorded by a computer using LabView software.

Figure 4.2 shows a result of a dye experiment using the above set up, the concentration of dye is 0.92x10^{-6}M Cy5.5.

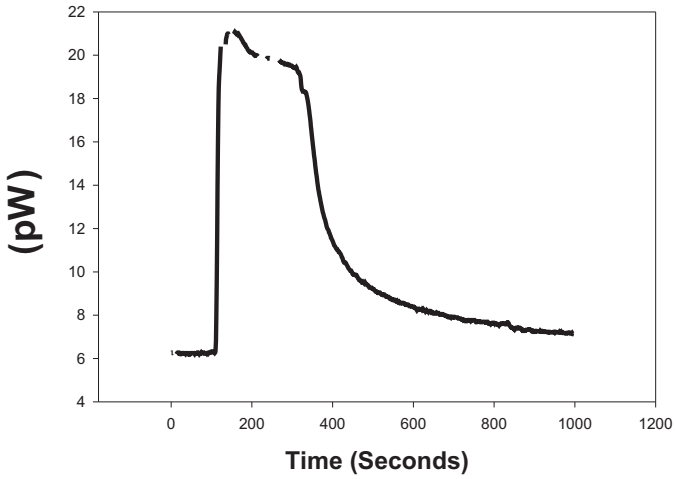

FIGURE 4.2: 0.92x10^{-6}M Cy5.5 test. The slow trailing edge is due to the mixing of washout and the dye solution diffusing into the pure water (sample No. 11-3-32).

The signal is defined as an averaged signal over a series of data in the peak region of the dye pulse, in which the background signal was deducted. The background signal was an averaged signal over two parts, the first part of the signal was taken before the beginning of the dye pulse and the second part was the signal taken after the dye pulse. The limit of detection here is defined as three times the dye concentration divided by the signal to noise ratio. Here the noise is defined as the square root of the squared standard deviation of the signal and the squared standard deviation of the background signal (noise=$\sqrt{\sigma^2_{signal} + \sigma^2_{background}}$). Therefore, a detection limit below 2 x 10^{-8} M Cy5.5 was determined for the 1^{st} generation sensor chip.

In Figure 4.2, the dye concentration has been chosen to give a similar peak fluorescent signal to that of a "blank" immunoassay measurement. The signal is 15pW, but this will be increased by a factor of 2 if lock-in detection is not used and also increased with the high power laser to be used in the instrument, so that at least 50pW of signal can be expected. In this experiment to measure the fluorescence from bulk dye solutions, the dye sample was loaded with a flow rate of 1.4 ml.min^{-1} for 5 minutes. Subsequently, the dye solution was washed out of the cell with the fixed pump flow rate of 0.56 ml.min^{-1}. The change of flow rate from fast to slow shows an effect of sudden cut-on in, and a slow trailing edge at the washout end, due to the mixing of washout and the dye diffusing into the pure water.

4.3 Patch-to-patch uniformity

A good patch-to-patch uniformity means that the measurements from all 32 patches will have a similar dynamic measurement range. Uniformity of the signal from the 32 patches was assessed by scanning an individual fibre underneath the chip while the cell was filled with 10^{-6}M Cy5.5 dye, as shown in Figure 4.3. Background signal strength

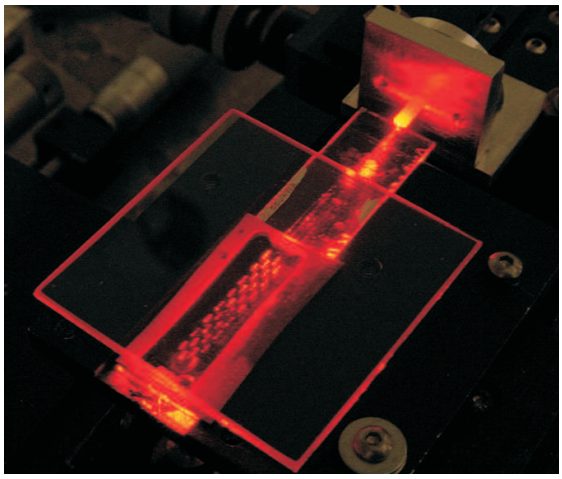

FIGURE 4.3: Setup for patch-to-patch uniformity measurement.

was recorded, which was the average of the measured signal strength at 4 spots adjacent to the patches, this average background signal of 1.3mV, equivalent to 32pW, was subtracted. 16 patches attained ∼15pW with 10^{-6}M Cy5.5 and 16 patches yielded 135±30pW, Figure 4.4 shows the mapping of the uniformity of the 32 patches with 10^{-6}M Cy5.5 dye solution;

Figure 4.4 shows the mapping of the uniformity of the 32 patches with 10^{-6}M Cy5.5 dye solution. Uniformity was reduced after applying the tantalum pentoxide high-index film. The intensity decay along the patches was mainly due to the high-index film which pulls the intensity field towards the sensor surface, resulting in an increase in the signal strength decay rate. Absorption and scattering losses inside the Ta_2O_5 also contributed to the intensity decay. Annealing the device could reduce the attenuation due to reducing the optical absorption in the Ta_2O_5 film (13). A direct comparison with the patch-to-patch uniformity of the new generation sensor chips will be discussed in the section below.

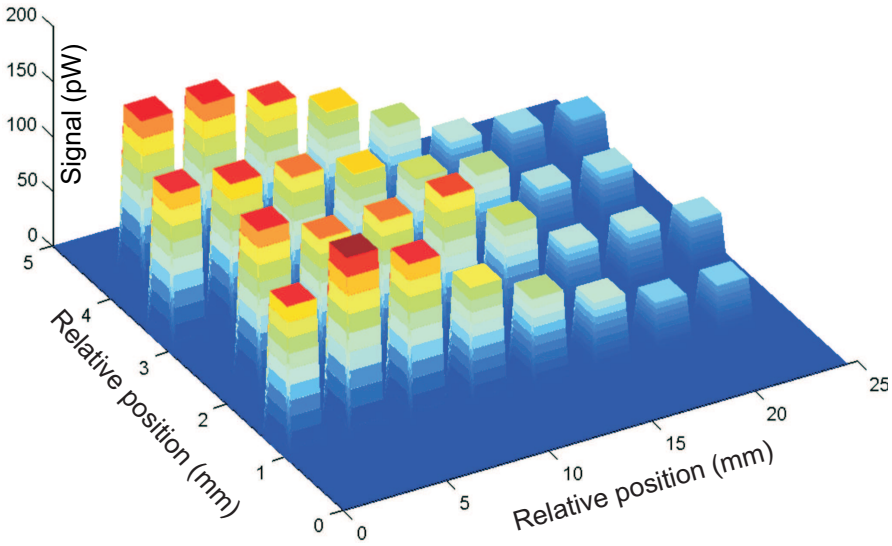

FIGURE 4.4: Mapping of the uniformity of the 32 patches with 10^{-6}M Cy5.5 dye on the 1^{st} generation sensor chip coated with Ta_2O_5 film.

4.4 Comparisons between 1^{st} and 2^{nd} generation sensor chips

This section presents the dye experiment results of the new generation sensor chip and the direct comparison with the first generation sensor chips.

4.4.1 Bulk dye experiments

Dye experiments have been carried out again using bulk dye solutions of 10^{-6}M-10^{-9}M Cy5.5 in water, with a commercial flow-injection system to supply sequences of solutions to the sensor surface with CRL instruments. All CRL electronics were used for these trials (240V AC input to instrument, all 32 photodiode outputs and both temperature outputs).

4.4.2 Chips with and without Ta_2O_5 over-layer

4.4.2.1 Limit of detection

The best case LOD for the newly fabricated chips coated with Ta_2O_5 layer (Figure 4.5) has reached 7.7x10^{-11}M bulk Cy5.5 in water, it is about 130 times better than

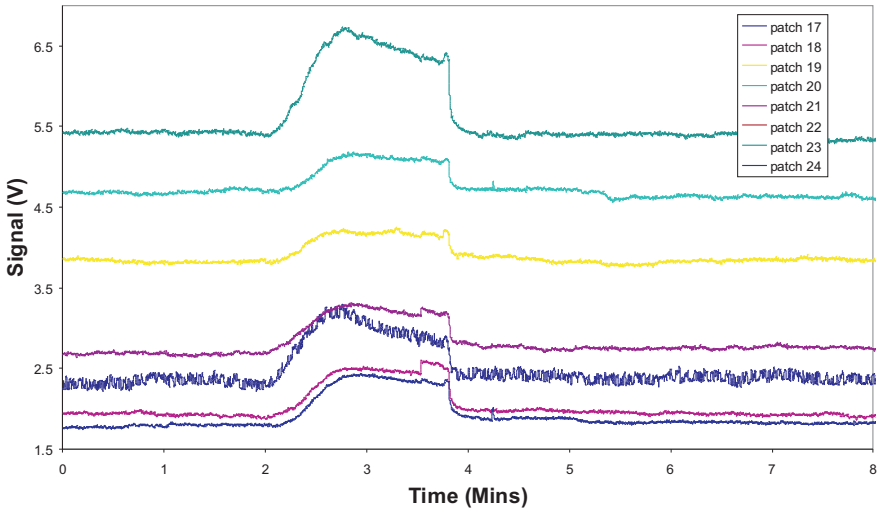

FIGURE 4.5: 10^{-9}M Cy5.5 on new generation chip sample 14-2 with Ta_2O_5 film @ RT=29 °C.

previously fabricated 1^{st} generation sensor chips, and it is about 36 times better than what was achieved before adding the Ta_2O_5 film (Figure 4.6), this is agreed well with the theoretical prediction in Figure 2.12, which shows the enhancement factor of 36 for the 35nm Ta_2O_5 film (the index of the Ta_2O_5 film is 2.1).

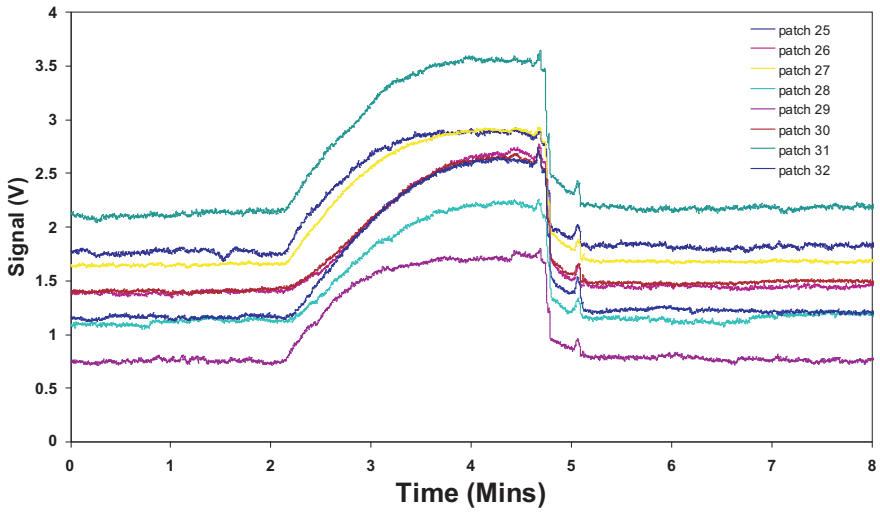

FIGURE 4.6: 10^{-6}M Cy5.5 on new generation chip sample 13-2 without Ta_2O_5 film @ RT=29 °C.

Discussion: the comparison of the flow profiles between Figure 4.5, Figure 4.6 and Figure 4.2.

The flow regime was identical for the experiments shown in Figure 4.5 and Figure 4.6, with a slow flow rate of 0.42 ml.min^{-1} when the dye sample is introduced, the duration of sample loading is 3 minutes, and a fixed pump flow rate of 0.56 ml.min^{-1} when the washing out starts. The slow flow rate shows the effect of the dye solution diffusing into the water in the cell, and the change of flow rate from slow to fast shows the effect of sudden cut off. The difference between Figure 4.5 and Figure 4.6 is in the dye concentrations, and Figure 4.5 also has a 35 nm Ta_2O_5 film coated on the sensor surface which shows higher sensitivity than the result of Figure 4.6 in which the sensor chip has no high-index coating. The reasons for the difference in diffusing in the leading edge are unknown.

The flow regime in Figure 4.2 was different from the above experiments. It has a fast flow rate of 1.4 ml.min^{-1} for loading the dye sample, the duration of sample loading is 5 minutes, and the fixed pump flow rate of 0.56 ml.min^{-1} (the same as the above) when dye solution was washed out from the cell. Therefore, the change of flow rate from fast rate of 1.4 ml.min^{-1} to slow rate of 0.56 ml.min^{-1} shows a sharp cut-on in, and a slow trailing edge at the washout end, due to the mixing of washout and the dye diffusing into the pure water.

The detection limit of the system also means that the system is able to resolve 1% of blank measurement. The peak signal for a blank measurement is expected to be equivalent to a bulk dye concentration of 1.46 x 10^{-6}M Cy5.5 in water. If a detection limit of 10^{-10}M Cy5.5 is assumed, then the minimum detectable surface density of Cy5.5 could be worked out.

As we only detect dye molecules within the evanescent field, which extends of order d = 100nm from the waveguide surface, we can estimate how many molecules per unit area this concentration corresponds to.

This surface density is denoted as ρ, and may be calculated as follows:

$$\rho = 1000\ D_l N_A d_p$$

(Note: the units are molecules.m^{-2}; a factor of 1000 is required to convert L to m^3, 1mol/1000cm^3=1M). Where D_l is the bulk detection limit of the system, N_A is Avogadro's number = 6.02x10^{23}(molecules.mol^{-1}), and d_p is the penetration depth of the evanescent field:

$$d_p = \lambda/[2\pi(N_{eff}^2 - {n_2}^2)^{1/2}]$$

Where λ is the wavelength of the laser, N_{eff} is the effective index of the waveguide mode, and n_2 is the refractive index of the analyte.

For λ =635nm, $N_{eff} = 1.51$, and $n_2 = 1.339$, we obtain $d_p = 145$nm

This results in a surface density detection limit of 8.73x10^9 Cy5.5 molecules.m^{-2} or 8.73x10^3 Cy5.5 molecules.mm^{-2}, and it is equivalent to 4.36 x10^3 antibodies.mm^{-2}, this is at least one order of magnitude better than the detection system requirement.

4.4.2.2 Patch-to-patch uniformity

The patch-to-patch uniformity measurements were carried out on the new generation chips using the CRL semi-finished set up. Although this would limit the number of data points collected to 8 in each dye measurement, it is still an improvement in the measurement efficiency when compared with the previous method, in which fluorescent signals were collected by scanning an individual fibre underneath the chip from patch to patch manually. It was found from the measurements that about 80% of the patches reached a LOD of 2.8x10^{-9}M Cy5.5, compared with previous measurements in which 46% reached an LOD of 8.1x10^{-9}M Cy5.5. Figure 4.7 shows the patch-to-patch uniformity measurement on sample 13-2 before adding the Ta_2O_5 layer. Figure 4.8 shows the patch-to-patch uniformity for sample 14-2 coated with a 35nm Ta_2O_5 film. The decreasing signal from the patches along the length of chip is mainly due to the Ta_2O_5 film which pulls the modal field towards the sensor surface, resulting in an increase in attenuation due to increased surface scattering and scattering at the beginning and end of each sensing window. Optical absorption in the Ta_2O_5 may also contributed to the intensity decay, and this may be reduced by annealing the device to reduce oxygen deficiencies (13). During the measurement in the latter case, air bubbles were observed in the flow system. These air bubbles could cause the signal to fluctuate as they prevent the

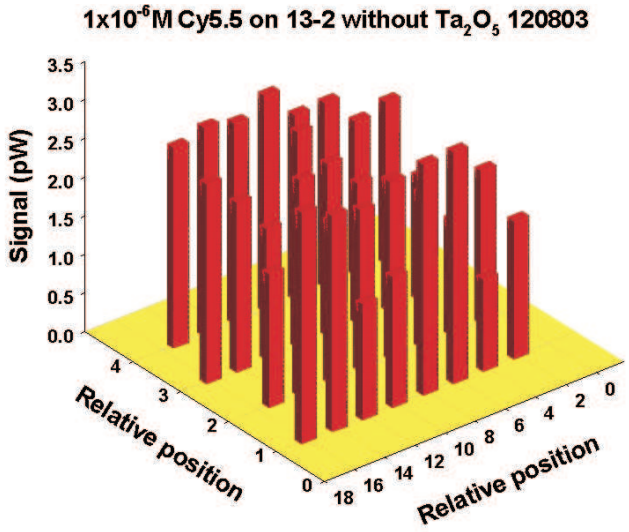

FIGURE 4.7: The patch-to-patch uniformity measurement on sample 13-2 before adding Ta_2O_5 film. Data was obtained from 8 patches at a time.

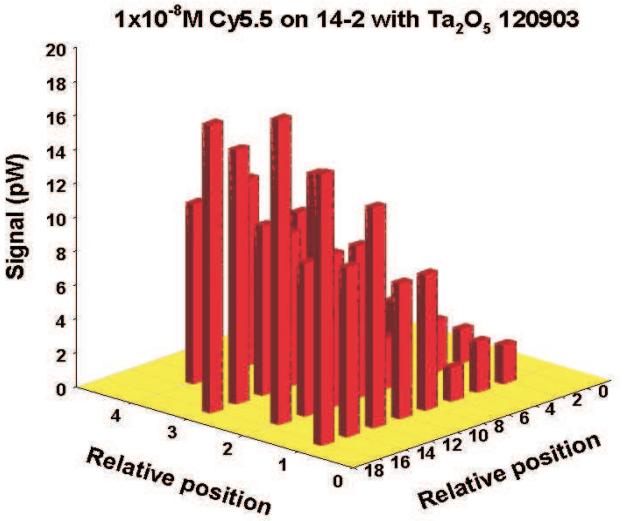

FIGURE 4.8: The patch-to-patch uniformity measurement on sample 14-2 after adding 35nm Ta_2O_5 layer. Data was obtained from 8 patches at a time.

dye solution from contacting the patch surface fully. There is still room for optimising the thickness of the Ta_2O_5 film as a trade-off between sensitivity and the uniformity.

Discussion: The desired thickness of Ta_2O_5 for the 2^{nd} generation sensor chip sample 14-2 was 15 to 20 nm, in order to make direct comparison with the 1^{st} generation sensor chip in terms of signal uniformity, since the uniformity was degraded after applying a 25nm of Ta_2O_5 film on the sensor chip described in section 4.3. Unfortunately, the sputtered Ta_2O_5 film thickness on sample 14-2 was 35nm despite using the same conditions as before (due to unknown experimental variations). Although the chip achieved the better

detection limit of 7.7x10^{-11}M Cy5.5 compared with 2.8x10^{-8}MCy5.5, addition of the Ta_2O_5 film compromised the uniformity of the sensor chip.

4.5 Comparisons of theoretical and experimental results

Table 4.1 presents both theoretical and practical results for the photodiode array detector system. The calculation result was made under conditions of 1% of maximum assay response (blank measurement) with 1mW input laser power in the waveguide. The second row in the table shows that 0.93pW.mW^{-1}@10^{-8}M and 0.73pW.mW^{-1}@10^{-8}M should be expected for the collected fluorescence power by the tapered waveguide opening with 30μm and 60μm respectively.

The 52pW.mW^{-1}@10^{-8}M listed in the third row of the table was the result of the bulk dye experiment on the first generation sensor chip with a 30μm taper waveguide opening. The chip was coated with 25nm Ta_2O_5 film and it has a total loss of 14dB (6dB loss due to the four-way split and 6dB and 2dB due to the transmission and silica layer loss respectively). The bulk dye experiment was carried out with a lock-in amplifier, and the final result of 52pW.mW^{-1}@10^{-8}M took into account the effect of this lock-in. It is also assumed that the fluorescence intensity is proportional to the concentration of the dye.

The second generation sensor chip has a good improvement in terms of coupling efficiency and optical loss in the waveguide compared to the 1st generation sensor chip. The result from the fourth row of 2.2pW.mW^{-1}@10^{-8}M (without Ta_2O_5 layer) was obtained for the new generation sensor chip, which is comparable with the theoretical result. The SNR of 152 and the LOD of 2x10^{-8}M were achieved with this sensor chip.

A result of 253pW.mW^{-1}@10^{-8}M was achieved for sensor chip No 14-2. The chip has a 35nm Ta_2O_5 film coated on its surface. The LOD of 7.7x10^{-11}M of Cy5.5 was also achieved with this sensor chip.

Overall, the theoretical prediction of 0.23 pW.mW^{-1}@10^{-8}M fluorescence power collection should be reached if one takes the 4-way split waveguide structure into account for a 30μm taper waveguide, so it is in reasonable agreement with the experimental result of 2.2 pW.mW^{-1}@10^{-8}M for the same waveguide (assuming a linear response of the

concentration of dye with the fluorescence signal power), since the laser power in the waveguide was an estimation, it could be higher in practice.

PD Detetor System	Estimated Laser Power in WG(mW)	Estimated /measured Power in WG(μW)	Dye Conc. (M)	WG width (μm)	Fluorescence Output for WG width 30&60 (μm)	pW.mW^{-1} at10^{-8}M
In theory*	1	1000	1.2x10^{-8}	30/60	1.12pW /880fW	0.93(30μm) 0.73(60μm)
In practice 1st Generation**	0.6	24	0.92x10^{-6}	30	15pW	52 (With 25nm Ta_2O_5 film)
In practice 2nd Gen. 13-2***	1	63	10^{-6}	30	2.8pW	2.2(No Ta_2O_5 film)
In practice 2nd Gen. 14-2***	1	63	10^{-8}	30	16pW	253 (With 35nm Ta_2O_5 film)

Note:	
*	under the condition of 1% of maximum assay response (blank measurement)
**	Lock-in Amp. was used for the experiment, 6dB loss due to the 4-way split. Transmission loss was 6dB and silica layer loss was 2dB.
***	6dB loss due to the 4-way split. 5dB transmission loss and 1dB silica layer loss.

TABLE 4.1: Comparing the theoretical result with experimental outcomes of the fibre collection and photodiode array detector system.

4.6 Conclusion

This Chapter addressed bulk dye experiments and discussed the results for both generation sensor chips. The newly fabricated sensor chip has increased improvement in terms of low loss, robustness and with a LOD well within the specification. A direct comparison between the experimental results and the theoretical calculations were carried out and the results were comparable. Optical parts and electronic parts of the instrument were assembled and functioned successfully. Further improvement and optimisation of devices, instrument parameters and signal processing will depend on the real signal and data from immunoassay trials.

Chapter 5

Surface Chemistry, Immunoassay Experiments and Data Processing

5.1 Introduction

The immunochemistry utilised in this research work takes advantage of a binding inhibition test that requires antibodies directed against specific analytes and analyte derivatives that can be covalently bound to a transducer surface.

A huge number of polyclonal antibodies and their corresponding analyte derivatives have been produced for a variety of organic micro-pollutants. After being purified and labelled with a fluorescent marker, they were developed into immunoassays and used in this study.

This chapter describes the surface chemistry modification, the detection limit of the sensing system, the procedure of the immunoassay experiment, and the response of the measurement result of different concentrations of an analyte, which forms a calibration curve. This curve subsequently can be used for detecting an unknown concentration of the analyte. This chapter also presents the first result on multi-analytes' measurement as well as a direct comparison with conventional analytical techniques.

In addition to the above, this chapter also addresses the results of data processing in which it is ascertained whether the data collected via the system would be affected by the influence of the photobleaching.

5.2 Analyte recognition overview

Analyte recognition is based on a binding inhibition assay (Figure 5.1). Prior to the

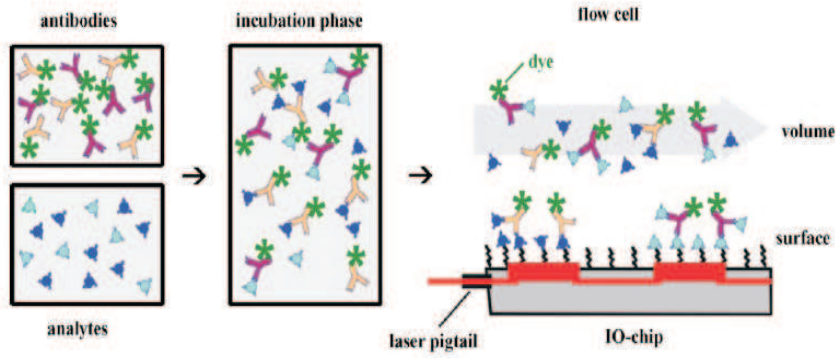

FIGURE 5.1: Schematic diagram of binding inhibition assay.

assay, analyte derivatives are first immobilised onto the transducer surface, analyte-specific antibodies labelled with fluorescent markers are then incubated with the analyte samples. After a short incubation period, the analyte solution is made to flow over the transducer, during which process analyte-specific antibodies with free binding sites will bind to the transducer surface whereas those having one analyte molecule bound to each epitope will not bind to the surface. The surface-bound labelled antibodies are excited in the evanescent field and the fluorescence is detected. As a result, an inverse analyte signal is measured, with samples having low analyte concentrations giving rise to high fluorescence signals and samples with high analyte concentrations resulting in low fluorescence.

For the binding inhibition assay to be quantitative, the binding of the antibody to the surface must be mass transport-limited. This allows the signal to be a function of the diffusion rate to the surface and not of the kinetics of the surface binding. The number of higher affinity binding sites on the surface has to be much higher than the number of antibodies used for one measurement. In order to make sure that the binding is mass transport-limited, there was a huge excess of antigen derivatives immobilised on the sensor surface while only small amounts of antibodies were applied. This was confirmed by additional reflectometric interference spectroscopy (RIfS) measurements as described in (76).

5.3 Surface modification

This multisensor platform may be applied to a wide range of analytes according to the surface attachment protocol. In this case, characterisation of chip and instrument performance for immunofluorescence sensing was carried out with a single analyte, estrone, to allow direct patch-to-patch comparisons. The surface modification and the immunoassay experiments described in the next section were undertaken by the author jointly with Günther Proll, at the Tübingen University, in Germany. The entire sensor surface was chemically modified in order to render the chip specific to estrone, to reduce non-specific binding and to enable repeated use. The chip was cleaned in a freshly prepared mixture (ratio 2:3) of hydrogen peroxide (30% H_2O_2) and concentrated sulphuric acid (65% H_2SO_4) for approximately 10 minutes and rinsed with Milli-Q water. After drying under a nitrogen flow, a few drops of [3-(2, 3-Epoxypropoxy)propyl]trimethoxysilane were applied to the sensor surface, and the surface was covered with a microscope slide for 1 hour. The silanised surface was rinsed with dry acetone and blown dry at room temperature, and then the aminodextran was coupled to the silanised surface (33). Since the silane has an epoxy terminal which reacts directly with amine groups on the aminodextran, so when glass surface is silanated, the epoxy group is introduced and remains active till the dextran is added. Epoxy groups react with amines and for covalent bonds. The sensor surface was then immersed in the analyte derivative estrone carbonate acid dissolved in N-Dimethylformamide (DMF) together with N, N'-Dicyclohexylcarbodiimide (DCC). This procedure leads to a high surface density (4) of binding sites specific to estrone antibodies. Non-specific binding is limited due to the shielding of the glass surface by the aminodextran (77).

5.4 Immunoassay trial

The performance of the biosensor was demonstrated by measuring the response to eight known concentrations of the analyte estrone in deionised water, ranging from 0 ng.L^{-1} (blank) to 10 μg.L^{-1}. Then 100 μL of antibody solution, containing 60 ng.mL^{-1} of labelled affinity purified polyclonal anti-estrone antibody in 10-fold phosphate buffered saline (PBS), were added to 900 μL of each standard solution and mixed thoroughly to allow the analyte to bind to the fluorescent-labelled antibody molecules, according to

its concentration. The incubated solution was then pumped over the sensor surface as described below. Those antibodies which have not been bound to analyte molecules are free to bind to the sensor surface. The output of one sensing channel during a sensor test cycle using Cy5.5 labelled anti-estrone and a blank sample, is shown in Figure 5.2, and progressed as follows: a constant flow of PBS was established through the

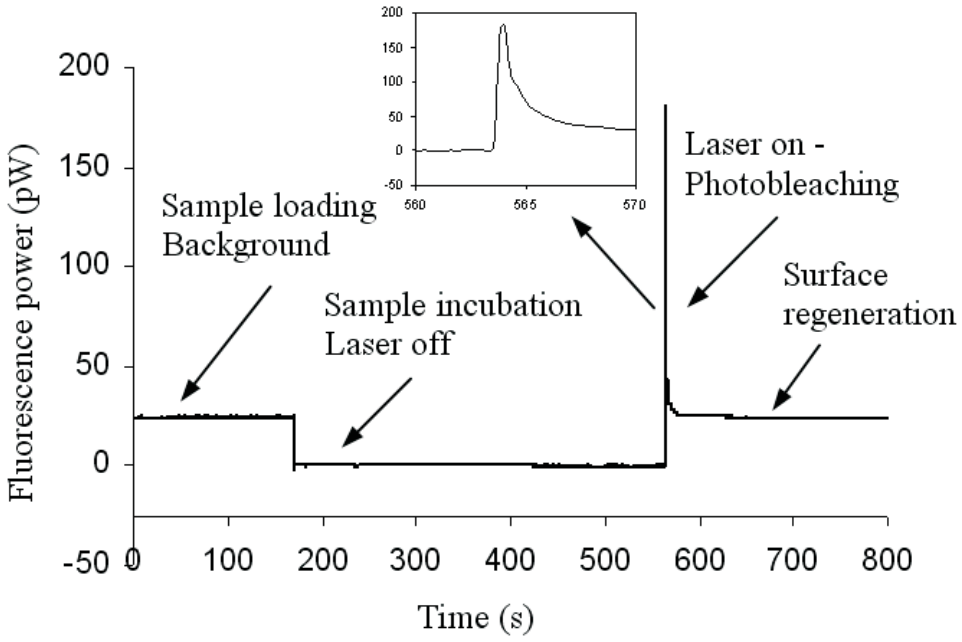

FIGURE 5.2: Sensor test cycle for blank with 6 ng.mL^{-1} anti-estrone.

micro-flow-cell, and the background signal, due to laser breakthrough and background fluorescence, was measured. While the incubated sample was being loaded and injected into the flow-cell, the laser was turned off to prevent the onset of photobleaching. After binding of the incubated sample at the sensor surface for ∼6 minutes, the cell was flushed with PBS again and the laser turned on, allowing fluorescence from the Cy5.5 dye to be detected. Figure 5.2 shows that, once the background has been subtracted, a peak signal of ∼155pW was obtained and that this was bleached in a few seconds. Nonetheless, there is no difficulty in acquiring this signal, and the signal to noise ratio is of order 1000. After bleaching, the surface was regenerated by 0.5% sodium dodecyl sulphate (adjusted with HCl to pH 1.8) to break the interaction between the antibodies and analyte derivative and remove the antibodies bound to the surface, so that another measurement could be carried out, with the entire cycle time taking less than 18 minutes.

Figure 5.3 shows a test cycle for zero estrone concentration (blank), using an antibody concentration of 50ng.mL^{-1} on the sensor chip number 13-2. Figure 5.4 shows a close look of the same cycle.

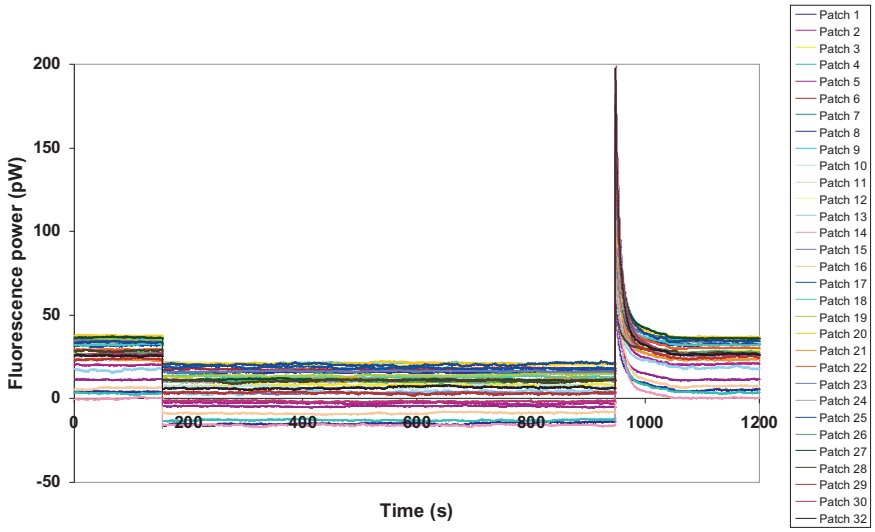

FIGURE 5.3: Test cycle for blank on sample 13-2 (without Ta_2O_5 layer).

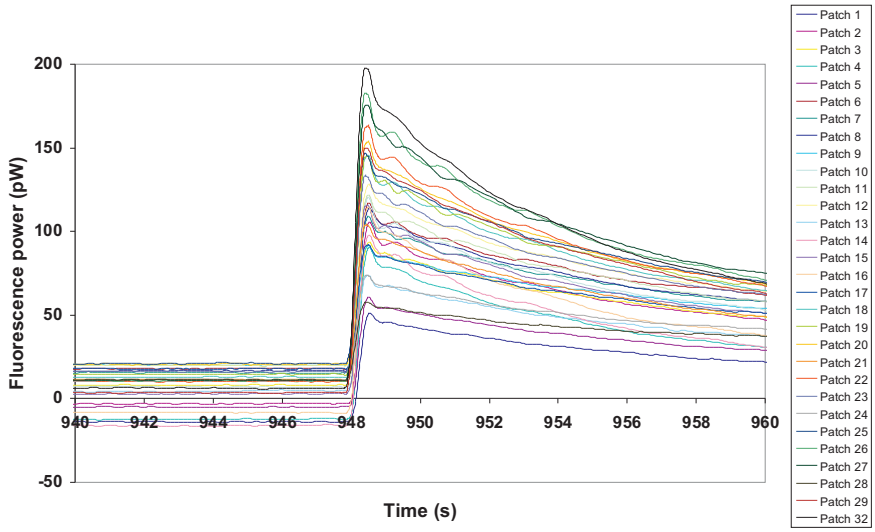

FIGURE 5.4: An expansion of Figure 5.3. Note: two saturated patches were removed from the figure.

Linear correlations have been achieved between the antibody concentration used and the fluorescence power measured in preliminary experiments conducted by Tübingen University (33). The first set of experiment was undertaken using antibody concentrations between 50ng.ml^{-1} and 500ng.ml^{-1}, and showed a linear relationship between the

fluorescence signal to the concentration of antibody. A linear correlation of 20fW fluorescence powerper ng.ml^{-1} of antibody concentration was achieved (78). Subsequently, tests using antibody concentrations from 1ng.ml^{-1} to 50ng.ml^{-1} showed similar linear behaviour. This linear relationship shows that the surface receptors are not becoming saturated even with the highest antibody concentration (1.5μg.ml^{-1}). This verifies that there is a large excess density of antigen derivative immobilised on the surface in comparison with density of antibody binding, so that a linear relationship between the free antibody concentration in solution after incubation with the sample and the fluorescence signal can be expected in water sample assays.

5.5 Data analysis and processing

One of the major features of the present sensor chip was the reduced rate of photobleaching which was achieved by broadening the waveguide, because the sensitivity of the device will be reduced if significant photobleaching of the dye molecules occurs under the high optical intensity. It is necessary to keep the photobleaching rate level sufficiently low, by reducing the optical field power density, so that signals can be collected before they fade away. In order to assess the effect on the photobleaching rate due to the waveguide broadening or the light power in the waveguide, it is desirable to extract the photobleaching rate from the output signal. The detailed data collecting system has been described in Section 3.4.4 Chapter 3. The output signal was filtered and it has the influence of the filter. The question is whether this influence or effect of the filter, the 4^{th} Order Butterworth Low-pass filter in this case, on the signal is noticeable. In this section, a detailed analysis is given on how to recover the raw data from the measured data in order to find out whether the latter is reliable.

5.5.1 Recovering the original signal from the measured data

In this study, the data measured from the instrument has been filtered, and the original input signal is unknown. If the effect of the filter on the signal is unimportant, the measured signal can be treated as the same as the original signal. If the filter's effect is important, or is unclear and yet is potentially important, it will be necessary to recover the original signal by removing the effect of the filter.

In this section, the method used to recover the orignal data from the measured data is discussed.

5.5.1.1 Recovering the original signal using a Fourier transform; theory

Assuming the original input signal is $x_i(t)$, the filter has a time response function h(t), or transfer function $H(\omega)$, and the measured signal, i.e. the output signal, is $x_o(t)$; the output signal can then be expressed as:

$$x_o(t) = h(t)^* x_i(t) \tag{5.1}$$

Where * denoted the convolution integration of the two adjacent functions. The equation in 5.1 can be rewritten in the frequency domain as

$$\begin{aligned} x_o(t) &= F^{-1}[X_o(\omega)] \\ &= F^{-1}[H(\omega)]^* F^{-1}[X_i(\omega)] \\ &= F^{-1}[H(\omega)X_i(\omega)] \end{aligned} \tag{5.2}$$

Which leads to

$\mathrm{X}_o(\omega) = H(\omega)X_i(\omega)$

or

$$X_i(\omega) = X_o(\omega)/H(\omega) \tag{5.3}$$

The original signal $x_i(t)$ can now be obtained by performing an inverse Fourier transform to both sides of equation 5.3

$$\begin{aligned} x_i(t) &= F^{-1}[X_i(\omega)] \\ &= F^{-1}[X_o(\omega)/H(\omega)] \end{aligned} \tag{5.4}$$

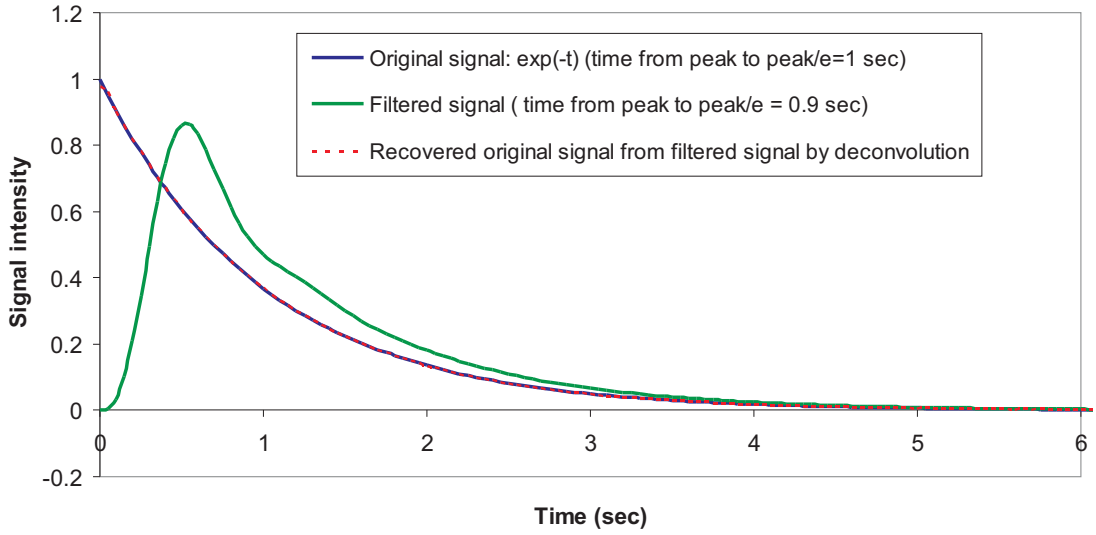

FIGURE 5.5: Effect of AWACSS 4^{th} Order Butterworth Low-pass filter, time step size=0.05 sec

An example is shown in Figure 5.5, in which the original input signal $x_i(t)$=exp(-t); the 4^{th} Order Butterworth Low-pass filter which was used in the AWACSS system has a cut-off frequency of 1.4 Hz. The original signal $x_i(t)$ is obtained by applying an inverse Fourier transform to the measured signal which is the filtered in this case over the transfer function of the 4^{th} Order Butterworth Low-pass filter in the frequency domain. It can be seen that the original signal is fully recovered using this method.

5.5.1.2 Application to photobleaching data - post-processing

The main objective of this effort to recover the original signal is to exclude the distortion from the measured data caused by the filter, so that the decay rate of the original signal can be more accurately calculated.

There are three steps involved in determining the decay rate of the original signal. The first step is to remove the background noise. The second step is to de-convolute the measured signal using a Fourier transform to recover the original signal and the last step is to determine the decay rate using a curve fitting method. The decay rate of the signal is measured by the time it takes to decay from peak value to peak value divided by e.

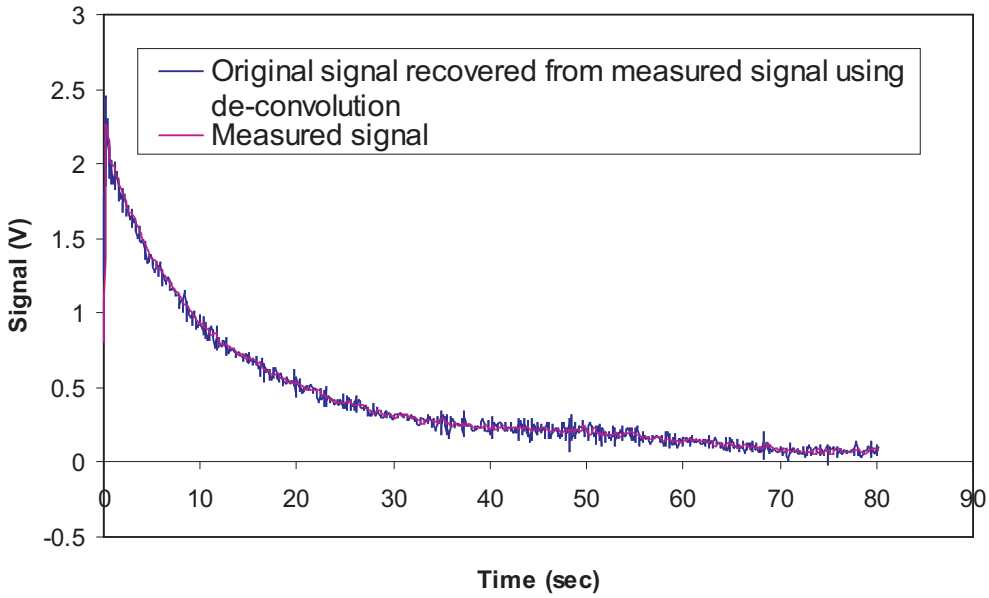

FIGURE 5.6: Measured signal and recovered original signal (channel 1)

Figure 5.6 shows an example of the original signal recovered from the measured signal using the de-convolution method. Note that the sampling rate needs to be at least twice as high as the frequency of the signal being sampled.

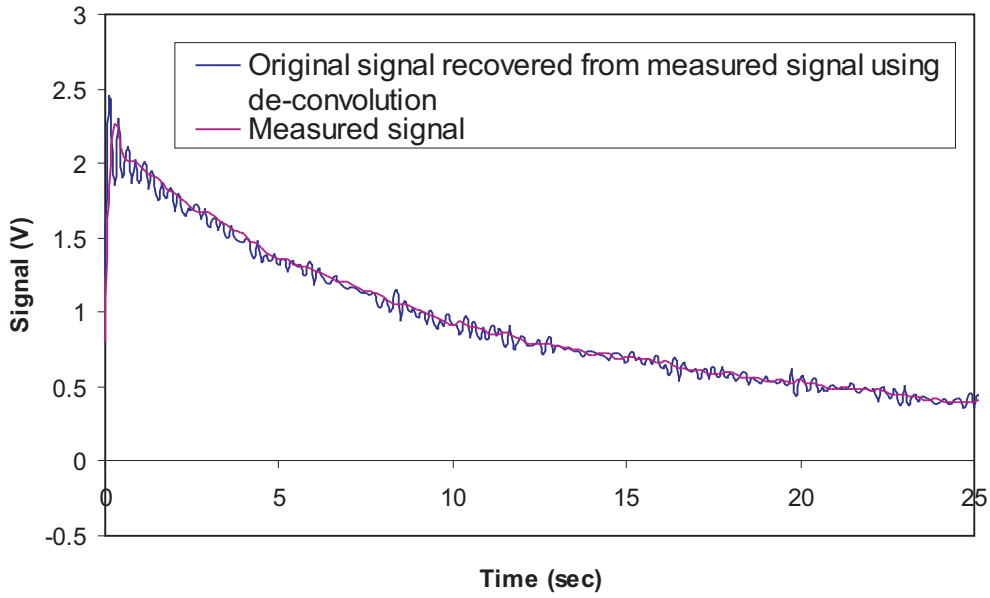

FIGURE 5.7: An expansion of the Figure 5.6.

5.5.1.3 Discussion

From Figure 5.7, one can observe that:

- The two curves have very similar mean values, but the recovered signal contains high frequency noise which has been filtered out in the measured date
- No obvious phase shift is observed in the measured signal near the peak
- Effect of the filter is negligible
- The peak value is always very close to the start of time (when the laser is switched on) and the data tends to be oscillatory, so the peak value obtained from the oscillating region may not be very reliable

It was therefore decided to perform a least square curve fitting to determine the decay rate. The decay rate of the measured signal can be assumed to be the same as that of the original signal.

5.5.1.4 Curve fitting and photobleaching rate extraction

An exponential function is chosen to fit both the measured signal and the recovered signal. The fitting curve is expressed as (excluding the base value):

$$S(\mathrm{t})=\mathrm{A}e^{-ct}$$

The decay rate is decided by the time it takes for the signal to reduce from its peak value A (at t=0) to A/e. If this length of time is denoted by T_d, then the decay rate of the fitting curve can be calculated by:

$$Ae^{-cT_d} = A/e$$

or

$$T_d = 1/c \tag{5.5}$$

By comparing the fitting curve with the measured data, it can be seen that, although the two agree very well in general, the sharp peak in the measured data at t=0 is not

well matched by the fitting curve. This difference is expected to reduce the decay rate, or increase the value of T_d, derived on the basis of the fitting curve.

In order to take the sharp peak in the measured data into account in the decay rate calculation, a modification needs to be made to the expression in equation 5.5.

Assuming the peak value of the measured data (at t=0) is A_m, then the time T_d on the fitting curve should be decided by

$$Ae^{-cT_d} = \mathrm{A}_m/e$$

i.e.

$$T_d = [1 - ln(A_m/A)]/c \tag{5.6}$$

It can be seen that if the measured data has a higher peak value than the fitting curve, i.e., $A_m/A>1$, then $\ln(A_m/A)>0$, then the value of T_d from equation 5.6 will be smaller than that from equation 5.5, i.e. the decay rate is higher (about 10% in the cases tested) with this modification.

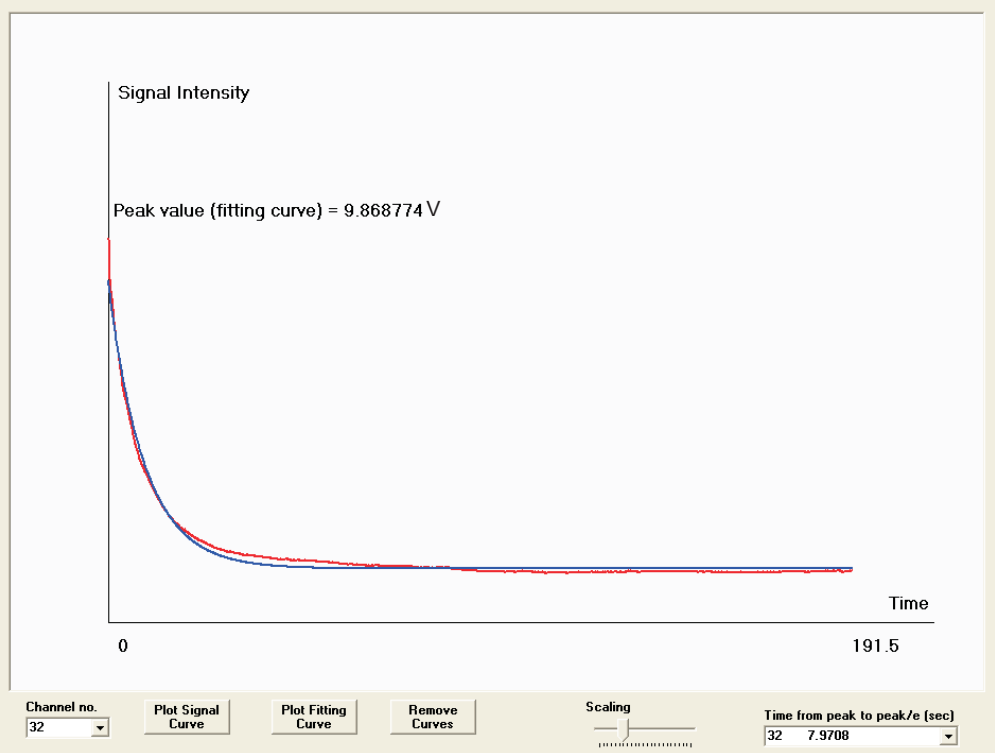

FIGURE 5.8: Sample of curve fitting of measured signal 1.

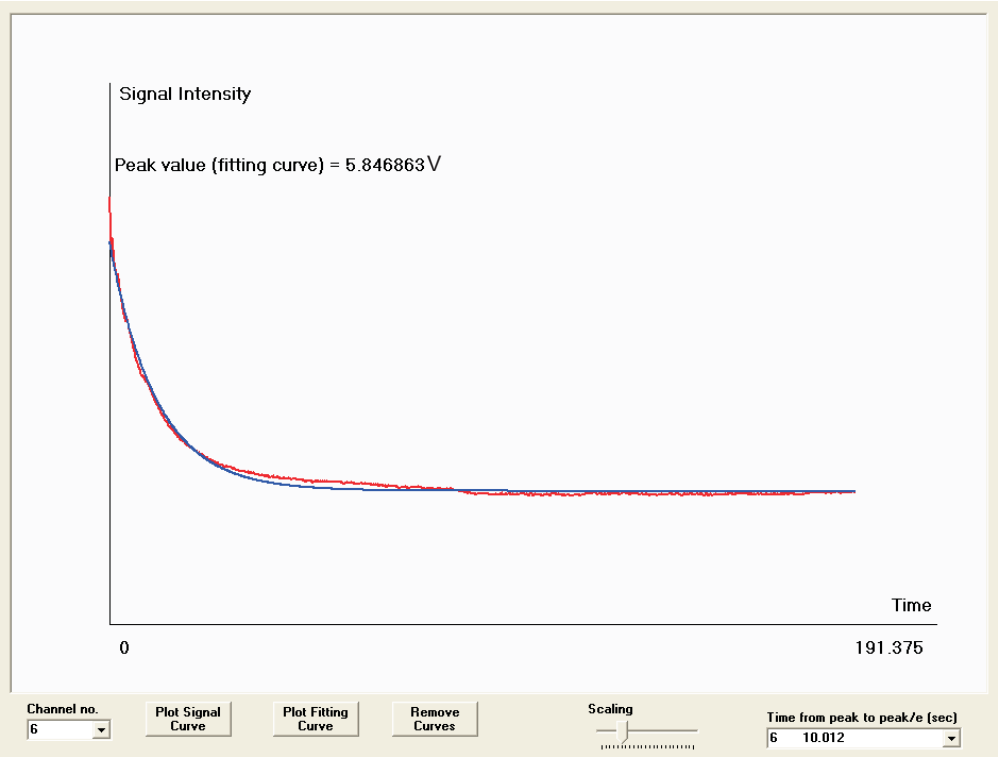

FIGURE 5.9: Sample of curve fitting of measured signal 2.

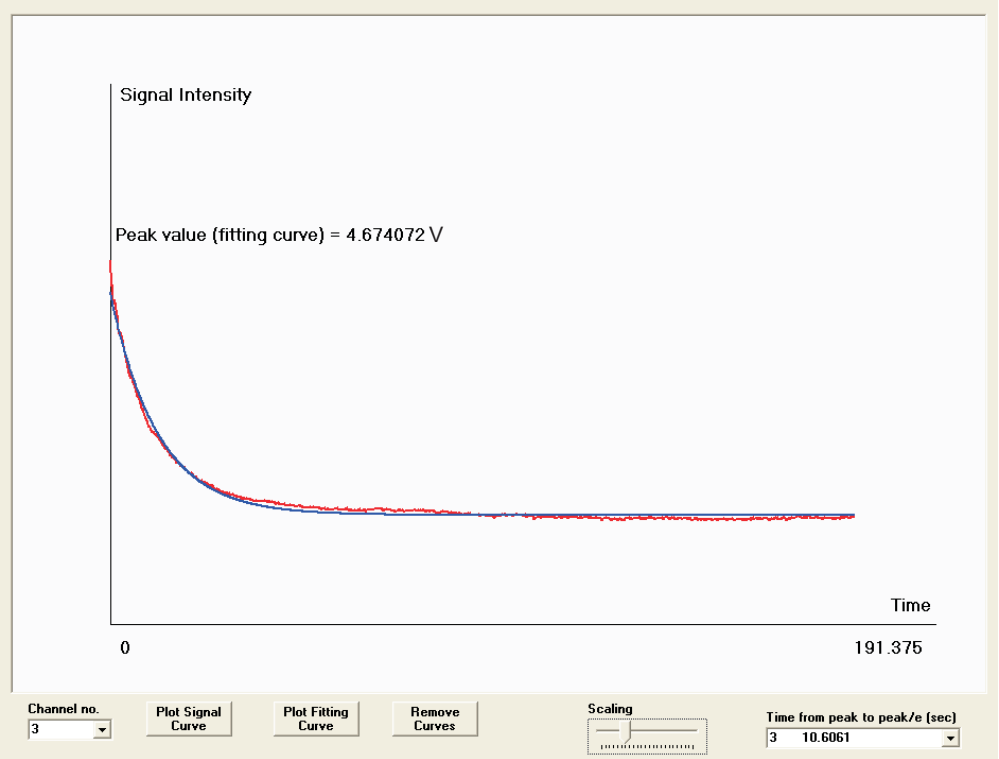

FIGURE 5.10: Sample of curve fitting of measured signal 3.

Figures 5.8, 5.9 and 5.10 show three curve fitting samples from three different sensor patches on the same sensor chip, the result is listed in Table 5.1. It can been seen that the decay rate or the value of the T_d, can vary and is dependent on the peak value of each sensor patch. We can apply this method to different broadened waveguide sensor chips to map the photobleaching rate, in order to find out the effect of the broadening.

Sensor patch No	Peak signal (V)	Decay rate $T_d(sec)$
32	9.87	7.97
6	5.85	10.01
3	4.67	10.61

TABLE 5.1: Comparison of the decay rate from three curve fitting of three different sensor patches on the same sensor chip. Note that patch No 32 is nearest the waveguide input end, patch No 6 and 3 are near the waveguide output end.

5.6 Estrone calibration curve and limit of detection (LOD)

A calibration curve for normalised fluorescence power against estrone concentration was obtained by repeating the procedure described in Section 5.4 using the 3 ng.mL^{-1} dye-labelled antibodies and water samples containing estrone in a different concentration, prepared as described above. This calibration curve was formed by responses of the measurement results of estrone in the concentration range 0-10ppb (μg.L^{-1}). Subsequently, the curve can be used for detecting an unknown estrone concentration.

The blanks were repeated 9 times to yield a good statistical sample and all other concentrations were repeated three times. The averaged data were fitted to a logistic function as given in equation 5.7 (79),

$$y = \frac{A_1 - A_2}{1 + (\frac{x}{x_\circ})^p} + A_2 \tag{5.7}$$

(parameters of a logistic function: A_1, A_2, $x_\circ$ and p) with three free parameters (A_2, $x_\circ$, and p) were used. A_1, as the upper asymptote was fixed to 100% (relative signal to the mean value of the blanks) and A_2 is the lower asymptote. The range between A_1 and A_2 is the dynamic signal range. The inflection point is given by the variable $x_\circ$ and represents the analyte concentration which corresponds to a decrease of 50% of the dynamic signal range (IC_{50}). The slope of the tangent in this point is given by the parameter p. The function 5.7 represents a close approximation to the shape of a typical

immunoassay curve, and an example is given in Figure 5.11, which shows the estrone calibration curve for one sensing patch normalised to the mean of the signals for the blanks.

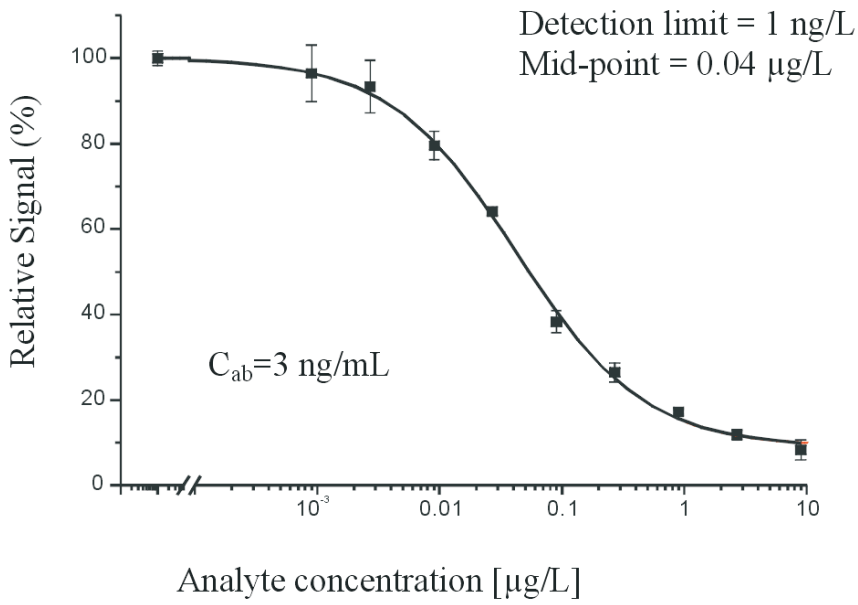

FIGURE 5.11: Averaged calibration curve for estrone. Sample13-2 without Ta_2O_5 layer.

The limit of detection (LOD) was taken to be the concentration in Figure 5.11 at which the signal has fallen below the blank value by three times the standard deviation of the blanks. Approximately 99.7% of all values fall within three standard deviations of the mean for data sets having a normal, Gaussian distribution.

LOD for estrone for this sensing patch was found to be just below 1 ng.L^{-1}, well within an European specification of 0.1 μg.L^{-1}(80), and the test mid-point of the response curve occurred at a concentration of 40 ng.L^{-1}. Concentrations up to 1μg.L^{-1} are measurable and higher concentrations could be measured by diluting the sample. A complete set of test results for all patches during one measurement is shown in Figure 5.4. Clearly the signal strength for each sensor patch is different, due to nonuniformity in the surface intensity of the pump. However, these patch-to-patch differences are constant between measurements and may be normalised in creating the calibration curve for each individual chip. The normalised calibration curves for all 32 patches were found to be similar, as all patches were modified for the same analyte.

Figure 5.12 shows the comparison of the results for the flow in opposite directions. It shows the peak power recorded, with the background subtracted, for all 32 sensing patches for zero estrone concentration (blank) using an antibody concentration of 10ng.mL^{-1}. Patches 29-32 are nearest the waveguide input and patches 1-4 are nearest the waveguide outputs. The red triangle mark shows the signal from each patch with co-directional propagation of light and of liquid flow through the cell, while the blue circle mark shows the flow direction is against the laser transmission direction.

Although there were 12 patches saturated in the former case and only three patches were saturated when the flow direction is reversed, this indicated that there are optical losses along the channels. Saturation can be avoided by further optimisation of the amplifier gain or the antibody concentration. Since the patch-to-patch variations in the peak signal were dominated by the flow direction rather than the losses in the waveguides as shown in Figure 5.12, this direct comparison implies that the dominant factor in patch-to-patch nonuniformity under these conditions is not the delivery of light to each patch, but a flow-related phenomenon such as the reduction in antibody concentration along the flow-cell as antibodies bind to the surface. This phenomenon or the design of the flow cell will not affect the purpose of this project, because each sensor patch on the sensor chip will eventually have different surface chemistry modification and will aim at and attract each different antibody, so the binding reduction effect is negligible.

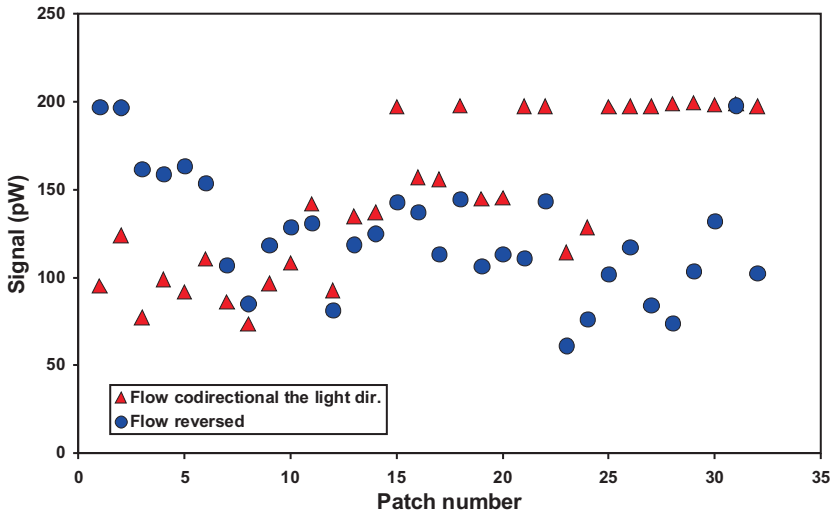

FIGURE 5.12: Comparison of reversing the flow direction. Sample14-2 with Ta_2O_5 layer, at antibody concentration of 10ng.mL^{-1}.

5.7 Multi-analyte measurement

The first multi-analyte test of this sensor was successfully carried out with a mixture of six analytes, atrazine, bisphenol A, estrone, isoproturon, sulphamethizole, and propanil, jointly with six project partners at Tübingen University, in Germany. During the test, the sensor chip was first modified with the derivatives of the above six analytes, in accordance with the previously described immobilisation protocol, by a parallel spotting device TopSpot from HSGIMIT, Villingen-Schwenningen, Germany. The sample containing six analytes was then incubated in a solution with the fluorophore labelled six specific antibodies (anti-atrazine, anti-bisphenol A, anti-estrone, anti-isoproturon, anti-mixed sulphonamides, and anti-propanil). For instance, 100μL antibodies stock solution was mixed with a 900μL sample by an autosampler and incubated for approximately 6 minutes. A simultaneous calibration could be performed with mixed analytes and an antibody stock solution from 0 to 90 μg.L^{-1} analyte concentration in Milli-Q water containing the six corresponding polyclonal antibodies.

The resulting set of calibration curves is shown in Figure 5.13. For all compounds, the calculated LOD is below 0.020 μg.L^{-1} and all validation parameters, calculated relative signals, and standard deviations, are summarised in the Table 5.2 below.

Conc. (μg.L^{-1})	Propanil	Atrazine	Isoproturon	Sulphamethizole	Bisphenol A	Estrone
0	100.0±1.91	100.0±2.37	100.0±2.04	100.0±2.79	100.0±0.93	100.0±0.56
0.009	96.43±2.02	92.15±2.19	96.45±0.83	95.55±2.23	98.01±2.33	95.59±2.04
0.027	92.87±3.38	89.66±3.27	92.05±3.96	90.49±2.24	95.84±0.87	91.62±2.48
0.09	75.69±1.83	71.96±3.49	70.47±3.48	80.13±1.80	86.75±2.27	56.93±2.48
0.27	49.85±1.77	54.96±3.69	40.62±2.23	70.13±1.32	81.76±2.22	32.34±1.58
0.9	26.95±1.35	41.15±1.53	18.24±0.57	58.67±0.10	70.34±2.55	21.69±0.41
2.7	17.44±0.36	32.78±1.86	12.52±0.27	52.73±1.06	58.67±1.54	18.65±0.46
9	12.41±0.61	27.41±0.98	9.85±0.26	45.70±1.14	49.31±2.25	16.53±1.00
27	9.39±0.81	22.58±0.91	8.24±0.51	39.59±0.88	40.25±1.39	15.64±1.56
90	7.87±0.68	19.15±0.63	7.10±0.24	33.91±0.92	34.22±1.64	14.63±0.23
A_1(%)	100	100	100	100	100	100
A_2(%)	9.34±0.87	20.66±1.65	8.39±0.52	32.88±2.41	28.10±2.45	16.72±1.05
x_0(μg.L^{-1})	0.23±0.01	0.22±0.02	0.17±0.01	0.47±0.10	1.70±0.29	0.09±0.01
p	1.05±0.04	0.74±0.05	1.23±0.04	0.57±0.05	0.58±0.04	1.46±0.12
LOD	0.019	0.010	0.020	0.018	0.008	0.007

TABLE 5.2: Resulting parameters (with standard deviations) for the determined logistic fit functions and the validation parameter LOD for all analytes.

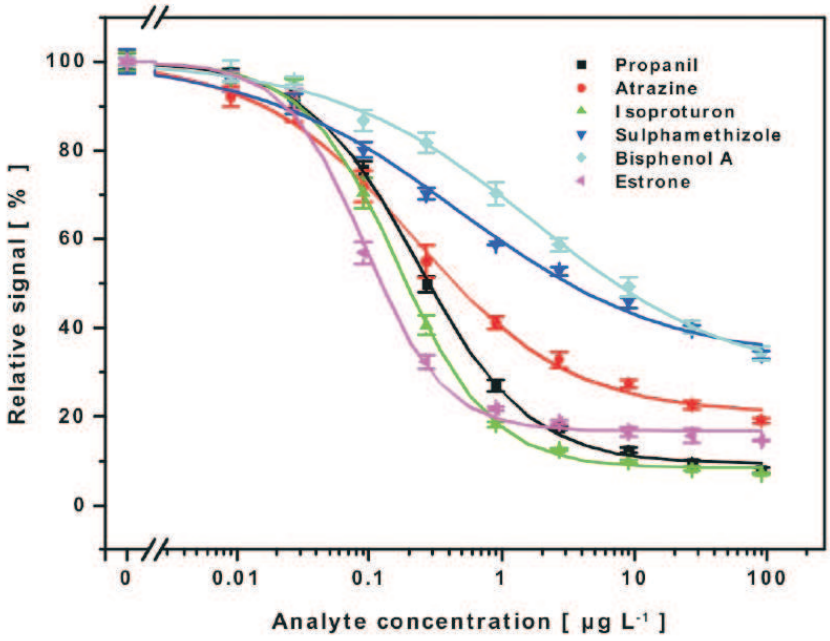

FIGURE 5.13: The resulting set of calibration curves for atrazine, bisphenol A, estrone, isoproturon, sulphamethizole, and propanil, which were measured in parallel on a multi-analyte transducer.

Table 5.2 presents calculated relative signal values with standard deviations for all six analytes at each concentration step from 0 to 90 μg.L^{-1}, and it also shows the calculated detection limit using the logistic function equation 5.7 (79) for all six analytes which are all below 0.020 μg.L^{-1}.

This multi-analyte calibration demonstrated the possibility to quantify pesticides from three different classes (triazines, phenylurea herbicides and anilides), endocrine disrupting compounds (bisphenol A), steroid hormones (estrone), and pharmaceuticals (sulphamethizole) within one single measurement cycle, which only takes approximately 18 minutes.

Tests were undertaken by the project partner in IIQAB, Department of Environmental Chemistry, CID-CSIC, Barcelona, Spain to quantify non cross-reactivity of each antibody. These tests were carried out with three different antibodies directed against the three different analytes. Three antibodies were tested together, but only one of the analytes' concentrations was varied, and it was reported that no mesureable cross-reactivity was observed (81). The final experiment was then set up in which all analytes were varied and calibration curves were established for all three analytes simultaneously (27 concentration combinations). This final experiment was performed successfully, which

confirmed that the multianalyte experiments could be run with little cross-reactivity, meaning that all patches were bound only with one specific antibody, or, there were no other antibodies captured on the same patch.

It was found that the silica isolation layer of the sensor chip was deteriorated beyond repair after 400 to 500 measurements. This deterioration was caused by the gradual erosion of the layer by 0.5% sodium dodecyl sulphate (adjusted with HCl to pH 1.8) solution, which was used in the regeneration process to remove the remaining antibodies bound to the sensor surface and to prepare the system ready for the next measurement.

5.8 Comparison to conventional analytical techniques

The overall performance of the AWACSS system in comparison to the conventional analytical and immunosensor techniques was tested in the inter-laboratory collaborative trial among the project partners. In total, eleven different analytical set-ups were used in six laboratories, among them four automated on-line SPE-LC-DAD UV system (82), on-line SPE-LC-FLD, on-line SPE-LC-MS (83), off-line SPE/LVI-GC-MS (84), two RIANA prototypes (85; 86), ELISA and AWACSS. The tested matrices were Milli-Q water and freeze dried 63μm fractions of river sediments from the Nitra River, for which the special sample preparation protocol was involved. Each of them was spiked with three analytes:(i) atrazine as a representative of pesticide class, being also on the list of WFD Priority Substances; (ii)bisphenol A-industrial pollutant known as an endocrine disrupting compound; and (iii) estrone-hormone with endocrine disrupting effects, often present in outlets of municipal waste water treatment plants. Spiking levels were 0.1 and 1 μg.L^{-1} in water matrices and 50 to 500 ng.g^{-1} in sediment. Water samples were directly loaded onto small 10.0mm X 2.0mm cartridges, which fitted into the automated sample preparation device available in all partner's laboratories. Sediment samples were first extracted by ultrasonic extraction into acetonitrile, the extract was diluted in Milli-Q water and concentrated on the same cartridges. Each sample has been prepared in triplicate and sets of cartridges, including blanks, were distributed among the partners.

The outcome of the tests showed that, in terms of accuracy, AWACSS performance in Milli-Q water and sediment samples is fully compatable with conventional chromatography-based techniques. Table 5.3 shows the results obtained by the AWACSS system within

Compound	Assigned value (μg.L^{-1})^a	Milli-Q water matrix			Assigned value (ng.g^{-1})^{a,b}	Sediment matrix		
		Mean (μg.L^{-1})	Mean (%)	CV (%)^c		Mean (ng.g^{-1})	Mean (%)	CV (%)^c
Atrazine								
Level 1	0.095	0.11	116	9.6	45	49.0	109	5.0
Level 2	0.950	1.12	118	8.3	450	384	85	3.6
Bisphenol A								
Level 1	0.097	0.08	82	4.0	44.5	51.7	116	27.8
Level 2	0.974	1.25	128	16.9	445	423	95	7.5
Estrone								
Level 1	0.076	0.08	105	7.0	36	25.4	71	3.2
Level 2	0.763	1.04	136	4.4	360	333	93	10.7

TABLE 5.3: Milli-Q water and sediment samples were spiked at 0.1 and 1.0 μg.L^{-1} (water samples) and 50 and 500 ng.g^{-1} (sediment samples), respectively. a) Corrected for recoveries of analytes on the SPE cartridges and blank measurements. b) Corrected for extraction recoveries from sediments. c) Calculated from three measurements.

Methods	Mean(μg.L^{-1})	CV(%)
Conventional		
SHE-HPLC-DAD UV (Lab 1)	0.11	14.3
SHE-HPLC-DAD UV (Lab 2)	0.14	3.5
SHE-HPLC-DAD UV (Lab 3)	0.07	20.8
Immunochemistry		
RIANA	0.16	24.1
AWACSS	0.11	9.6
ELISA	0.14	3.6

TABLE 5.4: Spiked concentration:0.1μg.L^{-1}; number of measurements=3.

the collaborative trial and Table 5.4 shows the comparison of atrazine determinations in Milli-Q water obtained by conventional liquid chromatography-based analytical techniques, ELISA, the immunosensor RIANA, and the AWACSS instrument. Recoveries of atrazine and bisphenol A ranged from 82 to 126% compared to the assigned values, while those for estrone were between 71 and 136%. In general, the AWACSS results were less biased towards higher values in comparison to ELISA and RIANA immunosensor techniques. An evaluation of the collaborative trial using the Z-score methodology as an expression of deviation of the measured from the assigned value showed that none of the results obtained by AWACSS was excluded from the evaluation. With regards to

the reproducibility, all results by AWACSS have a variation coefficient lower than 17% (Table 5.3), with the only exception of bisphenol A at the lower spiking level in sediment (27.8%). The results were well within the range obtained by both chromatography-based and other immunosensor techniques. The time for a single analytical run was less than 18 minutes and during the system validation more than 70 analyses were performed within a day in a fully automated regime. Detection limits of all tested analytes were in the low nanogram per litre range.

5.9 Conclusion

This chapter described the sensor chip surface chemistry, and the immunoassay experiments. Data analysis and processing were performed in order to verify the effect of the photobleaching against the collected signal data. The system was initially calibrated with the estrone, and then was applied to test up to six organic pollutants, at detection level of $ng.L^{-1}$, without any prior sample pre-concentration nor pre-treatment steps.

The LOD of $1ng.L^{-1}$ is two orders of magnitude better than that required by EU legislation for organic pollutants, and it is expected that improvements in sample handling and signal processing will reduce this further. The ability to regenerate the sensor automatically after an assay, as part of an automated protocol, means that the sensor and system may be left unattended for months, in normal operation, before a chip needs replacing. There is significant potential for further miniaturisation, increased integration, and reduced usage of reagents as the fluorescent signal is obtained from an area of less than $0.05mm^2$ and a volume of less than 20pL.

The overall performance of the AWACSS system, in comparison to the conventional analytical and immunosensor techniques, was tested for the first time. Among the tested matrices were surface, ground, drinking and waste water as well as sediment samples. The results showed that AWACSS is fully comparable to conventional analytical techniques in terms of accuracy, repeatability and reproducibility, while selectivity allowed for trace analysis even in complex matrices such as sediment extracts.

Chapter 6

Multi-Sensor System II: CCD Detection System

6.1 Introduction

The integrated optical fluorescence multi-sensor instrument discussed in this thesis is based on evanescent field technology. System I, which used polymer fibres to collect the fluorescence, as described in chapter 3 and subsequent chapters, has demonstrated that the principle on which the system design was based works successfully. In principle, the system could be extended to measure more than 32 analytes. For example, it could be readily adapted to measure in excess of a hundred analytes. In System I, the photodetector/filter assembly is chosen as the receiver due to its low cost, and as a result, the high cost effectiveness is one of the major features of the system. If System I is to be extended to a multi-analyte system which can measure many more analytes, the cost may become an issue, since each sensor patch will need a optical filter and a photodetector. Therefore, an alternative detecting and receiving system should be considered and investigated.

In this Chapter, an alternative detection system is presented, which is a CCD detector system. Alternative detection system such as microlens arrays (87) or microchannel plates (88) could also be considered, however, the combination of the sensor chip described in this thesis with a CCD detector could offer more, since the CCD system has flexibility in defining the sensing configuration, and low-noise performance. This chapter

addresses various aspects of the instrumentation of the CCD detector system, including the system overview and operation, estimation of the power flow, and Signal to Noise Ratio (SNR) analysis, as well as reporting the result of the fluorescence measurement on bulk dye Cy5.5 and comparing it with the theoretical prediction and the detection limit of the system for Cy5.5.

This work was severely delayed due to a major fire, which took place at the Mountbatten Building in the University of Southampton, at the end of October 2005. The work eventually resumed in later 2007, in temporary laboratories, and the newly fabricated sensor chips were also undertaken in a temporary cleanroom.

6.2 System overview and operation

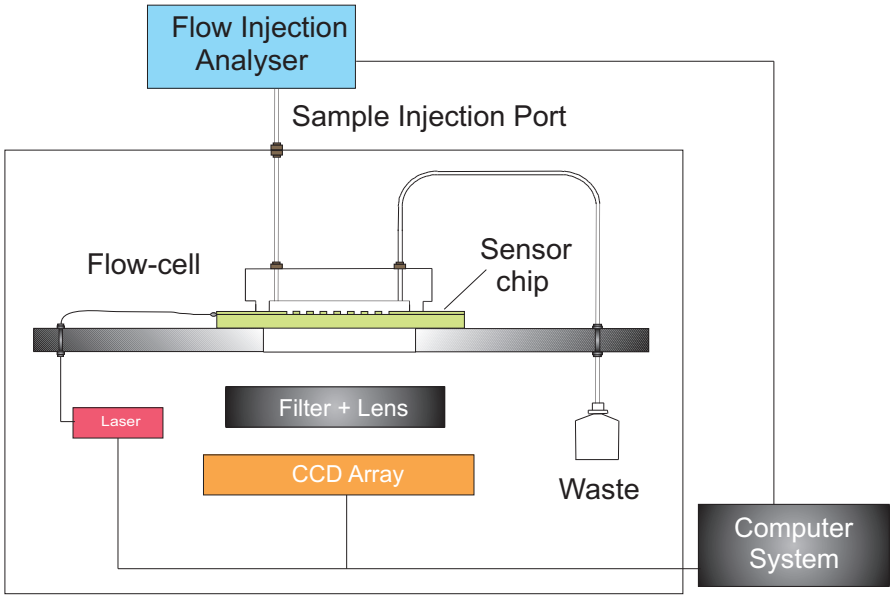

FIGURE 6.1: The multi-sensor CCD detection system.

Figure 6.1 is a schematic diagram of the CCD detection system. The basic principle of the operation is the same as in Chapter 3 Section 3.2, except that the photodetectors, optical filters and electronic filter in System I are replaced by a CCD camera, a single filter and lenses in System II.

There are two principal differences in these systems: (i) the efficiency of fluorescence power collection on the CCD; (ii) the noise performance of the CCD.

6.2.1 The difference between CCD and photodiode detectors

This section will study the types of CCD and address the main difference between CCD and photodiode detectors.

The CCD is a device which uses a quantity of electrical charge to represent an analog quantity, such as light intensity, sampled at discrete times. There are three well known types of CCD in scientific imaging, in terms of two-dimensional or area image scanning format. The first is the interline transfer CCD (ILCCD), the second is the full frame transfer (FFTCCD), and the third is the frame transfer CCD (FTCCD).

Figure 6.2 shows a schematic diagram of the structure of a CCD camera that uses the interline transfer method. The interline CCD (ILCCD) has vertically paired columns consisting of light sensitive arrays as the readout register (also called VCCD). Electrons generated by incoming photons in each light sensitive patch are transferred simultaneously from the patch to the adjacent VCCD register. The VCCD register is covered by a mask of aluminium or other opaque material to prevent photons from creating additional charges in this area. So, only the charges generated in the light sensitive array are included in the readout. Readout is accomplished by transferring each horizontal row of information in the VCCD, line by line, up the CCD to the Horizontal serial register (HCCD). At the HCCD charges are transferred horizontally and converted into charge voltage by an On-Chip-Amplifier (89).

The advantage of ILCCD is that the signal accumulation (exposure) and readout can be done simultaneously because the light sensitive array can accumulate charges for the next frame straight after the previously generated electric charges in the area are shifted to the VCCD. There is no possibility of image smearing in this device and the fastest optical shuttering is achieved.

Figure 6.3 shows a schematic diagram of the structure of FFTCCD and how the mechanism works. In most applications FFTCCD would require a mechanical shutter to cut off the light input, in order to prevent smearing during the time the charges are passing through the parallel VCCD. The pixel charges are transferred, in parallel, to the HCCD where they are then transferred, in series, to the output.

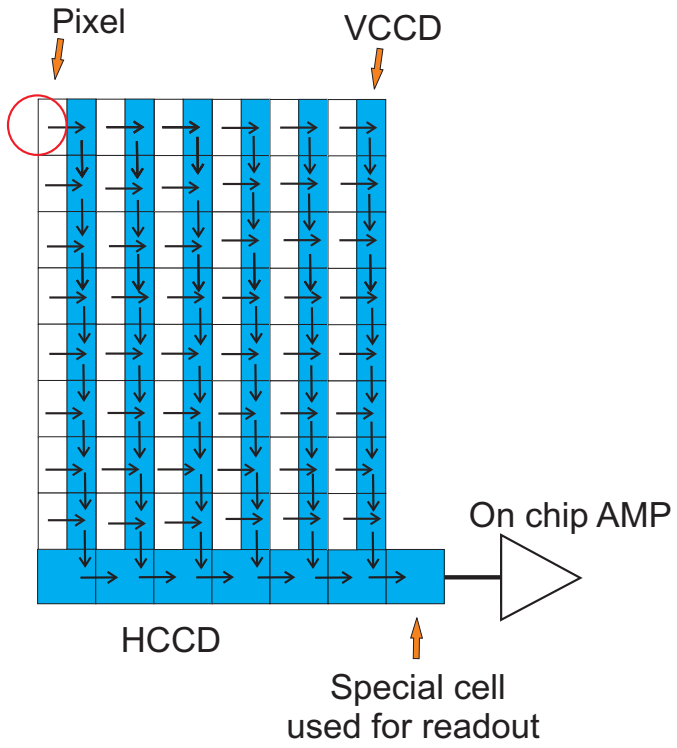

FIGURE 6.2: The interline transfer CCD (ILCCD).

Figure 6.4 shows how the FTCCD works. The image is transferred from the image array to the opaque frame storage array by the bucket-brigade (90) process. This is a relatively fast process, compared to FFTCCD, since the serial register is not used, but it is slower than ILCCD.

The main difference between CCD and a photodiode (PD) detector is the readout scheme of the output signal. In a CCD, the signal (charge) is transferred from one element to the next one down the row until it reaches the end. At the end of the line, the charges, from all the different "picture elements" (pixels), are read in sequence in a time multiplexed fashion, and can then be converted to electrical signals. In a photodiode, the signal (current) is output at the element's unique anode and cathode. Therefore, the signal for the photodiode can be read simultaneously, rather than sequentially and multiplexed.

After exploring all types of CCD, the conclusion is that depending upon the noise performance described in section 6.5, the new CCD to be chosen should be equipped with the ILCCD, since it is the fastest camera compared to the rest.

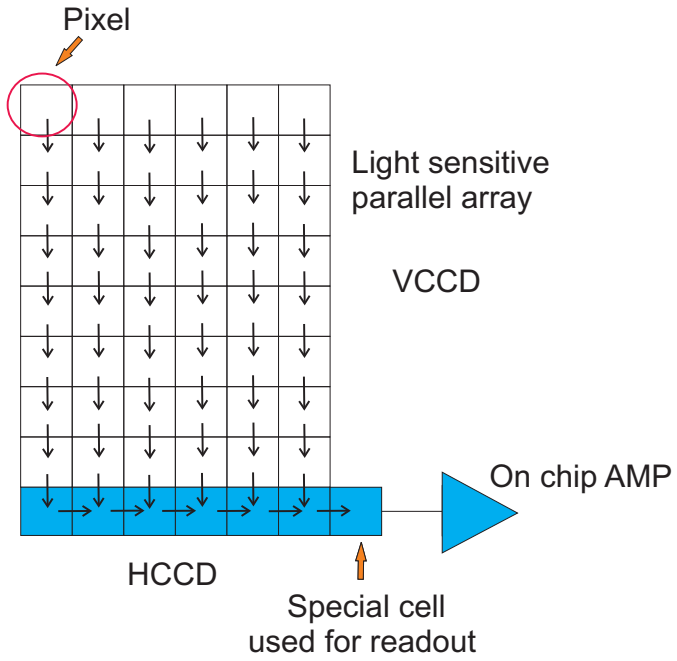

FIGURE 6.3: The full frame transfer CCD (FFTCCD).

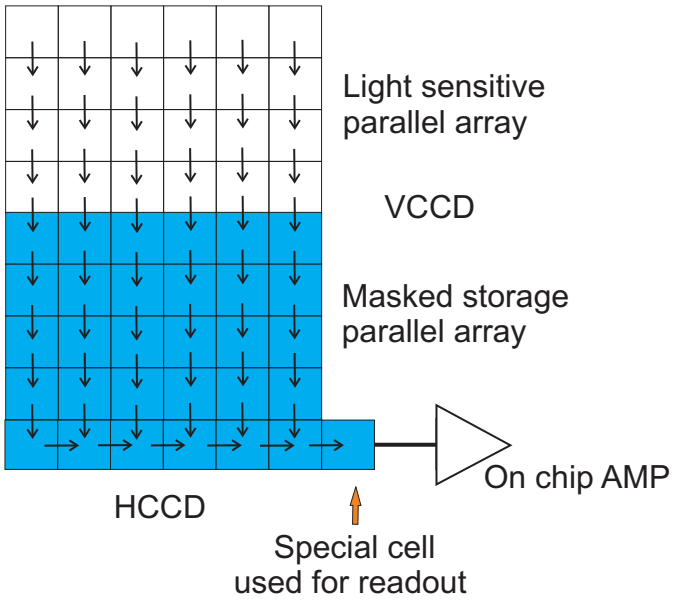

FIGURE 6.4: The frame transfer CCD (FTCCD).

6.3 Collected optical power estimation

Chapter 2 Section 2.7 addressed the power distribution along the optical sensor chip and the amount of fluorescence power reaching the receiving end of the detection system. The fluorescence collection efficiency of System I was given in Chapter 3.

In order to detect a dye concentration of 10^{-8}M which approximately corresponds to the minimum surface coverage required for the system, an emitted fluorescence power of 1pW must be detected with 1mW input pump power with System I, according to the study in previous chapters. In this section, a similar approach is adopted; it addresses the collection efficiency of a CCD detector system and the direct comparison of the collection efficiency with System I.

6.3.1 Collection efficiency of CCD detector system

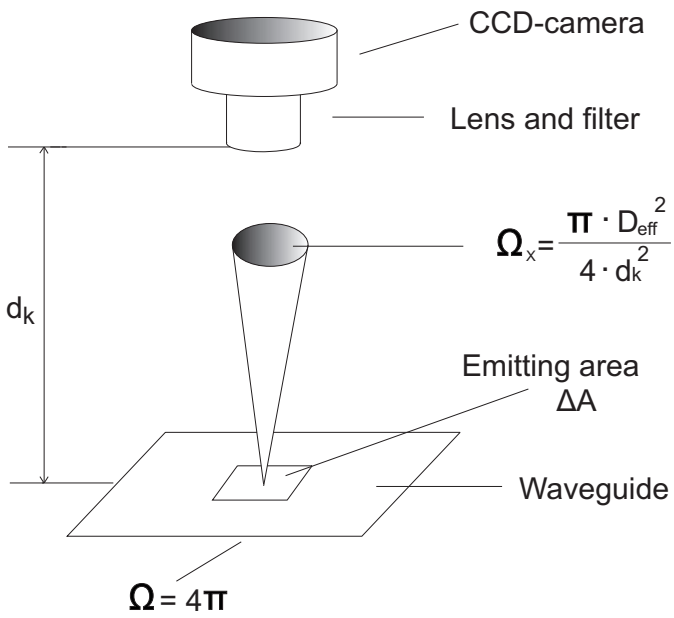

FIGURE 6.5: Fluorescent collection configuration from the sensor chip surface.

This section will study how much emitted fluorescence from the sensor area will be collected by the CCD detector system.

Figure 6.5 shows a sketch of the proposed fluorescent collection configuration. The number of fluorescent photons emitted from the sensor area ΔA radiate into all directions corresponding to the solid conical angle $\Omega = 4\pi$. The emitting area is positioned in the centre of the sphere with radius d_k. Assuming that the fluorescent radiation is isotropic, there are only a small fraction of the generated fluorescent photons striking the camera lens. The effective aperture of lens D_{eff} is given by:

D_{eff}=f/k_b, in which, f is the focal length and k_b is the f-number.

If the lens is positioned a distance d_k away from the emitting surface, then the solid angle of emitted light that is captured by the lens is given by:

$$\Omega_k = \frac{\pi(\frac{D_{eff}}{2})^2}{{d_k}^2} = \frac{\pi f^2}{4{d_k}^2{k_b}^2} \tag{6.1}$$

So that the fraction of light incident upon the lens is $\Omega_k/4\pi$. The number of photons which reach the CCD-sensor chip P_c is given as

$$P_c = T_{lens}T_{filter}(\frac{\Omega_k}{4\pi})P_e \tag{6.2}$$

In which, T_{lens} is the transmission of the lens and T_{filter} is the transmission of the interference filter at the wavelength of the fluorescent radiation.

Therefore, the CCD system collection efficiency η_{ccd}, which is the ratio of the collected fluorescent power to the emitted fluorescent power, can be expressed as:

$$\eta_{ccd} = T_{lens}T_{filter}\frac{f^2}{16{d_k}^2{k_b}^2} \tag{6.3}$$

A CCTV-lens (f = 16mm/k_b = 1.4 from Pantax Machine Vision C1614-M(C31634)) was chosen to collect sufficient fluorescent light. The transmission of the lens in the visible spectrum is $T_{lens} = 0.83$. The filter used in the set up is the same one in System I in order to make direct comparison of two systems, and has a transmission of 20% for the fluorescent emission of the dye Cy5.5.

Using equation 6.3, the collection efficiency of the CCD detector system η_{ccd} is 0.22%.

6.3.2 Collection efficiency for both System I and II

Table 6.1 shows the direct comparison of the fluorescence collection efficiency for both System I and System II. The collection efficiency of the CCD system is predicted to be three times better than that of the fibre collection System I.

In order to determine full system performance, the noise behaviour must now be studied.

	Fibre%	Lens%
Fibre/lens collection efficiency	3.67	1.31
Fibre/lens transmission	92	83
Filter transmission	20	20
Detector/CCD collection efficiency	11	100
Total emmision/collection efficiency	0.08	0.22

TABLE 6.1: Direct comparison of fluorescence collection efficiency for both System I and II.

6.4 Signal to Noise Ratio (SNR) analysis

This section will study the noise performance of CCD cameras, which leads to the identification of a suitable CCD for the detector system.

SNR is an important parameter of a CCD camera which describes the camera's detection capability. It refers to the relative magnitude of the signal compared to the uncertainty in that signal on a per pixel basis. In this research, SNR is also considered on a "regions of interest" (ROI) basis or a super-pixel basis for a CCD detector system.

Photons incident on the CCD convert to photoelectrons within the silicon. These photoelectrons comprise the signal but also carry a statistical variation of fluctuations in the photon arrival rate at a given point. This phenomenon is known as "photon noise" or shot noise and follows Poisson statistics (91). In addition, inherent CCD noise sources create electrons that are indistinguishable from the photoelectrons. When calculating overall SNR, all noise sources need to be taken into consideration.

The SNR in a CCD camera is given by the ratio of generated charge carriers (signal electrons) to the number of unwanted charge carriers (noise electrons):

$$SNR = \frac{N_{signal}}{N_{noise}} \tag{6.4}$$

In which the light signal N_{signal} is the number of signal electrons which depends on the illumination intensity of the incoming photons described as:

$$N_{signal} = \Phi \eta_{qe} t \tag{6.5}$$

Where Φ is the incident photon flux (pixel^{-1}. second^{-1}), η_{qe} is the quantum efficiency of the CCD, t is exposure time (s).

Photon noise refers to the inherent natural variation of the incident photon flux. Photolectrons collected by a CCD have a square root relationship between signal and noise.

So the total noise signal from photon or shot noise is

$$n_{photon} = \sqrt{N_{signal}} = \sqrt{\Phi \eta_{qe} t} \tag{6.6}$$

The other noise contributions from a CCD camera are readout noise and dark current.

The readout noise caused by the on-chip floating diffusion amplifier (FDA) that converts accumulated charges into voltage, is the most dominant factor influencing the detection limit of a CCD, and it is the square-root of readout noise squared.

The dark current has two elements, one is due to clock induced charge and the other is thermal charge. Clock induced charge is the charge generated when electric potential is changed in order to transfer charge. Normally, it is negligible as it is less than 1 electron compared to the readout noise which is several electrons or more. Since a CCD is made from silicon the dark current is caused by thermal migration of electrons in the silicon. This migration is known as dark current and can be an important noise factor for a CCD sensor. Dark current or dark noise, which also follows a Poisson relationship, is the square root of the number of thermal electrons generated within a given exposure.

Cooling the CCD from room temperature to -25°C will reduce dark current by more than 100 times (37).

Since all noise sources are not correlated, taken together the signal electrons and the total number of noise electrons, the SNR for a CCD camera can be calculated from the following equation (92):

$$SNR = \frac{N_{signal}}{N_{noise}} = \frac{\Phi \eta_{qe} t}{\sqrt{(\sqrt{\Phi \eta_{qe} t})^2 + \sqrt{n_d}^2 t + {n_r}^2}} \tag{6.7}$$

In which, n_d (electrons pixel^{-1}. second^{-1}) is dark current and n_r (electrons) is readout noise.

Hence, to achieve a good SNR, high quantum efficiency, small CCD dark current or dark noise and small readout noise are all desirable.

Using binning can improve the SNR of a CCD camera. Figure 6.6 shows the principle of binning. By summing signals of adjacent pixels in a CCD, the binning readout method delivers high sensitivity, improved signal to noise and increased frame rate as a tradeoff for resolution. The resolution is not an issue in this study, since the focus is on collection of emitted light rather than fine or detailed images. As an example, in 2x2 binning, the electrical charge of 4 pixels is summed in the CCD to increase the signal component 4-fold, but the readout noise is still only equal to one readout period so the SNR is improved.

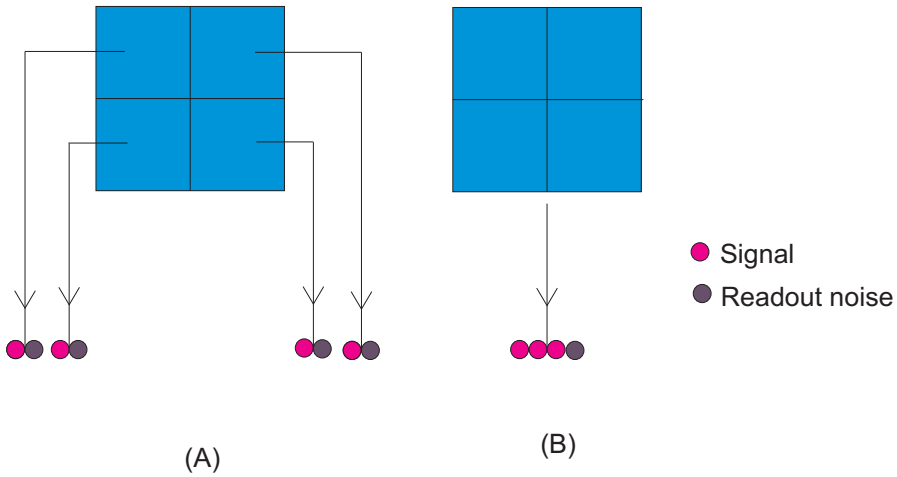

FIGURE 6.6: Principle of binning. (A) Normal readout of 4 pixels. (B) 2x2 binning readout. In which, readout noise is still only equal to 1 readout period per 4 pixels' signal readout.

Taking the effect of binning into account, equation 6.7 should be modified as below:

$$SNR = \frac{M\Phi\eta_{qe}t}{\sqrt{M\Phi\eta_{qe}t + Mn_dt + {n_r}^2}} \tag{6.8}$$

In which, M represents the number of binned pixels, and it is assumed that the signal in each of those pixels is the same.

6.5 Selection of the CCD camera

This section will investigate a number of CCD cameras based on the above analysis. In order to achieve a good SNR, high quantum efficiency, small CCD dark noise and small readout noise are essential. Table 6.2 lists a number of CCDs and some of their specifications. Figure 6.7 shows a plot of SNR vs exposure time based on all CCDs listed in the table, using the equation 6.7, in which, assuming Φ, the incident photons falling on each pixel per second, is 500(pixel^{-1}. second^{-1}), which is equivalent to the 10^{-8}M Cy5.5 fluorescence power collected from a sensor spot of 30 μm x 1.5 mm in practice. Figure 6.8 shows an expanded view of the SNR for the listed CCDs with exposure times from 0.1s to 1s.

	Quantum efficiency (%,@700nm)	Dark noise ($e^-.pixel^{-1}.s^{-1}$)	Readout noise (r.m.s.,e^-)	Frame rate (no binning, frames.s^{-1})
Hamamatsu ORCA-R^2	50	0.005	6	8.5
Hamamatsu ORCA-285	27	0.8	8	8.8
Q-Imagin RETIGA-SRV	45	0.05	8	11
PCO Sensicam qe	40	0.1	6	10

TABLE 6.2: List of CCD cameras and some of their specifications.

Having compared the listed CCDs, the digital CCD camera $ORCA-R^2$ from Hamamatsu was chosen for the CCD detector system. The ILCCD is used in the $ORCA-R^2$. It has better SNR and it is also cooled to -35°C with air cooling (it could reach -40°C with water cooling). The CCD chip contains a 8.66mm x 6.66mm effective area (1344 x 1024 pixels), the dimensions of a pixel is 6.45μm x 6.45μm. The quantum efficiency of the CCD, as shown in table 6.2, is 50% at the emission wavelength λ = 700nm. The pixel quantum wells have a full well capacity of 18,000 electrons (with the high dynamic range mode off) and 36,000 electrons (with the high dynamic range mode on). The maximum digital signal for the 12-bit A/D converter is 2^{12} = 4,096, so the analog-to-digital-conversion factor is ν = (18,000/4096) = 4.4 electrons/ADcounts. The

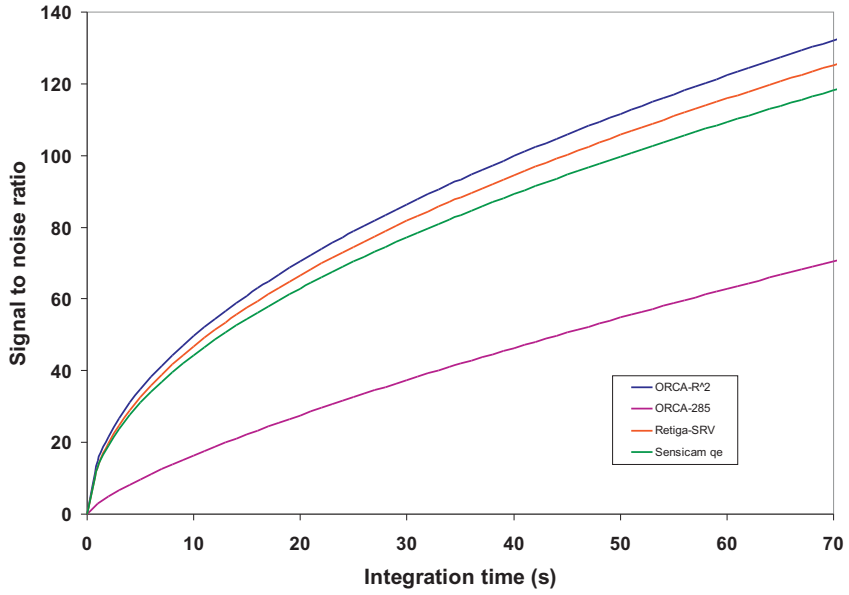

FIGURE 6.7: Signal to Noise Ratio for the listed CCDs in table 6.2, assuming the photons' flux is 500 pixel^{-1}. second^{-1}, which is equivalent to the 10^{-8}M Cy5.5 fluorescence power collected from a sensor spot of 30 μm x 1.5 mm in practice.

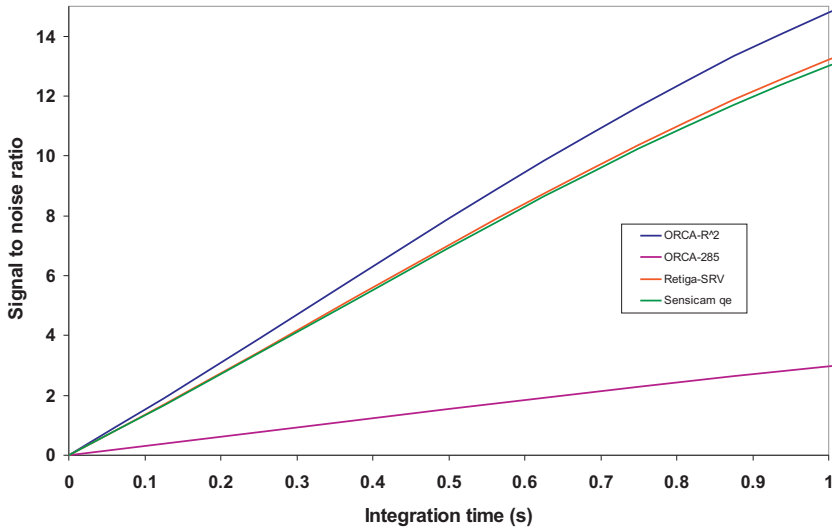

FIGURE 6.8: An expansion of the Signal to Noise Ratio shown in Figure 6.7.

maximum digital signal for the 16-bit A/D converter is 2^{16} = 65,536, so the analog-to-digital-conversion factor is ν = (18,000/65,536) = 0.275 electrons/ADcounts. The integration time of the camera t_{Int} can be set from 10μs up to 4200s.

One of reasons for choosing $ORCA-R^2$ is due to its high dynamic range feature in the normal scan mode. High dynamic range takes advantage of the larger full well capacity of the horizontal transfer register pixels, in comparison with the full well capacity of

each imaging pixel. It is enabled in 2 x 2, 4 x 4 and 8 x 8 binning modes where the charges in the imaging pixels are summed in the horizontal transfer pixels. This feature is only available in normal scan mode since normal scan mode is able to transfer these larger charges accurately. For example, the standard dynamic range for the CCD is 3000 (full well capacity/readout noise):1 at full spatial resolution in normal scan mode. This is higher than most comparable cameras. The high dynamic range mode is 6000:1 and this mode offers an increased full well capacity of 36,000 electrons when binning.

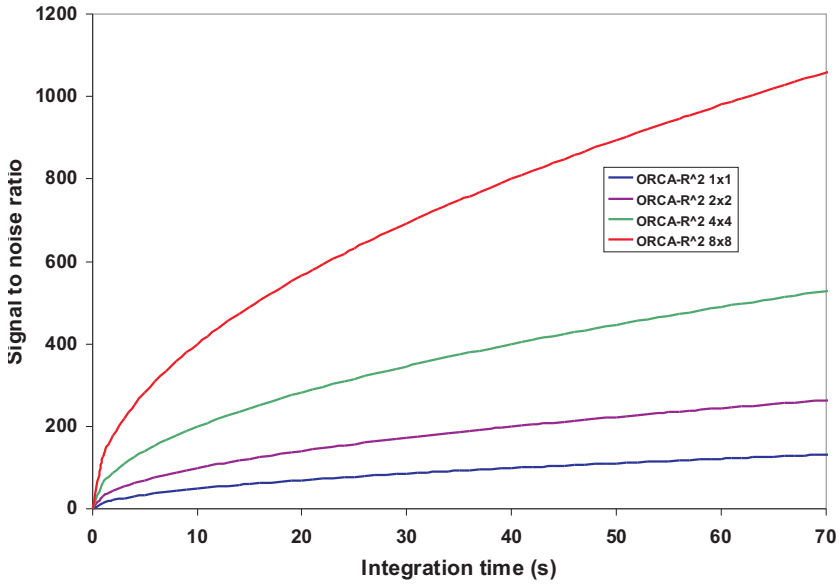

FIGURE 6.9: Signal to noise improvement with binning. Assuming the photon flux is 500 pixel^{-1}. second^{-1}.

Figure 6.9 shows the effect of different binning values on curves plotting the variation of SNR of the selected $ORCA - R^2$ camera with exposure time. The calculation was based on equation 6.8.

From Figure 6.9, one can see that the SNR will be over 8 times better when using the 8x8 binning mode compared to without using binning.

6.6 The Noise Equivalent to Power (NEP) of the CCD

It has been determined in Chapter 3 Section 3.4.1 that the selected photodetector for System I has the NEP of 150 fW.(Hz)$^{-1/2}$ over 5 mm^2 or 30 fW.(Hz)$^{-1/2}$.mm^{-2}.

In order to make a direct comparison with the photodetector in System I, one should work out the NEP of the selected CCD for System II. This section addresses the NEP of the CCD ORCA-R^2.

From the ORCA-R^2 specifications, the real dark noise of the CCD is negligible, at much less than an electron/second. The noise is dominated by readout noise, the charge that is injected into the analog channel during clocking out of the data. In this case, the readout noise is 6 electrons in normal scan mode. Each photon has a chance equal to QE (quantum efficiency) of generating an electron. The QE of ORCA-R^2 CCD camera is 50% at the wavelength of 700nm. Hence 6 electrons of noise are equivalent to 12 photons.

Assuming the signal integration is $1s$, then the readout noise is equivalent to 340x10^{-18}W.(Hz)$^{-1/2}$ = 340aW.(Hz)$^{-1/2}$.

As an example, Figure 6.10 shows the NEP at SNR=1, the integration time is 0.027 seconds, assuming the photon flux is 500 photons pixel^{-1}. second^{-1}, it is equivalent to the fluorescence power of 10^{-8}M Cy5.5 collected from a sensor spot of 30 μm x 1.5 mm in practice.

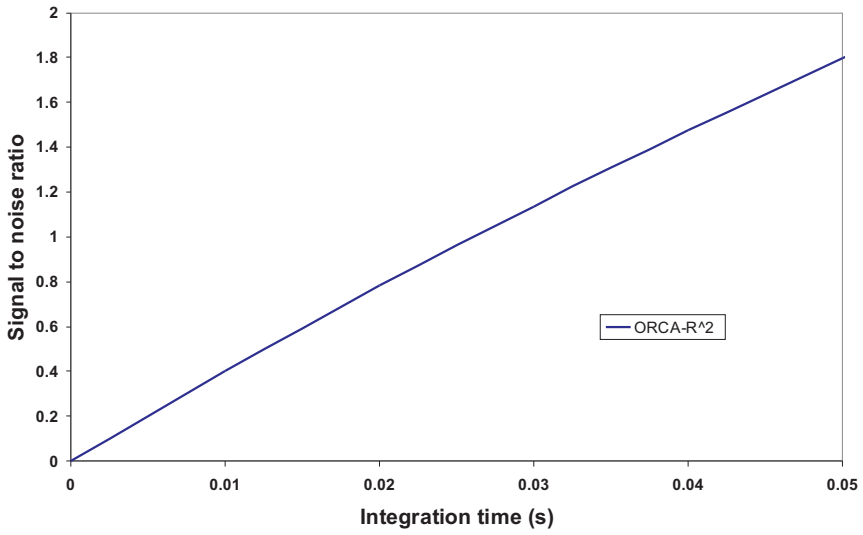

FIGURE 6.10: NEP at signal = noise at 0.027s. Assuming the photon flux is 500 pixel^{-1}. second^{-1}.

Therefore, the NEP of the CCD camera system, in this case, over the area of one mm^2, is 25fW.(Hz)$^{-1/2}$.mm^{-2}, which is comparable with photodetector system.

In general, the CCD is more preferable, in terms of noise performance, as one could choose a smaller area for signal, in other words, the CCD system has the flexibility in defining the sensing configuration.

6.7 Instrumentation

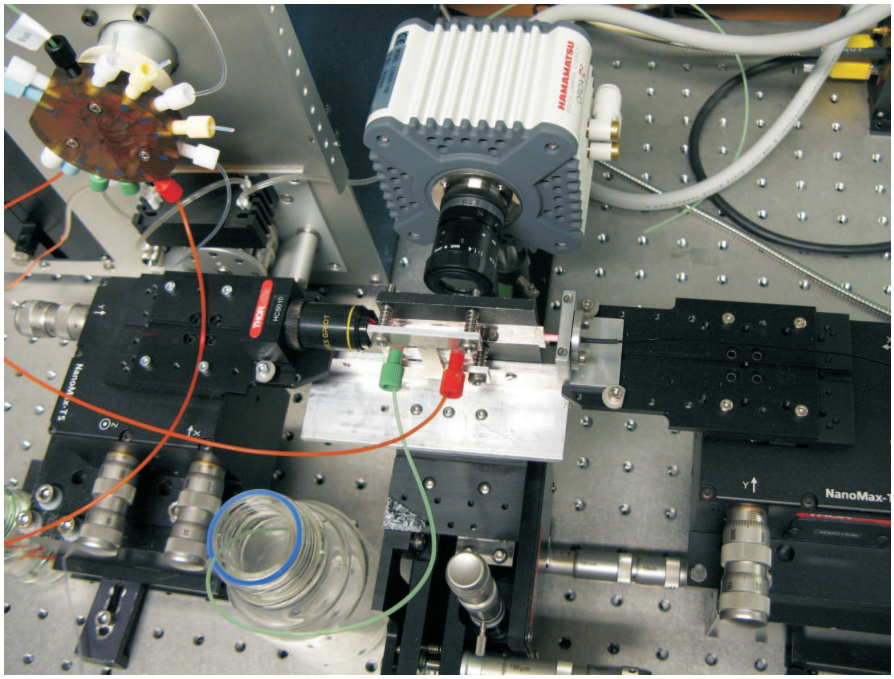

FIGURE 6.11: Experimental set up.

Figure 6.11 shows the CCD detection system. In order to make a direct comparison with two detector systems, the same sensor chip design was used with the CCD detector system. The iFLEX fibre-coupled laser diode from Point-Source, operating at the wavelength of 635nm, with an output power of 5mW (the same laser used in System I), is butt-coupled into the input waveguide of the sensor chip (from the right side of the sensor chip) to pump the Cy5.5 fluorophores. A micro-flow injection system from FIAlab, shown in Figure 6.11, is used to present initial samples to the sensor surface. The excited fluorescence is filtered to remove stray pump light collected and detected by the CCD camera (model ORCA-R^2 from Hamamatsu) behind the sensor chip. The output power from one branch of four outputs of the sensor chip is collected by a microscope lens and monitored on a power meter. This is in order to optimise the input power, since the fibre is not permanently pigtailed to the chip for these experiments.

LabVIEW software was used for the system integration, which enables integrated control of the laser, flow injection system and the CCD camera and data acquisition. The following functions have been implemented:

- Control of all functions of the flow-injection analyser;
- Control and power feedback functions of the laser;
- Capturing frames from the CCD at a maximum rate of 40 frames.sec^{-1}. The camera is run with internal triggering, images are captured and calculations performed on them to produce an array of 32 values proportional to the fluorescence power emitted from the 32 software-specified "regions of interest" (ROIs);
- Thermistor sensors are provided for the temperature measurement of two regions in the sensor assembly, and these temperatures are logged;
- NI 6009 USB module is used for all control and measurement functions.
- A bitmap image of the exposed sample, and additional data relating to the test type, time and temperatures are recorded.

6.8 Fluorescence measurements

In this section, detailed fluorescence measurements using the CCD detector system and the outcome of these experiments are presented. Importantly, it addresses the limit of detection (LOD) of System II, which leads to the direct comparison with the LOD of System I.

6.8.1 Fluorescence measurements

This section presents the results of the fluorescence test for the CCD camera detector system, which enables the limit of the detection of System II to be determined and an estimate made of detectable surface density for dye molecules.

Fluorescence measurements were carried out using the set up in Figure 6.11, which shows a sensor chip fitted in the custom made optical block and with a flowcell attached. Cy5.5

from Amersham Pharmacia was chosen for the bulk dye experiments, as it was used for the previous dye experiments. The sensor chip was newly fabricated using the same design as the sensor chip in System I, but without the Ta_2O_5 film, since the sensor chip without the coated Ta_2O_5 film has been proved to have good sensitivity from previous experiments. The bulk Cy5.5 dye solutions of 10^{-6}M - 10^{-8}M in water were tested. The excited fluorescence at around 700nm was collected by the CCD camera ORCA-R^2 located behind the sensor chip, and the data and condition of the test were recorded via a computer.

Figure 6.12 shows the bulk dye result from the newly fabricated sensor chip with a 60μm taper waveguide. The dye concentration is 4.4x10^{-6}M, with 49μW of laser power measured in the waveguide. The size of selected ROIs on the CCD camera corresponds to the size of the sensing patches on the sensor chip. The A/D converter of the CCD camera was set as 12 bit, and no binning was used in this case and the exposure time was one second.

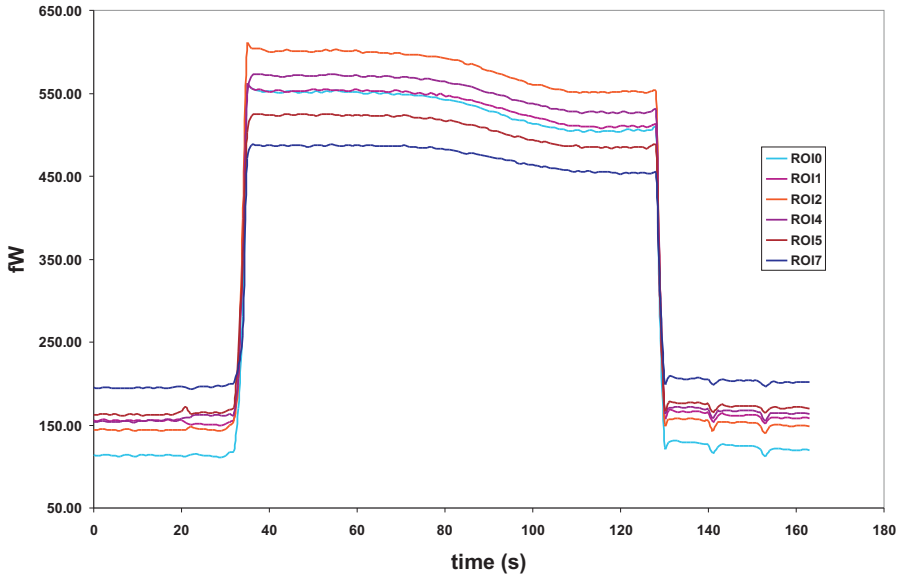

FIGURE 6.12: 4.4x$10^{-6}M$ Cy5.5 on sensor chip No 15 with the 60μm taper waveguide with a 49μW measured laser power in the waveguide (one of set of data showed in Figure 6.13).

Figure 6.13 shows the changes in fluorescence signal with changes in laser power measured in the waveguide, the result gave a response of 8.7$\pm$ 0.5fW.μW$--1$, between the output fluorescence power and the laser input power in the waveguide. While Figure 6.14

shows the changes in SNR that corresponded to the dye experiment results in Figure 6.13, which demonstrated that there is an optimum power level beyond which the plot saturates, increasing the input laser power implies a direct increase in the fluorescence signal, but the downside is that as the signal increases the noise will also increase, so the SNR will be degraded.

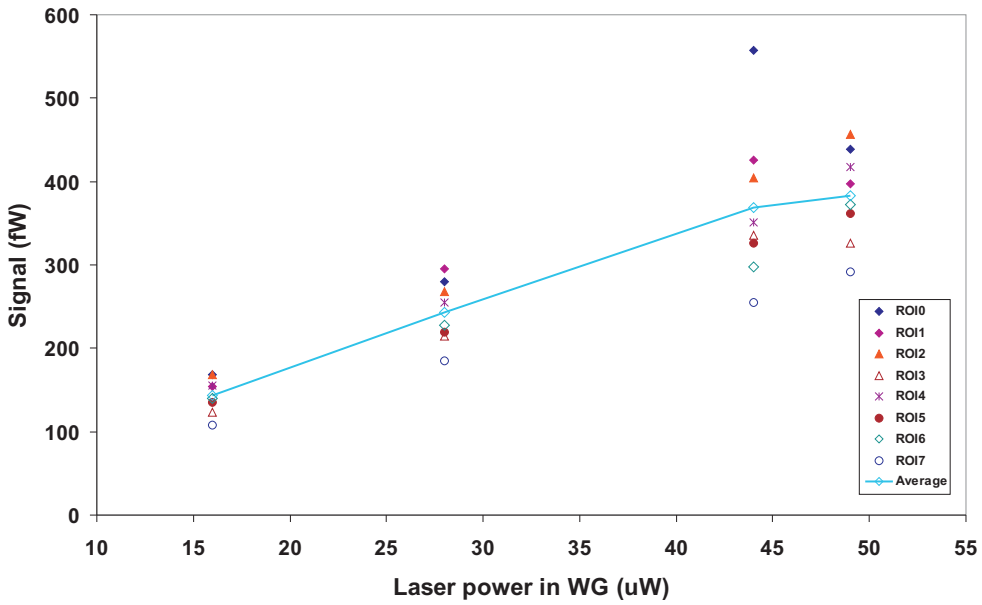

FIGURE 6.13: Fluorescence signal of 4.4x10^{-6}M Cy5.5 tests on sensor chip No 15 with the 60μm taper waveguide, against different levels of laser power in the waveguide.

Figure 6.15 presents the bulk dye result with dye concentrations from $10^{-7}M$ to $10^{-5}M$ of Cy5.5 applied onto the newly fabricated sensor chip with the 30μm width waveguide. This shows that the average fluorescence signal increases about 19 and 24 times when the dye concentration increases from $10^{-7}M$ to $10^{-6}M$, and from $10^{-6}M$ to $10^{-5}M$ respectively.

However, Figure 6.16 shows the average SNR of the same set of data as in Figure 6.15 against the different dye concentrations, it shows that the SNR increases less compared to the increasing rate of the dye concentration (under the same laser input power). This might be due to some pixels in ROIs being saturated. The software of the data acquisition part was reviewed and modified, with the addition of the function of notifying any saturation of any pixels after this experiment.

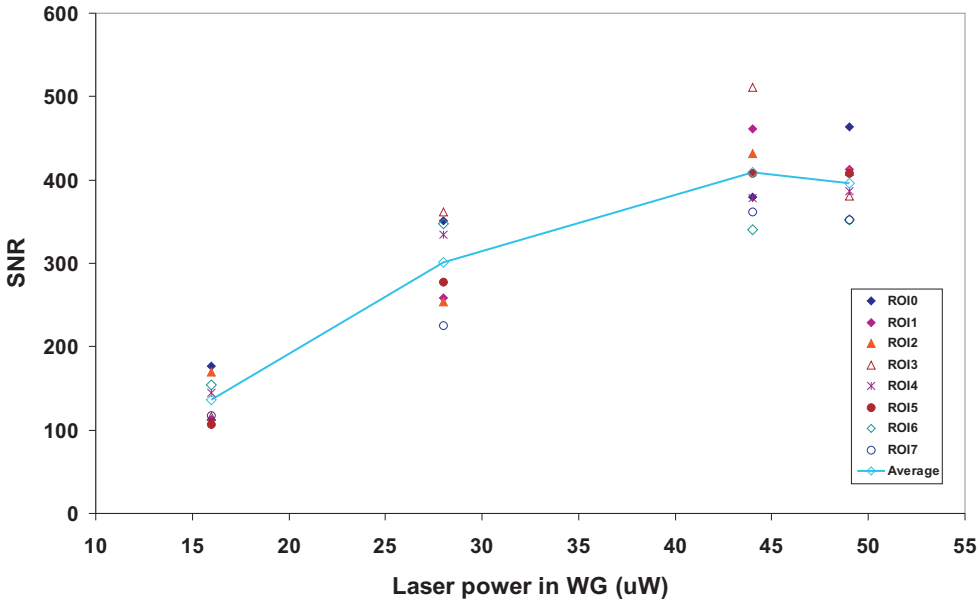

FIGURE 6.14: SNR of $4.4\text{x}10^{-6}M$ Cy5.5 tests on sensor chip No 15 with the 60μm taper waveguide, against different levels of laser power in the waveguide.

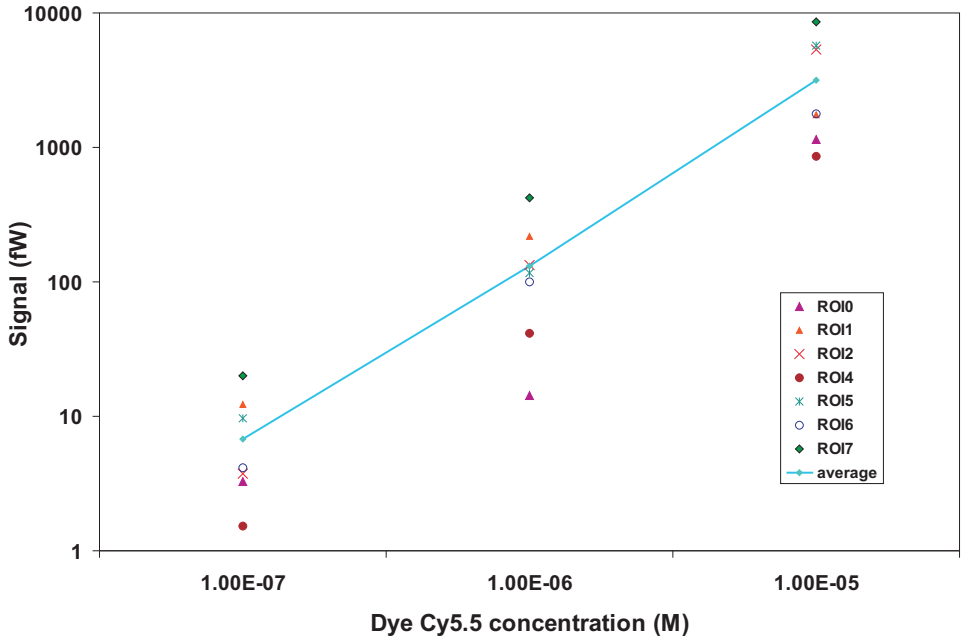

FIGURE 6.15: Dye Cy5.5 tests with different concentrations from $10^{-7}M$ to $10^{-5}M$ on the sensor chip No 15 with the 30μm taper waveguide, without Ta_2O_5 film, at room temperature.

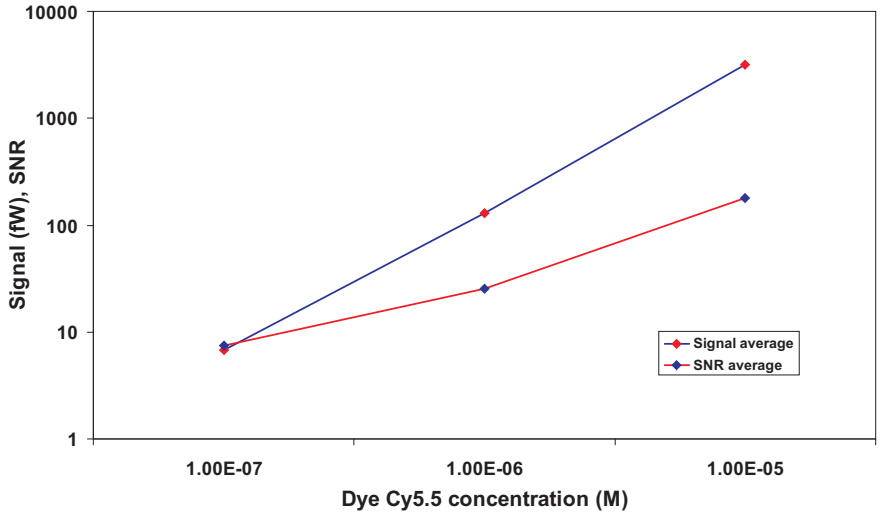

FIGURE 6.16: The average fluorescence signal of dye Cy5.5 tests with different concentrations from $10^{-7}M$ to $10^{-5}M$, on sensor chip No 15 with the 30μm taper waveguide (same set of data as shown in Figure 6.15), compared with the average SNR of the same data.

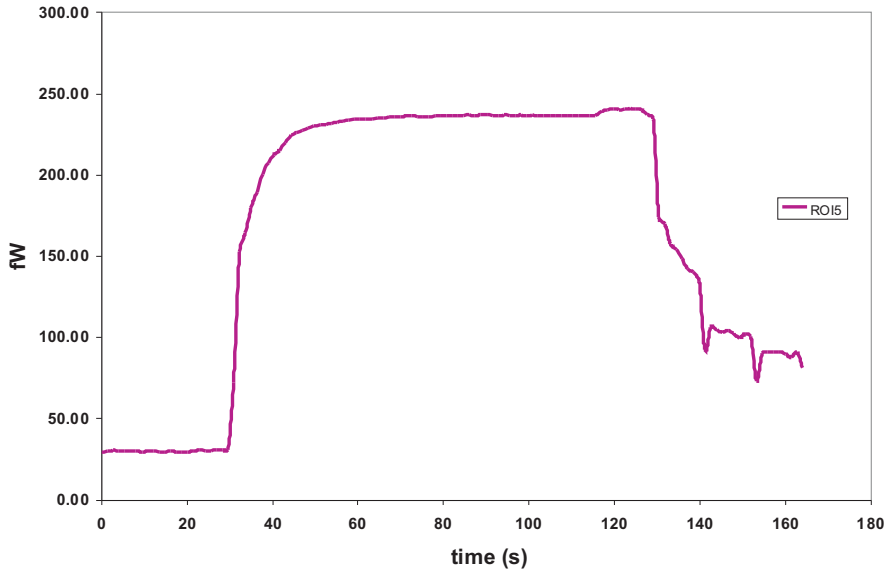

FIGURE 6.17: $10^{-7}M$ Cy5.5 test on the sensor chip No 15 with the 60μm width taper waveguide, without Ta_2O_5 film at room temperature.

Figure 6.17 shows a typical dye pulse of one of the sensing patches. The Cy5.5 dye concentration was $10^{-7}M$, and the test was carried out on the sensor chip with the 60μm taper waveguide. The maximum of 8x8 binning was used in this case, in order to improve the SNR, and a SNR of 600 was achieved as a result. The power in fW shown on the plot was converted from the CCD digital signal, the sum of counts of ROI.

Assuming N_p is the total number of photons reaching the CCD,

$$N_p = (\frac{1}{\eta_{qe}})vC \tag{6.9}$$

In which, $\eta_{qe} = 50\%$ is the quantum efficiency of the CCD camera, v is the analog-to-digital conversion factor, v= 4.4 (electrons / AD counts), in this case. C is the sum of counts (digital signal) over the ROI from the CCD camera.

The total energy of these N_p is $N_p h\nu(J)$, therefore, the power equals:

$$\frac{N_p h\nu}{t} = (\frac{h\nu}{\eta_{qe}})\frac{vC}{t} \tag{6.10}$$

Where h is Planck's constant, $\nu = c/\lambda$, c is the speed of light, λ is dye emission wavelength and t is the integration time.

6.8.2 Comparison of theoretical results and experimental outcomes

Table 6.3 shows theoretical and experimental results for the CCD detector system. The theoretical result was under the condition of 1% of maximum assay response (blank measurement) with 1mW input laser power in the waveguide, the second row of the table shows that 2.5pW.mW^{-1}@10^{-8}M and 2pW.mW^{-1}@10^{-8}M should be expected for the collected fluorescence power by the tapered waveguide opening with 30μm and 60μm respectively, the 4-way split was not considered in the theoretical prediction.

The 0.4pW.mW^{-1}@10^{-8}M listed in the third row of the table was the result of the bulk dye experiment on the newly fabricated sensor chip with a 60μm taper waveguide opening. The chip has a total loss of 16dB (6dB loss due to the 4 way split and 10dB loss due to the transmission and silica layer), there was no Ta_2O_5 film coated on the surface. This result is comparable with the theoretical result, and a good SNR of 600 was achieved with this chip.

A result of 74 pW.mW^{-1}@10^{-8}M was obtained for the sensor chip No 13-3 fabricated for the AWACSS project, the chip has 37nm of Ta_2O_5 film coated on the sensor surface,

this result is about 3.4 times lower compared to the result of sample 13-3 in Table 4.1, due to damage to the input end of the chip.

CCD Detetor System	Estimated Laser Power in WG(mW)	Estimated /measured Power in WG(μW)	Dye Conc. (M)	WG width (μm)	Fluorescence Outpuot for WG width 30&60 (μm)	pW.mW^{-1} at10^{-8}M
In theory*	1	1000	1.2x10^{-8}	30/60	3pW/2.4pW	2.5(30μm) 2(60μm)
In practice Sample No 15-3**	1	25/58	10^{-7}	60	206fW	0.4(No Ta_2O_5 film)
In practice Sample No 13-3***	1	63/0.94	10^{-8}	60	70fW	74 (With 37nm Ta_2O_5 film)

Note:	
*	under the condition of 1% of maximum assay response (blank measurement)
**	6dB loss due to the 4-way split. 10dB due to transmission and silica layer loss
***	6dB loss due to the 4-way split. 5dB transmission loss and 1dB silica layer loss

TABLE 6.3: Comparing the theoretical results with experimental outcomes of the CCD detector system.

Overall, the theoretical prediction of 0.5 pW.mW^{-1}@10^{-8}M fluorescence power collection should be reached if one takes the 4-way split waveguide structure into account for the 60 μm taper waveguide, so it is in a good agreement with the experimental result of 0.4 pW.mW^{-1}@10^{-8}M for the same waveguide (assuming a linear response of concentration of dye with the fluorescence signal power).

6.8.3 Detection limit of System II

The limit of detection is defined as three times the dye concentration divided by the signal to noise ratio, where, the noise is defined as the square root of squared standard deviation of the signal and the squared standard deviation of the background signal (noise=$\sqrt{\sigma^2_{signal} + \sigma^2_{background}}$).

The signal is defined as an averaged signal over a series of data in the peak region of the dye pulse, from which the background signal was deducted. The background signal was an average signal taken before the beginning of the dye pulse.

Therefore, from the outcome of the bulk dye experiments, a limit of detection below 3 x $10^{-10}M$ Cy5.5 was determined for the CCD detector system.

This results in a surface density detection limit of 1.3x10^4 antibodies.mm^{-2} based on the calculation in Section 4.4.2.1, which is about one order of magnitude better than the detection system requirement.

In Chapter 4, Section 4.4.1, the LOD of 2.8x$10^{-9}M$ Cy5.5 was found for the sensor chip without Ta_2O_5 film. In this section, a limit of detection below 3 x $10^{-10}M$ Cy5.5 was determined for the CCD detector system, which is about one order of magnitude better than System I. There is still room for improvement and optimising the CCD detection system could reduce the LOD even further.

6.9 Conclusion

In this chapter the optical apparatus, instrumentation and the performance analysis of a CCD detector system for multisensor immunoassay were described. It was estimated theoretically that the collection efficiency of the CCD detector system is about three times better than the fibre collecting photodiode detector, largely due to the assumption that 100% of the light hitting the lens would fall on the CCD sensor chip, while only 11% of the light from the end of the light collecting fibre would fall on photodiode. Although Table 6.1 shows that the fibre collection up to the filter in system I is better than lens collection up to the filter in CCD system, the combination of fibre collection and CCD may offer better collection efficiency in theory, but it will limit the flexibility in defining the sensing configuration in reality. The results of bulk dye experiments of the system were presented, which is 0.4pW.mW^{-1}@10^{-8}M and it is comparable with the theoretical prediction of 0.5pW.mW^{-1}@10^{-8}M, and a good agreement is reached. It also addressed detailed analysis on Signal to Noise Ratio of the CCD camera and optimisation of the camera in order to improve the SNR. Improvements could be undertaken from three aspects: using larger binning in order to reduce the readout noise; increasing the exposure time to increase the signal strength, also using the better cooling method to reduce the thermal noise; and finally, integrating with many short exposure times, especially for those analytes that cannot survive under a long exposure time due to the photobleaching.

While the NEP for both CCD and photodetector systems are comparable, the CCD system is preferable due to its flexibility in defining the sensing region and the low noise performance. A limit of detection below 3 x 10^{-10}M Cy5.5 was determined for System II, which is about one order of magnitude better than System I and two orders of magnitudes better than the detection requirement for the system.

Chapter 7

Conclusions

7.1 Overall conclusion

A novel 32-analyte integrated optical fluorescence-based multisensor chip has been realised, and integrated with fluidics, a detection system, surface chemistry, immunochemistry, and a computer for control and signal processing. The performance of this biosensor system has been demonstrated with the key pollutant estrone. A detection limit of 1 ng.L^{-1} was achieved (with a range up to 1 μg.L^{-1}). This is two orders of magnitude better than that required by EU legislation for organic pollutants, and it is expected that improvements in sample handling and signal processing will reduce this further.

Extensive study was carried out theoretically and experimentally in order to optimise the sensor chip design, fabrication and sensing system. A tapered waveguide section was introduced into the sensor chip design to reduce the power density of excitation radiation at the sensing surface, hence reducing the rate of photobleaching and maintaining the overall signal strength and the sensitivity of the device. In order to maintain a uniform power distribution in a wide, and hence highly multi-moded waveguide, it is desirable to excite only the fundamental mode which is the lowest-order spatial mode of a channel waveguide. If the rate of increase in the width of the waveguide is slow enough, the broadening of the modal field is essentially adiabatic resulting in all of the launched light remaining in the fundamental mode of the waveguide. A theoretical study and simulation using BPM were carried out with taper widths of 30μm, 60μm and 100μm.

The taper widths of 30μm and 60μm were chosen for the final mask design, to avoid significant excitation of higher order modes while keeping the taper length to 10mm, due to chip size constraints. A set of preliminary test waveguides were fabricated under various conditions in order to determine the optimum production process for the sensor array chip, aiming for low loss, high signal strength and robustness.

Particular attention has been paid to the fibre to waveguide coupling efficiency. Since the ultimate device discussed in this thesis would be a portable type of instrument which requires the sensor chip to be pigtailed with a fibre, this allows an easy method for connecting and coupling light from a laser source. Therefore, to optimise the fibre to waveguide coupling efficiency is essential. A thorough investigation was undertaken theoretically and experimentally and the best coupling efficiency, of 80.2% in the TE mode, was achieved and corresponded to the fabrication conditions of 2.5 μm waveguide opening with 2 hours of ion exchange time. Subsequently, low loss, high signal strength and robust optical transducers were realised based on the optimised mask design and fabrication process.

The surface intensity of the sensor region was studied in depth based on the establishment of a precise 2D refractive index profile for the waveguide. Extensive studies were undertaken mathematically in terms of step by step calculation of the optical power collection efficiency of the detection system, in order to estimate the power flow in the detection system, which is vital for the design of the detection system. The photodiode-based detection schemes which consist of the photodiodes with integral amplifiers, an amplification and prefiltering stage, were experimentally evaluated for cost, noise, stability and detection limit.

A system detection limit was estimated theoretically based on immunoassay characteristics, and an equivalent detection limit of the system for dye solution was also predicted. It was estimated that 1pW of fluorescence power should be collected by the fibre and photodiode detection system with 1mW laser power in a 30μm width taper waveguide, under the area of 30μm x 1.5mm. Subsequently, extensive bulk dye fluorescence measurements were carried out, in order to confirm low-noise operation of the detection system and determine an ultimate detection limit in terms of the number of Cy5.5 molecules per unit area. In practice, a 2pW of fluorescence power was achieved under the same condition as theoretically predicted. LOD of 7.7 x 10^{-11}M and 2.8 x 10^{-9}M were achieved

for the sensor chips with and without Ta_2O_5 high index film respectively. If a detection limit of 10^{-10}M Cy5.5 is assumed, this is equivalent to the minimum detectable surface density of 4.36 x10^3 antibodies.mm^{-2}, which is at least one order of magnitude better than the detection system requirement.

Surface chemistry and immunoassay experiments were carried out in cooperation with the project partner in the University of Tübingen, Germany. The antigen and antibody were provided by the project partner from King's College, University of London. Extensive immunoassay trials were undertaken, in order to calibrate the detection system initially using estrone as the analyte. Subsequently, the system was applied to detect up to six organic pollutants (propanil, atrazine, isoproturon, sulphamethizole, bisphenol A and estrone), and a good detection limit of 1ng.L^{-1} for the system has been achieved. The overall performance of the detection system, in comparison to the conventional analytical and immunosensor techniques, was tested and also undertaken by other project partners. The results showed that the system is fully comparable to conventional analytical techniques in terms of accuracy, repeatability and reproducibility, while selectivity allowed for trace analysis even in complex matrices such as sediment extracts. In addition, the analysis only takes a few minutes without any prior sample pre-concentration nor any pre-treatment steps, and it cuold regenerate upto 500 times without replacing the sensor chip.

A detailed study was carried out in a CCD detection system theoretically and experimentally. It was estimated theoretically that the light collection efficiency of the CCD detector system is about three times better than the fibre collecting photodiode detector, this is based on the assumption that 100% of the light reaching the lens would fall on the CCD sensor chip, while only 11% of the light from the end of the light collecting fibre fell on the photodiode. The results of the bulk dye experiments of the system was presented, which is 0.4pW.mW^{-1}@10^{-8}M, and it is comparable with the theoretical prediction of 0.5pW.mW^{-1}@10^{-8}M. Improvements could be undertaken from three aspects in order to improve the SNR: using larger binning in order to reduce the readout noise; increasing the exposure time to increase the signal strength, also using the better cooling method to reduce the thermal noise. Finally, integrating with many short exposure times, especially for those analytes that cannot survive under a long exposure time due to the photobleaching. The NEP for both CCD and photodetector systems

are comparable, however the CCD system is preferable due to its flexibility in defining the sensing region and low noise performance. A limit of detection below 3 x 10^{-10}M Cy5.5 was determined for System II, which is about one order of magnitude better than System I and two orders of magnitude better than the detection requirement for the system.

Overall, an integrated optical fluorescence multi-sensor system was presented; the applications of this system will be in environmental monitoring, medical diagnostics and biotechnology. The applications are not for screening very large numbers of compounds in high concentrations, but fairly low numbers of compounds in very low concentrations. End-users will include instrument manufacturers and scientific researchers who wish to analyse small volumes of analyte for multiple compounds with good stability and repeatability and low detection limits.

The main innovative features in this work are multi sensing integration on a sensor chip, including integration of 32 sensing spots, selection of waveguide materials technology and optimisation of fibre coupling, surface irradiance, isolation layer, with incorporation of tapered waveguides for reduced photobleaching and high-index over-layers for improved pump efficiency. Optimisation of the fabrication parameter and the process; power budget: calculation from input power, output power, emitting and collection for both detection systems. Integration the sensor chip to the detection system including the interface with microfluidics system, establishing the apparatus for improving optical alignment and signal collection from photodiode arrays via hardware tests for photodiode array readout, and operation to detect 6 organic pollutants simultaneously and with the detection limit of 20ng.L^{-1}, the best performance reported. The waveguide design leading to high sensitivity, the mass-fabrication technology employed for the chips, which will help to keep unit costs down, and the robust connection to instrumentation, which is expected to lead to greater reliability, ease of use, and reduced detection limits through improved stability. These sensor devices are being developed for fluorescence-based measurements but may potentially be applied to other surface scattering or luminescence techniques, such as Raman spectroscopy.

7.2 Future work

The silica isolation layer in the present sensor was found to have deteriorated beyond repair after 400∼500 measurements. This deterioration was caused by the gradual erosion of the layer by 0.5% sodium dodecyl sulphate (adjusted with HCl to pH 1.8) solution, which was used in the regeneration process to remove the remaining fluorescence labelled antibodies bonded on the sensor surface and to prepare the system ready for the next measurement. Therefore looking for a suitable isolation layer or a different sensor chip fabrication technique with different substrates such as sapphire has priority in the next phase of study, in order to produce low loss and robust new generation sensor chips.

Through-out the project period, laser breakthrough and background fluorescence have been found to be problems which cause the reduction of the signal to noise ratio. Selecting the correct filter to strip off the pump source is one way to overcome the laser breakthrough problem. More efforts should also be made into studying the fluorescence behaviour of various glass and crystal materials which are chosen as the host substrate of the sensor chip. Better signal to noise ratio can be achieved by using a substrate which is less sensitive to the pump source in terms of exciting fluorescence.

Another feature of the present sensor chip is the reduced rate of photobleaching which was achieved by broadening the waveguide. The measurement results show that the detection limit of the system is good and it is within EU regulation, therefore the system did not take the broadening issue into account. But for the future improvement of signal to noise ratio and sensitivity, detailed and systematic study on the raw data of various width of waveuide against photobleaching rate should be carried out.

The system has been developed for the application in river water monitoring, which is the main objective of the AWACSS project. Although this project has now been completed, the potential of this system has to be explored further.

Work building upon that described in this thesis will continue towards an optical waveguide sensor for highly sensitive detection and quantification of cytokines in biological fluids. This aims at quantifying cytokines (such as IL-1α, and IL-1β, IL-6 or TNFα) at the ng.L^{-1} range in biological fluids which might lead to significant potential for many other bioscience applications. The system can also be applied in medical science such as in DNA recognition, or in the food industry such as for the detection of toxicity, etc..

Exploration of new areas for the application of this system will also form part of the future work.

Appendix A

Power Collection

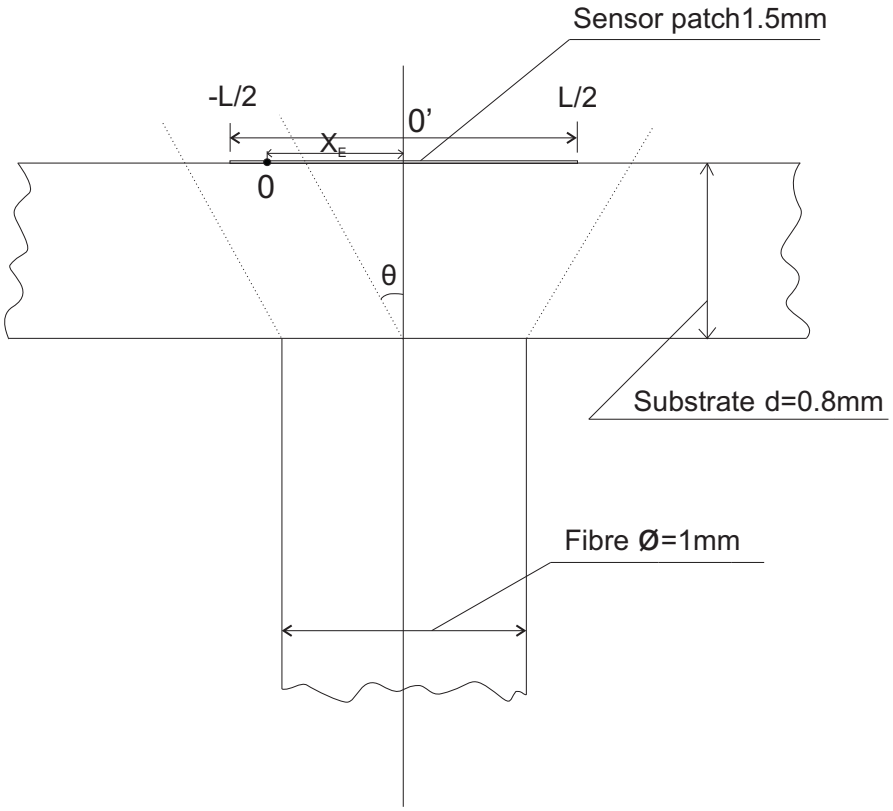

FIGURE A.1: The Sketch shows the fluorescence collecting fibre butt-coupled underneath the sensor patch.

In this appendix, a detailed calculation of how much fluorescence emitted by the 1.5mm long and 30 μm width waveguide within the sensor patch was collected by the fibre (NA=0.51±0.03) underneath the sensor patch is given. The Figure A.1 shows the fluorescence collection fibre underneath the sensor substrate. The calculation has three

parts: Part one considers the dye molecules of Cy5.5 which are located outside of the fibre region, as shown in Figure A.2. Parts two and three take into account the dye molecules within the fibre area with different ranges shown in Figures A.3 and A.4.

A.1 Case A ($\mathbf{x}_E \geq R_f$)

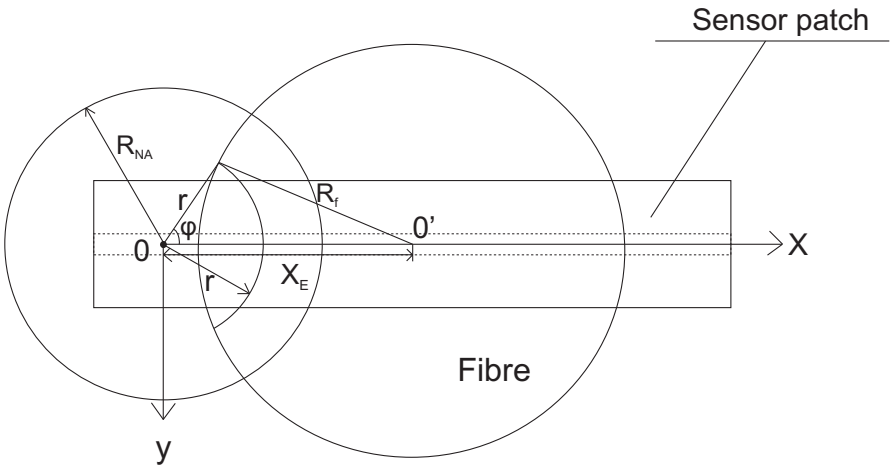

FIGURE A.2: View from the top of the sensor patch. In case A, the Cy5.5 molecules are located outside of the fibre region.

The fluorescence intensity from a single molecule reaching the fibre can be expressed as

$$I\ (x,y) = \frac{P_m(x_E, y_E)}{4\pi(d^2 + x^2 + y^2)} = \frac{P_m(x_E, y_E)}{4\pi(d^2 + r^2)} \tag{A.1}$$

In which, $\mathrm{r}^2 = x^2 + y^2$; $P_m(x_E, y_E) = power/molecule$ at position (x_E, y_E).

Therefore for the power from a molecule in the analysis region (P_E) :

$$\begin{aligned} P_E(x_E, y_E) &= \int I(x,y)dxdy = \int I(r,\varphi)rdrd\varphi \\ &= \frac{P_m(x_E, y_E)}{4\pi} \int_{x_E - R_f}^{R_{NA}} rdr \frac{1}{d^2 + r^2} 2 \int_0^{\varphi_{max}(r)} d\varphi \\ &= \frac{P_m(x_E, y_E)}{4\pi} \int_{x_E - R_f}^{R_{NA}} rdr \frac{1}{d^2 + r^2} 2\varphi_{max}(r) \\ &= \frac{P_m(x_E, y_E)}{4\pi} \int_{x_E - R_f}^{R_{NA}} dr \frac{2r}{d^2 + r^2} arccos \frac{r^2 + x_E^2 - R_f^2}{2rx_E} \end{aligned} \tag{A.2}$$

In which,

$$R_f^2 = r^2 + x_E^2 - 2rx_E cos\varphi_{max}(r) \tag{A.3}$$

$$cos\varphi_{max}(r) = \frac{r^2 + x_E^2 - R_f^2}{2rx_E} \tag{A.4}$$

$$\varphi_{max}(r) = arccos\frac{r^2 + x_E^2 - R_f^2}{2rx_E} \tag{A.5}$$

$R_f = 0.5mm$, $d = 0.8mm$.

Assuming that the dye emits isotropically and ignoring the effects of the glass slide.

$\mathrm{NA}_{fibre} = Sin\theta = 0.48, \theta \approx 28\,^\circ$. $\mathrm{R}_{NA} = d \times tan\theta = 0.8mm \times 0.53 = 0.424mm$.

The total power reaching the fibre in case A (P_A) should be:

$$\begin{aligned} P_A &= 2\int_{R_f}^{L/2} dx_E \int dy_E P_E(x_E, y_E)\rho \\ &= 2\int_{R_f}^{L/2} dx_E \int_{x_E - R_f}^{R_{NA}} dr \frac{2r}{d^2 + r^2} arccos\frac{r^2 + x_E^2 - R_f^2}{2rx_E} \int dy_E \frac{P_m(x_E, y_E)}{4\pi}\rho \end{aligned} \tag{A.6}$$

In which, $L = 1.5mm$, where ρ is the molecule density, ρ =number of molecules/area, note: neglecting the dependence on y_E.

Calculating the integral of the first part of the equation A.6 using a numerical method and neglecting the x_E- dependence of P_E, the following result can be obtained,

$$P_A = 0.0966(mm) \int dy_E \frac{P_E(y_E)}{4\pi}\rho \tag{A.7}$$

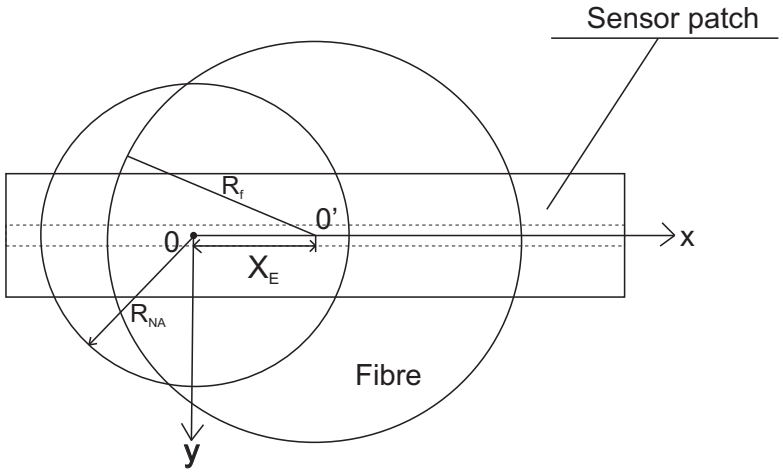

FIGURE A.3: View from the top of the sensor patch. In case B, the Cy5.5 molecules are located within the fibre region ($R_f - R_{NA} \leq x_E \leq R_f$).

A.2 Case B ($R_f - R_{NA} \leq x_E \leq R_f$)

$$\begin{aligned} P_E(x_E, y_E) &= \frac{P_m(x_E, y_E)}{4\pi} \int_0^{R_f - x_E} r dr \frac{1}{d^2 + r^2} \int_0^{2\pi} d\varphi \\ &+ \frac{P_m(x_E, y_E)}{4\pi} \int_{R_f - x_E}^{R_{NA}} r dr \frac{1}{d^2 + r^2} 2 \int_0^{\varphi_{max}(r)} d\varphi \\ &= \frac{P_m(x_E, y_E)}{4} log \frac{d^2 + (R_f - x_E)^2}{d^2} + \frac{P_m(x_E, y_E)}{4\pi} \\ &\int_{R_f - x_E}^{R_{NA}} dr \frac{2r}{d^2 + r^2} arccos \frac{r^2 + x_E^2 - R_f^2}{2 r x_E} \end{aligned} \tag{A.8}$$

The total power reaching the fibre in case B should be:

$$P_B = 2 \int_{R_f - R_{NA}}^{R_f} dx_E \int dy_E P_E(x_E, y_E) \rho \tag{A.9}$$

A.3 Case C ($\mathbf{x}_E + R_{NA} \leq R_f$)

$$\begin{aligned} P_E(x_E, y_E) &= \frac{P_m(x_E, y_E)}{4\pi} \int_0^{R_{NA}} r dr \frac{1}{d^2 + r^2} \int_0^{2\pi} d\varphi \\ &= \frac{P_m(x_E, y_E)}{4} log \frac{d^2 + (R_{NA})^2}{d^2} \end{aligned} \tag{A.10}$$

The total power reaching the fibre in case C should be:

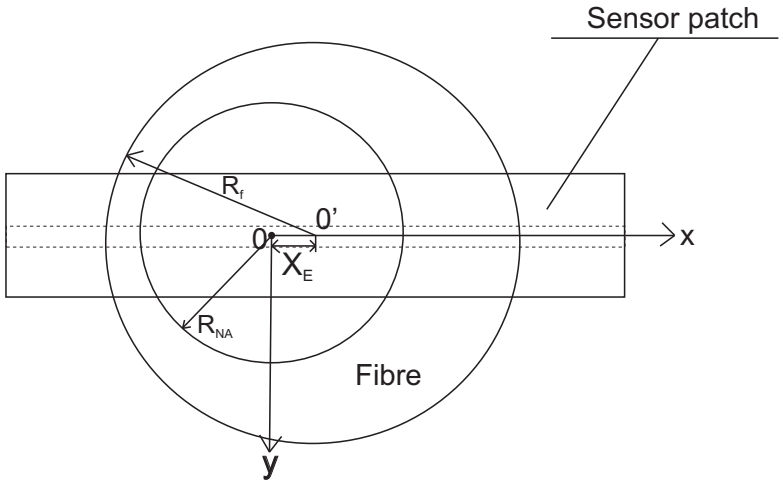

FIGURE A.4: View from the top of the sensor patch. In case C, the Cy5.5 molecules are located within the fibre region ($x_E + R_{NA} \leq R_f$).

$$P_C = 2 \int_0^{R_f - R_{NA}} dx_E \int dy_E P_E(x_E, y_E)\rho \tag{A.11}$$

A.4 Power collection

Therefore the total collected fluorescence light by the fibre is:

$$\begin{aligned} \eta &= \frac{P_A + P_B + P_C}{P_{total,emitted}}\% \\ &= \frac{P_A + P_B + P_C}{\int_{-L/2}^{L/2} dx_E \int dy_E P_m(x_E, y_E)\rho} \\ &= 3.67\% \end{aligned} \tag{A.12}$$

Note: $\int P_m(y_E)dy_E * \rho$ drops out of ratio.

Appendix B

Electronic signal filtering analysis

B.1 Principle of the analogue filter

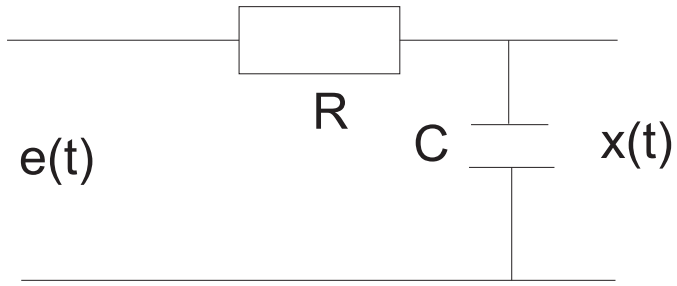

FIGURE B.1: A 1^{st} Order RC Low-Pass Filter, in which R is the resistance of a resistor, C is the capacitance of a capacitor, and $x(t)$ is the output alternating voltage which is equal to the voltage on the capacitor. Both R and C are constants.

To understand how a filter works, it is necessary to establish a relationship between the input signal and output signal for the electric circuit representing the filter.

Taking the 1^{st} order RC low-pass filter, shown in Figure B.1, as an example, the equation of the output voltage x(t) can be derived as follows.

Based on the serial electric circuit theorem, the sum of the voltages on the components in the circuit equal the input voltage, i.e.

$$V_R(t) + V_C(t) = e(t) \tag{B.1}$$

In which V_R and V_C are the voltages on the resistor and capacitor respectively, and e(t) is the input voltage. Note that V_C(t) = x(t).

Assuming the electric current in the circuit is I(t), the voltage on the resistor can be expressed as:

$$V_R(t) = I(t)R \tag{B.2}$$

The voltage on a capacitor is equal to the quantity of electric charge in the capacitor, Q(t), divided by the capacitance, i.e.

$$V_R(t) = Q(t)/C \tag{B.3}$$

Since the electric charge in the capacitor is equal to the net inflow of the electric current into the capacitor, i.e.

$$Q(t) = \int_0^t I(t)dt$$

$V_C(t)$, i.e. x(t), can then be written as:

$$V_C(t) = x(t) = \frac{1}{C}\int_0^t I(t)dt \tag{B.4}$$

Differentiating with respect to time t on both sides of the equation above, the following expression is obtained:

$$\frac{dx(t)}{dt} = \frac{I(t)}{C} \tag{B.5}$$

Comparing equation B.2 with equation B.5, the voltage on the resistor can be expressed as:

$$V_R(t) = RC\frac{dx(t)}{dt} = RCx'(t) \tag{B.6}$$

equation B.1 now becomes an ordinary first order and linear differential equation for the output voltage x(t):

$$RCx'(t) + x(t) = e(t) \tag{B.7}$$

Assuming at $t < 0$, there is no input signal, i.e. $e(t) = 0$ for $t < 0$, and $x(t) = 0$ when $t = 0$, the equation B.7 can be solved using a Fourier transform or the method of variation of constants. In order to illustrate the frequency characteristics of the circuit, the Fourier transform method is to be used to solve the equation.

Taking the Fourier transform (denoted by F) on both sides of equation B.7, and noting that

$$\mathrm{F(x(t))} = \mathrm{X}(\omega)$$

$$\mathrm{F(x'(t))} = j\omega\ \mathrm{F(x(t))} = j\omega\ \mathrm{X}(\omega)$$

equation B.7 becomes:

$$(j\omega\ \mathrm{RC} + 1)\ \mathrm{X}(\omega) = \mathrm{E}(\omega)$$

or

$$X(\omega) = \frac{1}{j\omega RC + 1} E(\omega) \tag{B.8}$$

In the above, ω is the circular frequency in radians per second.

Let

$$H(\omega) = 1/(j\omega RC\ + 1)$$

equation B.8 can then be written as:

$$X(\omega) = H(\omega)E(\omega) \tag{B.9}$$

In the above, $\mathrm{H}(\omega)$ is the "transfer function" which decides the characteristics of the electric circuit response to the input signal in the frequency domain. $\mathrm{H}(\omega)$ itself is entirely decided by the electric circuit and is independent of the input signal. It can be seen that the higher the input signal frequency ω, the lower the $\mathrm{H}(\omega)$ value, and therefore the lower is the output to input ratio $\mathrm{X}(\omega)/\mathrm{E}(\omega)$, which is the feature of a low-pass filter.

It can be seen that the original differential equation in B.7 has been reduced to an algebraic equation in B.8 by the Fourier transform. The solution for output signal x(t)

can be obtained by performing the inverse Fourier transform (denoted by F^{-1}) at both sides of equation B.8, i.e.

$$\begin{aligned} F^{-1}[X(\omega)] &= F^{-1}[H(\omega)E(\omega)] \\ &= F^{-1}[H(\omega)]^* F^{-1}[E(\omega)] \end{aligned} \tag{B.10}$$

in which "$*$" represents a convolution operation.

Note that,

$$F^{-1}[X(\omega)] = x(t)$$

$$F^{-1}[E(\omega)] = e(t)$$

and

$$\begin{aligned} F^{-1}[H(\omega)] &= F^{-1}[\frac{1}{j\omega RC+1}] \\ &= \frac{1}{RC}\exp(-\frac{t}{RC}) \\ &= h(t) \end{aligned} \tag{B.11}$$

(h(t) = 0 if t < 0)

equation B.10 becomes:

$$\begin{aligned} x(t) &= h(t)^* e(t) \\ &= \int_{-\infty}^{\infty} h(t-\tau)\, e(\tau)\, d\tau \\ &= \frac{1}{RC}\int_0^t \exp(-\frac{t-\tau}{RC})\, e(\tau)\, d\tau \end{aligned} \tag{B.12}$$

While the transfer function H(ω) exhibits the frequency characteristics of the circuit's response to the input signal, its inverse Fourier transform h(t), called the impulse-response function as given in equation B.11, shows the circuit's response to the input signal in the time domain, and the expression in B.12 demonstrates(in real time) how the input signal is modified by the circuit to become the output signal.

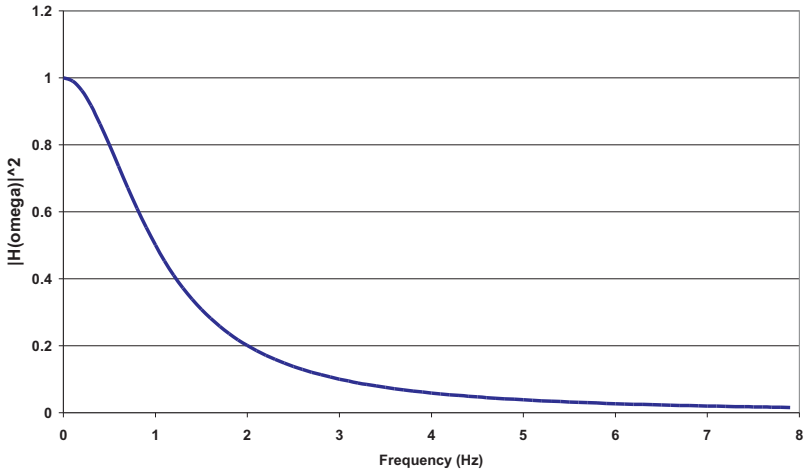

FIGURE B.2: Transfer Function (modulus squared) of the 1^{st} Order RC Low-pass Filter cut-off frequency = 1Hz or 6.283 rad.s^{-1})

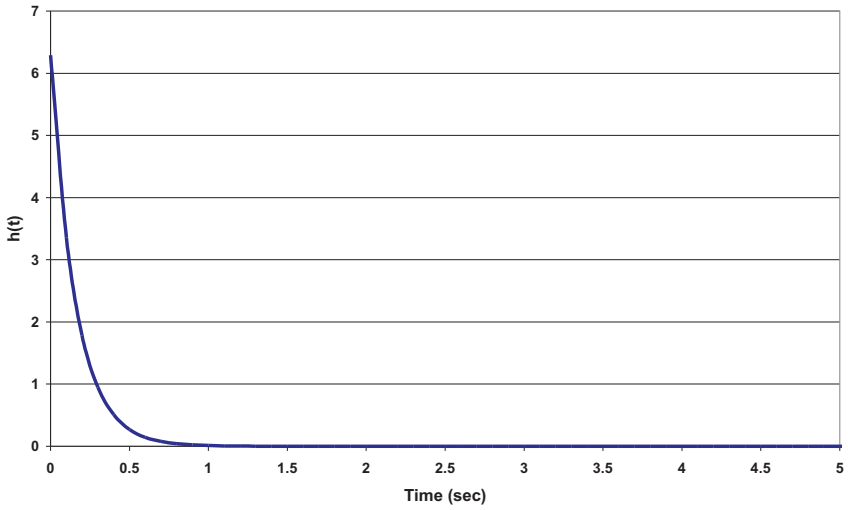

FIGURE B.3: Impulse-response Function of the 1^{st} Order RC Low-pass Filter (cut-off frequency = 1Hz or 6.283 rad.s^{-1})

Figure B.2 and Figure B.3 show the curves of the circuit's responses in the frequency domain (modulus of H(ω) given in B.13) and time domain (h(t) given in B.14), respectively.

$$|H(\omega)| = \frac{1}{\sqrt{1 + (RC\omega)^2}} \tag{B.13}$$

$$h(t) = \frac{1}{RC} exp(-\frac{1}{RC}) \tag{B.14}$$

The cut off frequency ω_c of this filter is decided by the RC value. By definition, the square of the modulus of the transfer function should have half of its value at zero frequency, i.e.

$$|H(\omega_c)|^2 = \frac{1}{1 + (RC\omega_c)^2} \tag{B.15}$$

which leads to:

$$\omega_c = 1/(RC)$$

Assuming the cut-off frequency is 1 Hz, or $\omega_c = 6.283$ (rad.s^{-1})), the corresponding RC value is RC = 0.159. For this RC value, the transfer function and the time response function of the filter are plotted in Figure B.2 and Figure B.3.

B.2 4^{th} Order Butterworth Low-pass Filter

Since the characteristics of a filter are described by its transfer function H(ω) or impulse-response function h(t), there is no need to look into the details of the electric circuit if either H(ω) or h(t) is available.

The transfer function of a 4^{th} order Butterworth low-pass filter is given as:

$$H(\omega) = \frac{\omega_c^4(A\text{-}iB)}{A^2 + B^2} \tag{B.16}$$

in which ω_c is the cut off frequency of the filter defined by

$$|H(\omega_c)| = \frac{1}{\sqrt{2}}\,|H(0)| \tag{B.17}$$

and

$$\begin{aligned} A &= (\omega_c^2 - \omega^2)^2 - 4\omega_c^2\omega^2 cos\frac{3\pi}{8} cos\frac{\pi}{8} \\ &= (\omega_c^2 - \omega^2)^2 - 1.4143\omega_c^2\omega^2 \end{aligned} \tag{B.18}$$

$$\begin{aligned} B &= 2(\omega_c^2 - \omega^2)^2\omega_c\omega(cos\frac{3\pi}{8} cos\frac{\pi}{8}) \\ &= 2.6131(\omega_c^2 - \omega^2)^2\omega_c\omega \end{aligned} \tag{B.19}$$

The modulus of the transfer function can be written as

$$|H(\omega)| = \frac{\omega_c^4}{\sqrt{A^2 + B^2}} \tag{B.20}$$

Note that selection of the cut-off frequency, ω_c, in this case is similar to selecting the RC value for the 1^{st} order RC filter in equations B.13 and B.14. Assuming the cut-off frequency of the filter is 1 Hz or $\omega_c = 6.283$ (rad.s^{-1}), the frequency characteristics of the 4^{th} order Butterworth filter can be demonstrated by the graph of the modulus squared of the transfer function in Figure B.4.

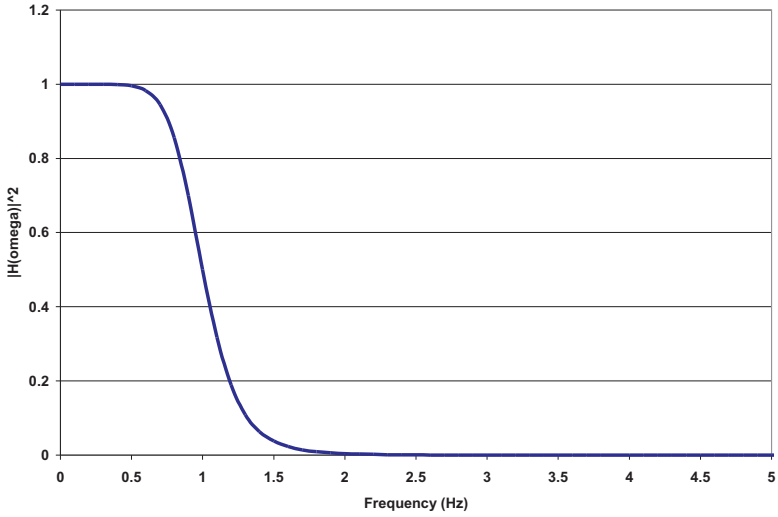

FIGURE B.4: Transfer Function (modulus squared) of the 4^{th} Order RC Low-pass Filter (cut-off frequency = 1Hz or 6.283 rad.s^{-1})

The time response function h(t), i.e. the impulse-response function, of the 4^{th} order Butterworth filter can be derived from its transfer function using the inverse Fourier transform. However due to the complexity of the transfer function, an analytical expression of h(t) is difficult to obtain. Instead, a discrete inverse Fourier transform can be used to derive the numerical time series of the function h(t), which is shown in Figure B.5.

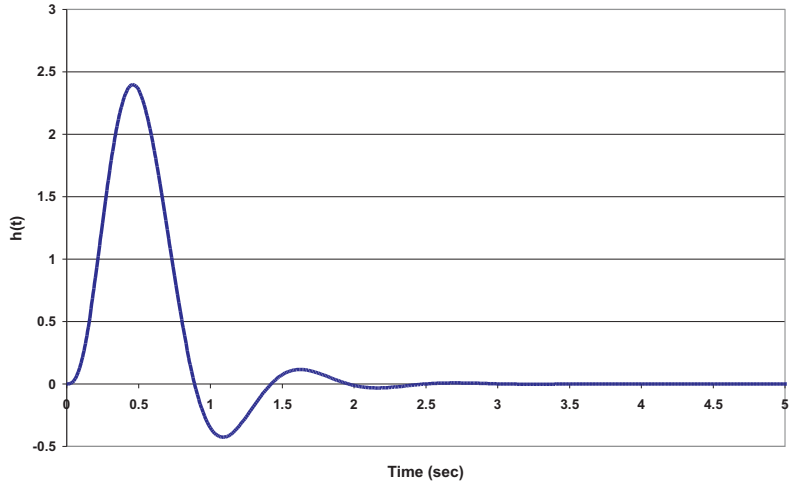

FIGURE B.5: Impulse-response Function of the 4^{th} Order RC Low-pass Filter (cut-off frequency = 1Hz or 6.283 rad.s^{-1})

B.3 Effects of the Order of the Low-pass Butterworth Filter

Comparing the graphs in Figure B.2 to Figure B.5 for the 1^{st} order and 4^{th} order filters, it can be seen that

- The higher order filter has a sharper frequency cut-off and therefore is able to allow more wanted frequency components and less unwanted frequency components to pass the filter. This is shown by the transfer function curves.

- The higher order filter's time response takes longer to reach the peak and also takes longer to die out. This can cause more phase delay in the output signal and more interference between signals.

For the above reasons, Butterworth filters with orders higher than 6 should be used with caution.

Regardless of the orders of the filters, the principle of a filter acting on input signals is the same, which can be presented either in frequency domain or time domain, as shown in equations B.9 and B.12.

Appendix C

Publications

1. **P. Hua, J.P. Hole, J.S. Wilkinson, G. Proll, J. Tschmelak, G. Gauglitz, M.A. Jackson, R. Nudd, R. Abuknesha, J. Kaiser and P. Krmmer** "Integrated optical immunofluoresence multisensor for river pollution" EWOFS'04 Second European Workshop on Optical Fibre Sensors, Santander, Spain, 2004.

2. **J. Tschmelak, G. Proll, J. Riedt, J. Kaiser, P. Kraemmer, J. S. Wilkinson, P. Hua, J. P. Hole, R. Nudd, M. Jackson, R. Abuknesha, D. Barcelo, S. Rodriguez-Mozaz, M. J. Lopez de Alda, F. Sacher, J. Stien, J. Slobodnik, P. Wswald, H. Kozmenko, E. Korenkova, L. Tothova, Z. Krascsenits, and G. Gauglitz** "Automated Water Analyser Computer Supported System (AWACSS) Part I: Project objectives, basic technology, immunoassay development, software design and networking" Biosensors and Bioelectronics, Vol.20, pp.1499-1508, 2005.

3. **J. Tschmelak, G. Proll, J. Riedt, J. Kaiser, P. Kraemmer, J. S. Wilkinson, P. Hua, J. P. Hole, R. Nudd, M. Jackson, R. Abuknesha, D. Barcelo, S. Rodriguez-Mozaz, M. J. Lopez de Alda, F. Sacher, J. Stien, J. Slobodnik, P. Wswald, H. Kozmenko, E. Korenkova, L. Tothova, Z. Krascsenits, and G. Gauglitz** "Automated Water Analyser Computer Supported System (AWACSS) Part II: Intelligent, remote-controlled, cost-effective, on-line, water-monitoring measurement system" Biosensors and Bioelectronics, Vol.20, pp.1509-1519, 2005.

4. **P. Hua, J.P. Hole, J.S. Wilkinson, G. Proll, J. Tschmelak, G. Gauglitz, M.A. Jackson, R. Nudd, H.M.T. Griffith, R. Abuknesha, J. Kaiser and P. Krmmer** "Integrated optical immunofluoresence multisensor for river pollution" Optics Express, Vol.13(4), pp.1124-1130, 2005.

5. **J. Tschmelak, G. Proll, J. Riedt, J. Kaiser, P. Kraemmer, J. S. Wilkinson, P. Hua, J. P. Hole, R. Nudd, M. Jackson, R. Abuknesha, D. Barcelo, S. Rodriguez-Mozaz, M. J. Lopez de Alda, F. Sacher, J. Stien, J. Slobodnik, P. Wswald, H. Kozmenko, E. Korenkova, L. Tothova, Z. Krascsenits, and G. Gauglitz** "Biosensors for unattended cost-effective and continuous monitoring of environmental pollution: Automated water analyser computer supported system (AWACSS) and river analyser(RIANA)" International Journal of Environmental Analytical Chemistry, Vol.85 (12-13), pp.837-852, 2005.

Bibliography

[1] G. R. Quigley, R. D. Harris, and J. S. Wilkinson, "Sensitivity enhancement of integrated optical sensors by use of thin high-index films," *Applied Optics*, vol. 38, no. 28, pp. 6036–6039, 1999.

[2] 2000/60/EC:, "Directive *2000/60/EC* of the european parliament and of the council of 23 *October* 2000 establishing a framework for community action in the field of water policy," *Official J. Eur. Commun. L327*, pp. 1–72, 2000.

[3] 98/83/EC:, "*COUNCIL DIRECTIVE (98/83/EC)* of 3 *November* 1998 relating to the quality of water intended for human consumption," *Official J. Eur. Commun. L330*, pp. 32–54, 1998.

[4] J. Tschmelak, G. Proll, J. Riedt, J. Kaiser, P. Kraemmer, J. Wilkinson, P. Hua, J. Hole, R. Nudd, M. Jackson, R. Abuknesha, D. Barcelo, S. Rodriguez-Mozaz, M. J. Lopez de Alda, F. Sacher, J. Stien, J. Slobodnik, P. Wswald, H. Kozmenko, E. Korenkova, L. Tothova, Z. Krascsenits, and G. Gauglitz, "Automated water analyser computer supported system (`AWACSS`) part `I`: Project objectives basic technology immunoassay development software design and networking," *Biosensors Bioelectronics*, vol. 20, pp. 1499–1508, 2005.

[5] J. Homola, S. Yee, and G. Gauglitz, "Surface plasmon resonance sensors: review," *Sensors and Actuators B Chemical*, vol. 54, pp. 3–15, 1999.

[6] R. Harris and J. Wilkinson, "Waveguide surface plasmon resonance sensors," *Sensors and Actuators B Chemical*, vol. 29, pp. 261–267, 1995.

[7] T. Akimoto, K. Ikebukuro, and I. Karube, "A surface plasmon resonance probe with a novel integrated reference sensor surface," *Biosensors & Bioelectronics*, vol. 18, pp. 1447–1453, 2003.

[8] T. Chinowsky, J. Quinn, and D. Bartholomew, "Performance of the *S*preeta 2000 integrated surface plasmon resonance affinity sensor," *Sensors and Actuators B Chemical*, vol. 91, pp. 266–274, 2003.

[9] G. B. Hocker and W. K. Burns, "Mode dispersion in diffused channel waveguides by the effective index method," *Applied Optics*, vol. 16, no. 1, pp. 113–118, 1977.

[10] W. Lukosz, "Principles and sensitivities of integrated optical and surface plasmon sensors for direct affinity sensing and immunosensing," *Biosens. Bioelectron.*, vol. 6, pp. 215–225, 1991.

[11] R. G. Heideman and P. Lambeck, "Remote opto-chemical sensing with extreme sensitivity: design, fabrication and performance of a pig-tailed integrated optical phase-modulated mach-zehnder interferometer system," *Sens. Actuators Part B. Chem.*, vol. 61, pp. 100–127, 1999.

[12] A. Collings and R. Caruso, "Biosensors: recent advances," *Reports on Progress in Physics*, vol. 60, pp. 1397–1445, 1997.

[13] P. Hua, B. J. Luff, G. R. Quigley, J. Wilkinson, and K. Kawaguchi, "Integrated optical dual *M*ach-*Z*ehnder interferometer sensor," *Sensors and Actuators B*, vol. 87, pp. 250–257, 2002.

[14] B. Luff, J. Wilkinson, J. Piehler, U. Hollenbach, J. Ingenhoff, and N. Fabricius, "Integrated optical *M*ach-*Z*ehnder bio-sensor," *IEEE J. Lightwave Technol.*, vol. 16, pp. 583–592, 1998.

[15] F. Prieto, B. Sepulveda, A. Calle, and C. Llobera, A.and Dominguez, "An integrated optical interferometric nanodevice based on silicon technology for biosensor applications," *Institute of Physics Publishing, Nanotechnology*, vol. 14, pp. 907–912, 2003.

[16] D. Nivens, T. McKnight, S. Moser, S. Osbourn, M. Simpson, and G. Sayler, "Bioluminescent bioreporter integrated circuits: potentially small, rugged

and inexpensive whole-cell biosensors for remote environmental monitoring," *Journal of Applied Microbiology*, vol. 96, pp. 33–46, 2004.

[17] E. Thrush, O. Levi, W. Ha, G. Carey, L. Cook, J. Deich, S. J. Smith, W. Moerner, and J. S. Harris, "Integrated semiconductor vertical-cavity surface-emitting lasers and *OIN* photodetectors for biomedical fluoresence sensing," *IEEE J. Quantum Elect.*, vol. 40, no. 5, pp. 491–498, 2004.

[18] O. H. Elibol, D. Morisette, D. Akin, J. Denton, and R. Bashir, "Integrated nanoscale silicon sensors using top-down fabrication," *Applied Physics Letters*, vol. 83, no. 22, pp. 4613–4615, 2003.

[19] A. Hierlemann, O. Brand, C. Hagleitner, and H. Baltes, "Microfabrication techniques for chemical/biosensors," *Proceeding s of the IEEE*, vol. 91, no. 6, pp. 839–863, 2003.

[20] K. Sapsford, Y. Shubin, J. Delehanty, J. Golden, C. Taitt, L. Shriver-Lake, and F. Ligler, "Fluorescence-based array biosensors for detection of biohazards," *Journal of Applied Microbiology*, vol. 96, pp. 47–58, 2004.

[21] R. M. Wadkinst, P. Golden, L. M. Pritsiolas, and F. Ligler, "Detection of multiple toxic agents using a planar array immunosensor," *Biosensors & Bioelectronics*, vol. 13, no. 3-4, pp. 407–415, 1998.

[22] F. Ligler, C. Taitt, L. Shriver-Lake, K. Sapsford, Y. Shubin, and J. Golden, "Array biosensor for detection of toxins," *Analytical and Bioanalytical Chemistry*, vol. 377, no. 3, pp. 469–477, 2003.

[23] H. P. Lehr, A. Brandenburg, and G. Sulz, "Modeling and expermental verification of the performance of *TIRF*-sensing systems for oligonucleotide microarrys based on bulk and integrated optical planar waveguides," *Sensors and Actuators B Chemical*, vol. 92, pp. 303–314, 2003.

[24] C. Taitt, G. P. Anderson, B. Lingerfelt, M. J. Feldsrein, and F. Ligler, "Nine-analyte detection using an array -based biosensor," *Anal. Chem.*, vol. 74, pp. 6114–6120, 2002.

[25] G. L. Duveneck, A. P. Abel, M. A. Bopp, G. M. Kresbach, and M. Ehrat, "Planar waveguides for ultra-high sensitivity of the analysis of nucleic acids," *Analytica Chimica Acta*, vol. 469, pp. 49–61, 2002.

[26] L. C. Clark and C. Lyons, "Electrode systems for continuous monitoring in cardiovascular surgery," *Ann. NY Acad. Sci*, vol. 120, pp. 29–45, 1962.

[27] Y. Tai, J. McGuire, O. Joshi, and W. D. Q., "Solid surface chemical and physical effects on the adsorption of recombinant factor *VIII*," *Pharmaceutical Development and Technology*, vol. 14, pp. 126–130, 2009.

[28] J. Armstrong, H. Meiselman, and T. C. Fisher, "Covalent binding of poly (ethylene glycol) (*PEG*) to the surface of red blood cells inhibits aggregation and reduces low shear blood viscosity," *American Journal of Hematology*, vol. 56, pp. 26–28, 1997.

[29] C. Jeanquartier, G. Schider, S. Feichtenhofer, and H. Schwab, "A two-step method to covalently bind biomolecules to group-*IV* semiconductors: *Si*(111)/1, 2-epoxy-9-decene/esterase," *Langmuir*, vol. 24, pp. 13 957–13 961, 2008.

[30] G. Luca, G. Basta, R. Calafiore, and C. Rossi, "Multifunctional microcapsules for pancreatic islet cell entrapment: design, preparation and in vitro characterization," *Biomaterials*, vol. 24, pp. 3101–3114, 2003.

[31] W. Henkel and R. Glanville, "Covalent crosslinking between molecules of type *I* and type *III* collagen," *Eur.J.Biochem.*, vol. 22, pp. 205–213, 1982.

[32] Z. Sui, N. Hanan, S. Phimphivong, R. J. Wysocki Jr, and S. Saavedra, "Synthesis, characterisation and sol-gel entrapment of a crown ether-styryl fluoroionophore," *Biological and chemical luminescence:www.interscience.wiley.com*, vol. DOI 10.1002/bio.1106, 2009.

[33] J. Tschmelak, G. Proll, J. Riedt, J. Kaiser, P. Kraemmer, J. Wilkinson, P. Hua, J. Hole, R. Nudd, M. Jackson, R. Abuknesha, D. Barcelo, S. Rodriguez-Mozaz, M. J. Lopez de Alda, F. Sacher, J. Stien, J. Slobodnik, P. Wswald, H. Kozmenko, E. Korenkova, L. Tothova, Z. Krascsenits, and G. Gauglitz, "Automated water analyser computer supported system

(AWACSS) part II: Project objectives basic technology immunoassay development software design and networking," *Biosensors Bioelectronics*, vol. 20, pp. 1509–1519, 2005.

[34] M. Farre, L. Kantiani, S. Perez, and D. Barcelo, "Sensors and biosensors in support of *EU* directives," *Trends in Analytical Chemistry*, vol. 28, no. 2, pp. 170–185, 2009.

[35] J. West, M. Becker, S. Tombrink, and A. Manz, "Micro total analysis systems: Latest achievements," *Anal. Chem.*, vol. 80, pp. 4403–4419, 2008.

[36] M. Seidel and R. Niessner, "Automated analytical microarrays: a critical review," *Anal. Bioanal. Chem.*, vol. 391, pp. 1521–1544, 2008.

[37] C. Rowe, L. Tender, M. J. Feldstein, J. P. Golden, S. B. Scruggs, B. D. MacCraith, J. J. Cras, and F. S. Ligler, "Array biosensor for simultaneous identification of bacterial, viral, and protein analytes," *Anal. Chem.*, vol. 71, pp. 3846–3852, 1999.

[38] J. Kim, D. Byun, M. Mauk, and H. Bau, "A disposable, self-contained *PCR* chip," *The Royal Society of Chemistry*, vol. 9, pp. 606–612, 2009.

[39] R. Pieler, E. Fureder, and M. Sonnleitner, "Printed photonics for lab-on-chip applications," *Electro-optical remote sensing, detection, and photonic technologies and thier applications,Proc.of SPIE*, vol. 6739, pp. 67 391–67 398, 2007.

[40] C. Taitt, L. Shriver-Lake, M. M. Ngundi, and F. S. Ligler, "Array biosensor for toxin detection: continued advances," *Sensors*, vol. 8, pp. 8361–8377, 2008.

[41] S. Rodriguez-Mozaz, M. Lopez de Alda, and D. Barcelo, "Biosensors as useful tools for environmental analysis and monitoring," *Anal. Bioanal. Chem.*, vol. 386, pp. 1025–1041, 2006.

[42] J. Lee, R. J. Mitchell, B. C. Kim, D. C. Cullen, and M. B. Gu, "A cell array biosensor for environmental toxicity analysis," *Biosensors and Bioelectronics*, vol. 21, pp. 500–507, 2005.

[43] G. Smith, "The invention of the *CCD*," *Nuclear Instruments and Methods in Physics Research A*, vol. 471, pp. 1–5, 2001.

[44] G. Duveneck, A. P. Abel, M. A. Bopp, G. M. Kresbach, and M. Ehrat, "Planar waveguides for ultra-high sensitivity of the analysis of nucleic acids," *Analytica Chimica Acta*, vol. 469, pp. 46–61, 2002.

[45] R. M. Wadkins, J. P. Golden, L. M. Pritsiolas, and F. S. Ligler, "Detection of multiple toxic agents using a planar array immunosensor," *Biosensors Bioelectronics*, vol. 13, no. 3-4, pp. 405–415, 1998.

[46] K. Jolling, M. Vandeven, J. Eynden, M. Ameloot, and E. Kerkhovn, "A highly reliable and budget-friendly *P*eltier-cooled camera for biological fluorescence imaging microscopy," *Microscopy*, vol. 228, no. 3, pp. 264–271, 2007.

[47] M. Seidel and R. Niessner, "Automated analytical microarrays: a critical review," *Anal Bioanal Chem*, vol. 391, pp. 1521–1544, 2008.

[48] X. Yu, X. Ding, F. Liu, and Y. Deng, "A novel surface plasmon resonance imaging interferometry for protein array detection," *Sensors and Actuators B*, vol. 130, no. 1, pp. 52–58, 2008.

[49] J. P. Golden and F. S. Ligler, "A comparison of imaging methods for use in an array biosensor," *Biosensors Bioelectronics*, vol. 17, pp. 719–725, 2002.

[50] W. Ho, J. Chen, M. Ker, and T. K. Wu, "Fabrication of a miniature *CMOS*-based optical biosensor," *Biosensors Bioelectronics*, vol. 22, pp. 3008–3013, 2007.

[51] G. R. Quigley, "Intergrated optical multisensors for water quality," *PhD thesis*, 2000.

[52] R. Harris, G. Quigley, J. Wilkinson, A. Klotz, C. Barzenzen, A. Brecht, G. Gauglitz, and R. A. Abuknesha, "Waveguide immunofluorescence sensor for water pollution analysis." *Chemical Microsensors and Applications*, vol. 3539, pp. 27–35, 1998.

[53] A. Miltoon, *IEEE J. Quantum Elect.*, vol. QE-13, p. 828, 1997.

[54] A. Miliou, H. Zhenguang, H. Cheng, R. Srivastava, and R. Ramaswamy, "Fiber-compatible K^+-Na^+ ion-exchanged channel wave-guides - fabrication and characterization," *IEEE J. Quantum Elect.*, vol. 25, pp. 1889–1897, 1989.

[55] P. J. Wallner, O. Winzer and W. R. Lee, "Alignment tolerances for plane wave to single-mode fibre coupling and their mitigation by use of pigtailed collimators," *Applied Optics*, vol. 41, pp. 637–634, 2001.

[56] B. J. Luff, J. Wilkinson, J. Piehler, U. Hollenbach, J. Ingenhoff, and N. Fabricius, "Integrated optical mach-zehnder bio-sensor," *J. Lightwave Technol.*, vol. 16, pp. 583–592, 1998.

[57] G. Stewart and B. Culshaw, "Optical waveguide modelling and design for evanescent field chemical sensors," *Optical and Quantum Electronics*, vol. 26, no. 3, pp. S249–S259, 1994.

[58] S. Fouchet, A. Carenco, C. Daguet, R. Guglielmi, and L. Riviere, "Wavelength dispersion of Ti induced refractive index change in $LiNbO_3$ as a function of diffusion parameters," *Journal of Lightwave Technology*, vol. LT-5, no. 5, pp. 700–708, 1987.

[59] G. P. Bava, I. Montrosset, W. Sohler, and H. Suche, "Numerical modeling of $LiNbO_3$ integrated optical parametric oscillators," *IEEE Journal of Quantum Electronics*, vol. QE-23, no. 1, pp. 42–51, 1987.

[60] J. E. Gortych and D. G. Hall, "Fabrication of planar optical waveguides by K^+ -ion exchange in BK7 and pyrex glass," *IEEE Journal of Quantum Electronics*, vol. QE-22, no. 6, pp. 892–895, 1986.

[61] M. N. Weiss and R. Srivastava, "Determination of ion-exchanged channel waveguide profile parameters by mode-index measurements," *Applied Optics*, vol. 34, no. 3, pp. 455–458, 1995.

[62] H. F. Taylor, "Dispersion characteristics of diffused channel waveguides," *IEEE Journal of Quantum Electronics*, vol. QE-12, no. 12, pp. 748–751, 1976.

[63] J. Albert and G. L. Yip, "Refractive-index profiles of planar waveguides made by ion-exchange in glass," *Applied Optics*, vol. 24, no. 22, pp. 3692–3693, 1985.

[64] R. Walker, C. Wilkinson, and J. Wilkinson, "Integrated optical waveguiding structures made by silver ion-exchange in glass. 1: The propagation characteristics of stripe ion-exchanged waveguides; a theoretical and experimental investigation," *Applied Optics*, vol. 22, no. 12, pp. 1923–1928, 1983.

[65] X. Zhang and R. Mears, "Planar optical waveguides formed by erbium ion exchange in glass," *Appl. Phys. Lett.*, vol. 62, no. 8, pp. 793–795, 1993.

[66] R. Ulrich and R. Torge, "Measurements of thin film parameters with a prism coupler," *Appl. Opt.*, vol. 12, no. 2, pp. 2901–2908, 1973.

[67] A. Brecht, C. Klotz, A.and Barzen, G. Gauglitz, R. Harris, G. Quigley, J. Wilkinson, P. Sztajnbok, R. Abuknesha, J. Gascon, A. Oubina, and D. Barcelo, "Optical immunoprobe development for multiresidue monitoring in water," *Analytica Chimica Acta*, vol. 362, pp. 69–79, 1998.

[68] H. Arwin, "Optical properties of thin layers of bovine serum albumin, γ-globulin, and hemoglobin," *Applied Spectroscopy*, vol. 40, no. 3, pp. 313–318, 1986.

[69] *http*: *//en.wikipedia.org/wiki/Beer-Lambertlaw.*

[70] J. S. Wilkinson, R. A. Abuknesha, G. Gauglitz, M. Steinwand, J.-L. Guinamant, and D. Barcelo, "River analyser final presentation," 1999.

[71] W. Heckele, W. Bacher, and Müller, "Hot embossing - the molding technique for plastic microstructures," *Mircosystem Technologies*, vol. 4, pp. 122–124, 1998.

[72] C. L. Chen and F. Jen, "Fabrication of polymer splitter by micro hot embossing technique," *Tamkang Journal of Science and Engineering*, vol. 7, no. 1, pp. 5–9, 2004.

[73] S. Sjölander and C. Urbaniczky, "Integrated fluid handling system for biomolecular interaction," *Anal. Chem*, vol. 63, pp. 2338–2345, 1991.

[74] "http://www.ndcinfrared.com/ndc/ndc%20optics.aspx."

[75] V. Thomsen, D. Schatzlein, and D. Mercuro, "Limits of detection in spectroscopy," *Spectroscopy*, vol. 18, no. 12, pp. 112–114, 2003.

[76] R. W. Glaser, "Antigen-antibody binding and mass transport by convection and diffusion to a surface: a two-dimensional computer model of binding and dissociation kinetics." *Analytial Biochemistry*, vol. 213, no. 1, pp. 152–161, 1993.

[77] J. Piehler, A. Brecht, K. Geckeler, and G. Gauglitz, "Surface modification for direct immunoprobes," *Biosensors & Bioelectronics*, vol. 11, pp. 579–90, 1996.

[78] J. M. Tschmelak, "New ultra-sensitive immunoassays for total internal reflectance fluorescence *TIRF*-based biosensors," *PhD Thesis*, 2005.

[79] R. Dudley, P. Edwards, R. Ekins, D. Finney, I. McKenzie, G. Raab, D. Rodbard, and R. Rodgers, "Guidelines for imunnoassay data processing." *Clin. Chem.*, vol. 31, no. 8, pp. 1264–1271, 1985.

[80] A. Brecht, A. Klotz, C. Barzen, G. Gauglitz, R. Harris, G. Quigley, J. Wilkinson, P. Sztajnbok, R. A. Abuknesha, J. Gascon, A. Oubina, and D. Barcelo, "Optical immunoprobe development for multiresidue monitoring in water," *Analytica Chimica Acta*, vol. 362, pp. 69–79, 1998.

[81] "*AWACSS* project meeting minutes, 01/03/2002."

[82] J. Slobodnik, M. G. M. Groenewegen, E. R. Brouwer, H. Lingeman, and U. A. T. Brinkman, "Fully automated multi-residue method for trace-level monitoring of polar pesticides by liquid chromatography." *J. Chromatogr.*, vol. 642, no. 12, pp. 359–370, 1993.

[83] J. Slobodnik and U. A. T. Brinkman, "*LC/MS* interfacing systems in environmental analysis: applications to polar pesticides. in: Barcelo, d. (ed), environmental analysis: Sample handling and trace analysis of pollutants-techniques, applications and quality assurance." *Elsevier*, pp. 935–1001, 2000.

[84] E. Korenkova, E. Matisova, and J. Slobodnik, "Large volume injection in capillary gas chromatography." *Chemicke Listy*, vol. 95, no. 9, pp. 528–539, 2001.

[85] J. Tschmelak, M. Kumpf, G. Proll, and G. Gauglitz, "Biosensor for seven sulphonamides in drinking , ground, and surface water with difficult matrices." *Anal. lett.*, vol. 37, no. 8, pp. 1701–1718, 2004.

[86] J. Tschmelak, G. Proll, and G. Gauglitz, "Immunosensor for estrone with an equal limit of detection as common analytical methods." *Analytical and Bioanalytical Chemistry*, vol. 378, no. 3, pp. 744–755, 2004.

[87] M. Manevich, M. Klebanov, V. Lyubin, J. Varshal, J. Broder, and N. P. Eisenberg, "Adaptive micro-lens arrays containing chalcogenide micro-lenses and nematic liquid crystals," *Chalcogenide Letters*, vol. 5, no. 4, pp. 58–60, 2008.

[88] J. L. Wiza, "Microchannel plate detectors," *Nuclear Instruments and Methods*, vol. 162, pp. 587–601, 1979.

[89] "*ORCA-R*^{2} technical note, http://www.orca-r2.com/assets/pdfs."

[90] W. S. Boyle and G. smith, "Charge coupled semiconductor devices," *Bell System Technical Journal*, vol. 49, p. 587, 1970.

[91] H.-P. Lehr, A. Brandenburg, and G. Sulz, "Modeling and experimental verification of the performance of tirf-sensing systems for oligonucleotide microarrays based on bulk and integrated optical planar wavegrudes," *Sensors and Actuators B*, vol. 92, pp. 303–314, 2003.

[92] T. J. Fellers and M. Davidson, "*CCD* noise sources and signal-to-noise ratio," *http://imagingu.com/articles/ccdsnr.html*.